Developing an Electron Multipacting-Free Cathode Unit of the Superconducting Radio Frequency Photoinjector

Dissertation
zur
Erlangung des akademischen Grades
Doktor-Ingenieur (Dr.-Ing.)
der Fakultät für Informatik und Elektrotechnik
der Universität Rostock

vorgelegt von

Eden Tafa Tulu
geb. am 02.11.1983 in Guder
aus Äthiopien

Rostock, 2020

https://doi.org/10.18453/rosdok_id00002903

Tag der Einreichung: 26.05.2020
Tag der Verteidigung: 02.10.2020

Gutachter
Prof. Dr. rer. nat. habil. Ursula van Rienen, Universität Rostock
Prof. Dr.-Ing. Herbert De Gersem, Technische Universität Darmstadt
Prof. Dr. Thorsten Kamps, Helmholtz-Zentrum Berlin

To my precious Miheret and Tsega

Acknowledgments

My utmost gratitude goes above all to Almighty God, who is the source of life, inspiration and strength.

This work was supported by the German Federal Ministry for Research and Education BMBF under contracts 05K13HRB.

This PhD project would not have been possible without the support of many people. First of all, I would like to devote very special thanks to Prof. Dr. rer. nat. habil. Ursula van Rienen for giving me the opportunity to work on this topic in her research group. Her kind support, patience, good advice, innumerable discussions throughout this research and insightful comments on this thesis are particularly appreciated. It was a great privilege and honor to work under her guidance.

I am also grateful to Prof. Xin Jiang, Prof. Jens Knoblauch, Dr. André Arnold, Dr. Michael Vogel, Dr. Erion Gjonaj, and the other members of the HOPE consortium, for valuable discussions and comments during this work. I convey special thanks to André Arnold for his input regarding the SRF photoinjector and for productive discussions around my topic.

I would like to express my appreciation to all my colleagues (EX) and friends at the institute, particularly Bachir Delanda, Shahnam Gorgi Zadeh, Dr.-Ing Revathi Appali, Dr.-Ing Kiran K. sriperumbudur, Dr.-Ing Thomas Flisgen, Dr.-Ing Tomasz Galek, Dr.-Ing Christian Schmidt, Dr.-Ing Johan Heller, Gowrishankar Hallilingaiah, Prasanth B. Ganta, Junaid Sadrach, Degol W/Gaber, Dr.-Ing Mirjana Holst, Dr. Piotr Putek, Dr. Christian Bahls, Dr.-Ing Dawei Zheng, Dr. Bernhard Himmel, Dr. Dirk Hecht, Kathrin Krebs and Petra Gefken for their valuable assistance and support of all kinds during my research.

I convey special acknowledgement to all my best friends. Their love, assistance and advice have made their own meaningful contributions towards the completion of this research work. I could not go without mentioning our scientific and social discussions and exhilarating times we spent together. I want to express my deep appreciation and love for all my friends. Thank you!

It is pleasure to express my wholehearted gratitude to my family for their love, unceasing support, prayers and encouragement. My mother Birhane deserves special mention for her unconditional love and care since my childhood. Her encouragement and prayer when times got rough are much appreciated. I am also very grateful to my father Tafa for the inspiration he has been to make me all that I am. I wish he were here with us. I know he would be proud of my every success. Lastly, thanks to my beautiful daughters Miheret and Tsega for their support and patience while I

was writing this thesis and throughout this project.

Abstract

Future light sources such as synchrotron radiation sources driven by an Energy Recovery Linac, Free Electron Lasers or THz radiation sources have in common that they require injectors, which provide high-brilliance, high-current electron beams in almost continuous operation. Thus, the development of appropriate highly brilliant electron sources is of key importance. With its superconducting radio frequency photoinjector (SRF gun) the Helmholtz-Zentrum Dresden-Rossendorf provided a promising approach for this key component, which has since been adopted in other laboratories. However, some limitations occur caused by electron multipacting in the cathode vicinity, which prevent the SRF gun from maximum productivity. The aim of this thesis is to deepen the understanding of multipacting and to obtain potential multipacting suppression techniques through detailed numerical investigations, and simple analytical analysis in the critical area of the SRF gun. Most importantly, the investigation is focused on developing a new (or an improved) design of the photocathode channel, which is an essential component for developing an MP-free SRF gun. Therefore, several possible remedies to suppress electron multipactor discharge and to improve the breakdown threshold in the vicinity of the photocathode of the SRF gun are investigated. Introducing cylindrically symmetric rectangular grooves and cylindrically symmetric isosceles grooves on the cathode surface of the SRF gun proved to be an efficient way to totally avoid vacuum electron multipacting. Moreover, a systematic multi-objective optimization based on a *trust-region algorithm* is performed to obtain optimal geometric parameters for these newly designed cathode stems. In a final step, the robustness of the optimized models is examined through uncertainty quantification and global sensitivity analysis. For this purpose, this work employs advanced tools, i.e. the generalized polynomial chaos expansion, and the generalized polynomial chaos based Sobol sensitivity indices. In conclusion, the development of this MP-free cathode unit serves particularly the further development at ELBE and thus the increase of the performance of existing and future compact accelerators. Nonetheless, the concrete and methodological results obtained here are of high value for similar national projects as well; for instance, for the development of an SRF photoinjector for bERlinePro at Helmholtz Zentrum Berlin. There is also significant international interest in using an SRF gun with comparable cathode unit with efforts to simplify the design as well as the negative influence of adsorbates as a result of cathode coating and the operation at cryogenic temperatures.

Zusammenfassung

Zukünftige Lichtquellen wie Synchrotronstrahlungsquellen, die von einem Energy-Recovery-Linac (ERL), freien Elektronenlasern oder THz-Strahlungsquellen angetrieben werden, haben gemeinsam, dass sie Injektoren benötigen, die hochbrillante Hochstromelektronenstrahlen in nahezu kontinuierlichem Betrieb bereitstellen. Daher ist die Entwicklung geeigneter hochbrillanter Elektronenquellen von zentraler Bedeutung. Das Helmholtz-Zentrum Dresden-Rossendorf hat mit seinem supraleitenden Hochfrequenz-Photoinjektor (SRF-Gun) einen vielversprechenden Ansatz für diese Schlüsselkomponente geschaffen, die inzwischen auch in anderen Laboren Anwendung gefunden hat. Nichtsdestotrotz treten einige Einschränkungen auf, die durch Elektronenvervielfachung verursacht werden, und unterdrückt werden sollten, um die SRF-Gun weiter zu verbessern.

In diesem Projekt wurde eine detaillierte Analyse des Multipacting im kritischen Bereich der SRF-Gun durchgeführt und verschiedene Unterdrückungstechniken für das Multipacting untersucht. Die analytischen Vorhersagen über den Schwellwert für das Multipacting sind qualitativ vergleichbar mit numerischen Simulationsergebnissen und experimentellen Daten. Mehrere mögliche Maßnahmen zur Unterdrückung der Elektronen-Multipaktor-Entladung und zur Verbesserung des Schwellwertes in der Nähe der Photokathode des SRF-Guns wurden untersucht. Die Einführung von rechteckigen und dreieckigen Rillen auf der Kathodenoberfläche erwies sich als eine effiziente Möglichkeit zur Unterdrückung von Vakuum-Elektronen-Multipacting.

Die Parameter für die rechteckig und dreieckig gerillten Oberflächen wurden in Bezug auf die Anzahl der Teilchen sowie auf die mittlere Sekundäremissionsausbeute optimiert (δ_a). Zu Beginn haben wir die Geometrieparameter der Rillen manuell in Bezug auf die Anzahl der Partikel im Laufe der Zeit variiert. Basierend auf diesen Ergebnissen konnten wir Geometrieparameter mit starken Auswirkungen auf das MP identifizieren. Diese Parameter wurden dann mit dem sogenannten trust-region-Algorithmus weiter optimiert. Dieser Algorithmus bietet die global beste Lösung für unsere Modelle. Im Gegensatz zur manuellen Optimierung wurde dies im Hinblick auf die besser geeignete, d.h. niedrigere Sekundäremissionsausbeute (δ_a) durchgeführt. Die Anfangsparameter wurden basierend auf den manuellen Ergebnissen ausgewählt. Die Optimierungszielfunktion erfordert, dass der SEYa kleiner als der Multipacting-Schwellenwert ist ($\delta_a < 1$).

Die numerischen Untersuchungen zur stochastischen Abhängigkeit der sekundären Emissionskoeffizienten in einem neu konstruierten Photokathodenkanal der SRF-Gun wurden dann untersucht. Der SEY-Wert wird durch Oberflächenkontamination bee-

influsst, daher steigt dieser Wert oft während des Betriebs der SRF-Gun an. Daher war es erstrebenswert, auch eine globale Sensitivitätsanalyse durchzuführen, um so zu bestimmen, wie sich im gewählten Modell die Variabilität des Sekundärelektron-Emissionskoeffizienten auf den SEYa auswirkt sowie den Arbeitsbereich der gerillten Strukturen in Abhängigkeit vom multipacting-Schwellwert ($\delta_a < 1$) zu bestimmen. Aus diesem Grund wurden die verallgemeinerte, polynomiale Chaos-basierte Quantifizierung von Unsicherheiten und das Sobol-Indexverfahren verwendet, um die Sensitivität in den Modellergebnissen zu bestimmen.

Contents

List of Figures

List of Tables

List of Abbreviation

(CSIG)	cylindrically symmetric isosceles grooved
ANOVA	ANalysis of VAriance
BC	boundary condition
BNL	Brookhaven National Laboratory
C_2Te	cesium telluride
CSRG	cylindrically symmetric rectangularly grooved
CSSG	cylindrically symmetric sawtooth grooved
CST PS	CST PARTICLE STUDIO®
Cu	Copper
cw	continuous wave
e.g.	example
EM	electromagnetic
Eq.	Equation
ERL	Energy Recovery Linac
FD	Frequency Domain
FDTD	finite difference time domain
FELs	Free Electron Lasers
FEM	finite element methods
Fig.	Figure
FIT	finite integration technique
gPC	generalized polynomial chaos

GSA	global sensitivity analysis
HEX	Hexahedral
HZB	Helmholtz-Zentrum Berlin
HZDR	Helmholtz-Zentrum Dresden-Rossendorf
LEP	Large Electron-Positron Collider
LHC	Large Hadron Collider
Linac	linear accelerator
LMR	*local mesh refinement*
LN_2	liquid nitrogen
Mg	magnesium
MGEs	*Maxwell's Grid Equations*
MP	multipacting
NCRF	normal conducting RF
PBA	Perfect Boundary Approximation®
PC	polynomial chaos
PCE	Polynomial Chaos expansion
PDF	probability density function
PEC	perfect electric conductor
PIC	Particle-in-Cell
PMC	perfect magnetic conductor
QE	quantum efficiency
RF	radio frequency
SEY	secondary electron emission
SRF	superconducting RF
SSI	Sobol sensitivity indices

TE	transverse electric
TEM	transverse electric and magnetic
TET	Tetrahedral
TM	transverse magnetic
UV	ultraviolet

1 Introduction

A particle accelerator is a device that accelerates charged particles, such as protons, electrons and ions, to very high energies using electromagnetic fields [154], [96]. Nowadays a major portion of particle accelerators work with radio frequency (RF) cavities as they allow to achieve very high energies. The electromagnetic (EM) fields are excited in the cavity using external power sources. The particles experience an acceleration, as they interact with the electric field. Their velocity can increase until they approach the speed of light. In accordance with Einstein's law $E = mc^2$ with the energy E, the mass m and the speed of light c, relativistic particles do no longer gain in velocity but in energy. The accelerating field has to be synchronized with the motion of particles to maintain the unidirectional acceleration. Moreover, for efficient acceleration, the accelerating mode is chosen to have maximal electric field and vanishing magnetic field on the axis where the particles pass. Therefore, cavities operated with the TM_{010} mode[1] are commonly used for such purpose. The particles are steered and focused by magnetic fields. Hence, modern particle accelerators use an assortment of magnets, i.e. dipole, quadrupole, sextupole, decapole magnets. For instance, dipole magnets are used for bending the path of the particles, whereas the quadrupole magnets are employed for focusing the beam of particles. Usually, particles are accelerated in ultra-high vacuum chambers to avoid collisions with residual gas that could potentially obstruct the path of the particles.

In particle accelerators, the particles can take a linear, a spiral or a circular path. Based on this, accelerators are commonly classified as linear accelerators (linac) and ring-type accelerators, namely synchrotrons and cyclotrons [154], [159]. As the name indicates, linear accelerators, the particles move on a straight line from one end to another. Unlike linacs, particles move on a circular orbit in synchrotrons and follow a spiral path inside cyclotrons.

Particle accelerators have a broad spectrum of applications, including ion implantation, lithography for microcircuits, thin-film technology, production of radioisotopes for medical or industrial purpose, proton and ion beam therapy to treat tumours, and production of synchrotron light sources. The synchrotron light sources [15], which use the EM radiation as a light source, are employed in the study of various fields of science such as condensed matter physics, materials science, biology, and medicine. For instance, ELBE [43] and PETRA III [9] are current examples

---

[1] TM mode refers to a *transverse magnetic mode*. The mode is characterized by a longitudinal electric field in the center of the cavity and by a transverse magnetic field component there on the axis. The associated subscripts indicate the mode classification. Further clarification is briefly explained in chapter two.

for synchrotron light sources in Germany. X-Ray Free Electron Lasers (XFELs) are novel light sources which are considered as *fourth generation light source* [160]. They enabled the study of the dynamics of atomic and molecular processes in the ultra-fast (in a few femtoseconds) time scales [37]. Furthermore, large particle accelerators have been applied in high-energy physics research. Prominent examples are the Tevatron [30], the Large Electron-Positron Collider (LEP) [88] or the Large Hadron Collider (LHC) [99], [40]. These modern and powerful particle colliders collide charged particles into each other at very high energy, for instance up to 6.5 TeV in LHC. The information on new particles that arise from the collision is used to study the physics of elementary matter. For example, the discovery of gluon [10] and the Higgs boson [1],[27] was achieved at PETRA, DESY and at LHC, CERN,

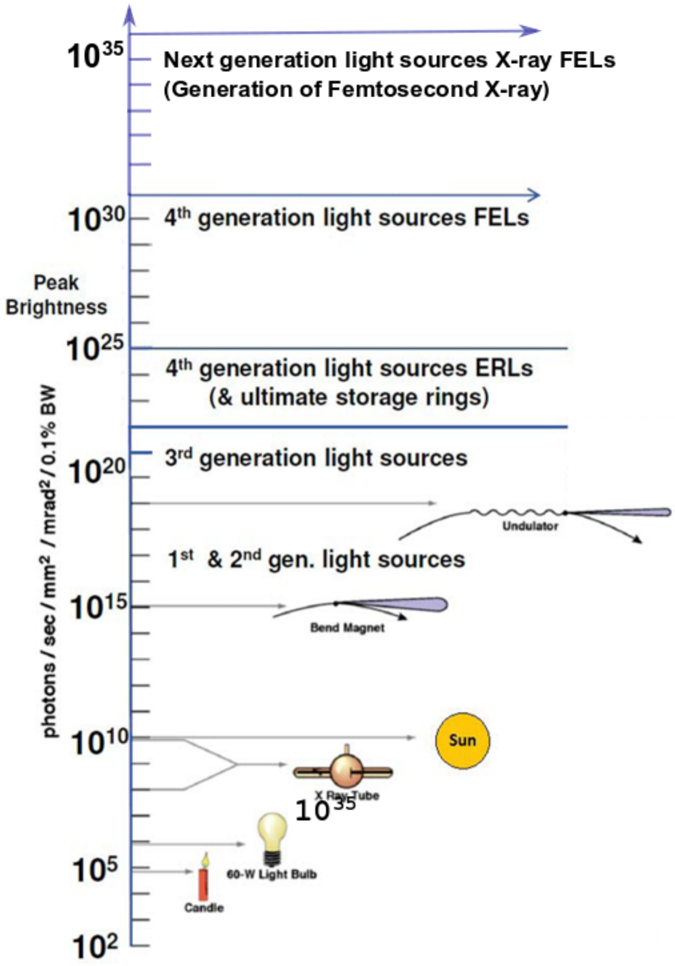

Figure 1.1: Evolution of peak brilliance of various light sources. Adapted from [117] p.167,[97].

respectively.

The applications mentioned above, including high energy particle colliders and the fourth generation light sources such as synchrotron radiation sources driven by an Energy Recovery Linac (ERL) [137], [52], Free Electron Lasers (FELs) [82],[117] or THz radiation sources require photoinjectors or RF guns. Photoinjectors provide high-brilliance, high-current electron beams in almost continuous operation. For this purpose, an advanced injector, such as a superconducting RF (SRF) injector, for high brightness beams, has been developed [24], [61].

The idea of an RF gun dates back to 1984 when Westenskow placed a thermionic cathode in an RF cavity [157]. Shortly after, the laser-driven RF gun using a semiconductor photocathode was demonstrated in 1990 [33]. In the meantime, the use of a superconducting cavity in the RF gun was introduced at the University of Wuppertal in 1988 [24], which merged the technology of a normal conducting RF (NCRF) injector and superconductivity. The first operational SRF gun, the ELBE SRF photoinjector or Drossel SRF injector, was demonstrated at the Forschungszentrum Rossendorf in 2002 [61]. Following this, the development of SRF photoinjectors has been progressing over the last few decades involving various technologies such as superconductivity, photocathodes, drive lasers.

Apparently, in modern particle accelerator applications, the SRF injector has received extensive attention. Such types of injectors have been developed worldwide, intended for various scientific and industrial applications. Among others, ELBE SRF photo gun, HZB bERLinPro gun, BNL/AEC SRF gun, hybrid Pb-Nb SRF gun, PKU gun and (NPS/Niowave/NNB) Mark I SRF gun can be mentioned. These guns are discussed in [6], [105]. Various approaches are considered in the design of these SRF injectors based on cavity shape, number of cavity cells, material, and position of the cathode, etc.

The centre of interest in choosing the SRF gun technology for a continuous wave (cw) operation or high *duty factor*[2] is the accelerating electric field level (accelerating gradient, E_{acc}) and the quality factor, Q-factor[3]. The SRF guns can operate at very high E_{acc} with lower power dissipation comparing to NCRF injectors. Even though the NCRF gun can produce a high-quality beam, it is limited to low duty factor operation due to an excessive amount of RF power dissipation into the structure's wall. To compensate for this power loss, a very large amount of RF power is required to maintain the operational accelerating fields. Moreover, the dissipation of the power is accumulated as heat on the structure's wall. It is costly and challenging to eliminate this heat as fast as required, which makes it difficult to operate an NCRF injector at a high duty factor [35], [105]. Thus the SRF injector is a perfect choice to address this issue. Furthermore, the SRF gun can provide a range of options

---

[2] duty factor (or duty cycle) can be defined as the product of pulse width and pulse-repetition frequency. It is usually expressed as a percentage.

[3] Q-factor of the RF cavity measures the stored energy with respect to the RF losses in the cavity.

(applications) by adjusting the beam's repetition rate, average current, and bunch charge.

However, there are a number of constraints, which prevent the SRF gun from maximum productivity. One of the main concerns is the insertion and operation of the non-superconducting photocathodes in the SRF cavity, which has a significant impact on cavity performance. This issue includes surface contamination due to the cathode materials and RF heating at the photocathode associated with RF fields at its surface, thermal conduction, and the exciting laser beam. These conditions are favourable to cause multipactor discharge, which results in poisoning the photocathode, degradation of Q-factor and E_{acc}. The performance of an SRF cavity is characterized by the latter two parameters, i.e. Q-factor and E_{acc}, [5], [105]. Therefore, this study aims to obtain potential suppression techniques for multipacting (MP) through detailed numerical investigations at the photocathode area. MP will be briefly discussed below, and a detailed theory is provided in Chapter 2.

1.1 Multipactor Discharge

One of the central efforts in the development of SRF injectors is achieving a higher E_{acc}. Toward this, as already mentioned, one of the significant challenges is the issue of MP which should be appropriately addressed. The electron MP may take place in many RF components operating in vacuum, for example, the SRF cavity, the coupler, the photocathode channel, and the RF windows. The source of an initial electron can be field emission, photoemission, ionization in the residual gas (imperfect vacuum), cosmic ray, and the photocathode laser [96]. This electron gets accelerated by RF fields and generates a secondary electron by impacting an RF structure surface, wherein electrons move back and forth in synchronism with the RF fields [63]. Then it leads to an avalanche effect and results in degradation of the vacuum, local heating within the distinct range of RF power levels, power reflection and fluctuation, surface damage, sparking, and even damage to RF components. The MP electron absorbs large amount of the RF power from the RF field and deposits it as heat on the surface. In the particular case of the SRF cavity, MP reduces the Q-factor and eventually might cause the cavity to quench. Therefore, in order to overcome the limitation caused by MP, possible suppression techniques have to be investigated and applied in each particular case. Some potential MP suppression methods have been introduced and studied in various projects. However, the data on the effectiveness of those approaches are still limited. Moreover, as multipactor discharge is a complex phenomenon, in most cases it should be individually treated.

Evolution of multipactor theories and several experimental developments are reviewed by Kishek [63] and Chang [26] in detail. MP is primarily well recognized and described in 1934 by Farnsworth [38]. Later in the 1930s and 1940s, multipactor was analyzed in a flat gap theoretically as well as experimentally. This study led to introducing the *adhoc* assumption by Gill and von Engel, which stated that a parameter k equal to the ratio of the impact velocity of the primaries to the emission velocity of secondaries is constant [48]. Hatch and Williams reformulated the latter assumption based on other theories and their own experimental and theoretical findings, which allowed to construct the susceptible zones for the fundamental and higher-order MP modes in 1950s [55], [56]. This theory is called the constant k theory. In the 1980s the constant k theory was advanced with a realistic assumption of a monoenergetic nonzero initial velocity (equivalent to a few eV) by Shemelin [123] and by Vaughan [148]. Additionally, phase stability was introduced by the latter theory.

The concept has been extended, and several theoretical and experimental studies have been done by many experts [138]. Most importantly, in recent decades, Furman and Pivi developed a mathematically self-consistent phenomenological probabilistic model for the secondary emission process. The model is a very good fit to experimental data of secondary emission yield (SEY)[4] [42]. The model considers the probability of the three kinds of emitted secondary electrons such as a true electron, backscattered, and rediffused electrons. This emission model was employed throughout our numerical study and will be further explained in chapter two.

1.2 Motivation

One approach to build an SRF gun is to combine the normal conducting cathode with an SRF cavity. This kind of injector has been developed and operated, for instance at Helmholtz-Zentrum Dresden-Rossendorf (HZDR) [5], at Helmholtz-Zentrum Berlin (HZB) [21], and at Brookhaven National Laboratory (BNL) [167]. The HZDR started to develop a 1.3 GHz 3.5 cell TESLA-type cavity SRF injector for the ELBE linac in 2004 based on successful experimental results gained from a 1.3 GHz half cell cavity SRF gun [61], [133]. The gun has been operated in three different modes. The corresponding operational modes are presented in Table 1.1. ELBE SRF injector produces an electron beam that is used for free-electron lasers (FELs), MeV-bremsstrahlung (synchrotron radiation), X-rays, fast neutrons and positrons. These allow for the use of various user experimental studies and applications [83]. Similarly, a 1.4 cell 1.3 GHz TESLA cavity-based SRF gun has been developed in the frame of the project bERLinPro at HZB [21]. The cavity is combined with a multi-alkali photocathode and a choke cell gun cavity. The injector provides a high average current beam up to 100 mA (77 pC at 1.3 GHz), for a 50 MeV ERL facility. A 704 MHz half-cell SRF gun is another example, which has been built at BNL for the research and development in an ERL project. The gun delivers 0.5 A, 2 MeV electron beam to a high average current, up to 500 mA, ERL [167].

---

[4] SEY denotes the number of emitted secondary electrons released per incident electron.

Table 1.1: Parameters of SRF Gun in different mode

Parameter	ELBE mode	High charge mode	BESSY-FEL mode
RF frequency	1.3 GHz	1.3 GHz	1.3 GHz
Nominal beam energy	9.5 MeV	9.5 MeV	9.5 MeV
Operation mode	CW	CW	CW
Driver laser wavelength	262 nm	262 nm	262 nm
Photocathode	Cs2Te	Cs2Te	Cs2Te
Quantum efficiency	≥1 %	≥1 %	≥2.5 %
Average current	1 mA	1 mA	2.5 μA
Laser pulse length	5 ps	20 ps	30 ps
Repetition rate	13 MHz	1 MHz	1 kHz
Bunch charge	77 pC	1 nC	2.5 nC
Transverse emittance	1 μm	2.5 μm	3 μm

The ELBE SRF injector, namely ELBE SRF Gun I, had been operated from 2007 until 2014. The detailed design of this gun has been presented in [5]. The SRF Gun I had been served as one of the electron injectors of the ELBE linac providing an electron beam with 3.3 MeV. Moreover, the installation of a new ultraviolet (UV) laser driver in 2012 enabled the gun application to be extended for an FEL operation [135]. To enhance the performance of this gun, i.e., beam quality and cavity gradient, and to attain its design values, which are limited by some constraints, for instance, field emission, an improved version of the gun, known as SRF Gun II, was installed in 2014 at ELBE. Most of the SRF Gun II design is similar to that of the previous gun (SRF Gun I). Some modifications are however included, e.g., the improvement on the half-cell cavity and the replacement of a normal conducting solenoid by a new design superconducting (SC) solenoid.

The ELBE SRF injector (SRF Gun II) shown in Fig. (1.2) comprises a 1.3 GHz 3.5 cell TESLA-type cavity, an SC solenoid, an SC choke filter cell, a photocathode, a main coupler as well as a 13 MHz UV laser system. The cavity is made of the SC material fine grain niobium (Nb). The cavity is surrounded by a helium (He) tank and cooled down to 2 K, which is installed in a stainless-steel cryostat. The cathode is placed at the back wall of the half-cell Nb cavity (gun cell) with a 1 mm circular vacuum gap, which provides thermal and electrical insulation between the cavity and the cathode. The cathode stem consists of a copper body and molybdenum plug, which is attached at the tip of the stem. The diameter and length of the cathode stem are 10 mm and 130 mm, respectively. The SC solenoid is installed near to the cavity for beam focusing. The electron bunches are produced as a UV laser beam impinges the photocathode. The main coupler supplies the RF power to the cavity. The electron bunches emitted from the cathode are accelerated using the RF fields in the RF cavity before being injected into the accelerator.

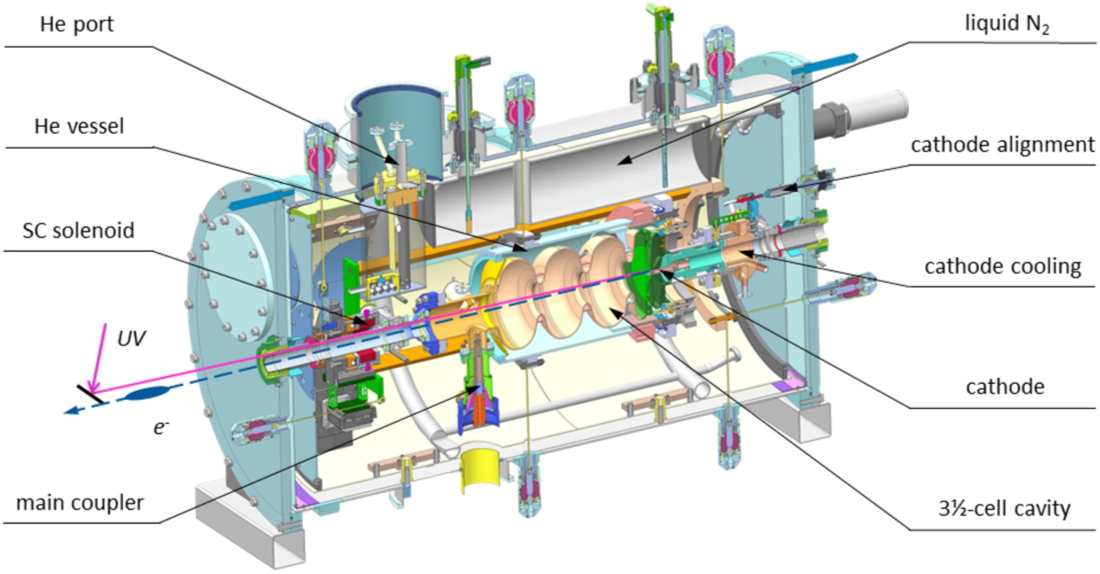

Figure 1.2: A cross section of the ELBE SRF gun II and its cryostat. Taken from [136] with permission.

The geometrical arrangement of the photocathode and the hole at the backplane of the half-cell form a coaxial line, which results in RF losses in the cavity. A choke filter cell is attached to the gun to reduce the RF losses due to the leakage of RF energy into the coaxial line from the gun cell. The cathode works at 77 K. It is cooled by an external liquid nitrogen (LN2) reservoir. An electrical insulator is installed between the cooler and the photocathode that enables to measure the emission current of the cathode and to apply a direct current (DC) voltage to suppress MP.

Normal- and semiconductor photocathode materials such as copper (Cu), magnesium (mg) and cesium telluride (C_2Te) are used in the SRF Gun II. The SRF Gun II is successfully tested with the Cu cathode and demonstrated an accelerating gradient of 9 MV/m, with a corresponding peak surface electric field of 23 MV/m. However, when the SRF Gun II was tested with a C_2Te cathode afterwards, the accelerating gradient was limited to 7 MV/m due to a severe contamination [136],[162]. Currently, the SRF Gun II is being operated with Mg cathodes at the gradient of 8 MV/m, which provides the beam properties required for the THz operation. It delivers a beam with a bunch charge of up to 200 pC [163]. The desired characteristics of a photocathode for a high brightness beam production include high quantum efficiency (QE) and a long lifetime. A higher QE of up to 10^{-2} can be obtained using Cs_2Te instead of metallic photo emitters, such as Cu and Mg. However, Cs_2Te is very sensitive to residual gas contamination [84],[104].

Besides the cathode material issue, the coaxial channel provides conditions susceptible to MP due to the RF field leaking into it. As mentioned above, the choke filter is installed to reduce the penetration of the RF leakage between the cathode and the back wall of the cavity. However, the field at the cathode is still sufficient to induce MP, as shown in Fig. 1.3. Due to this effect, it turns out that a strong input mismatch paired with a resonance drift makes it unfeasible to raise the accelerating gradient by increasing the incident RF power. Therefore, this phenomenon is a serious problem that limits the E_{acc} in the cavity to very low values by absorbing the available RF power [134]. Multipactor electron discharge in the cathode unit will be further explained in chapter two.

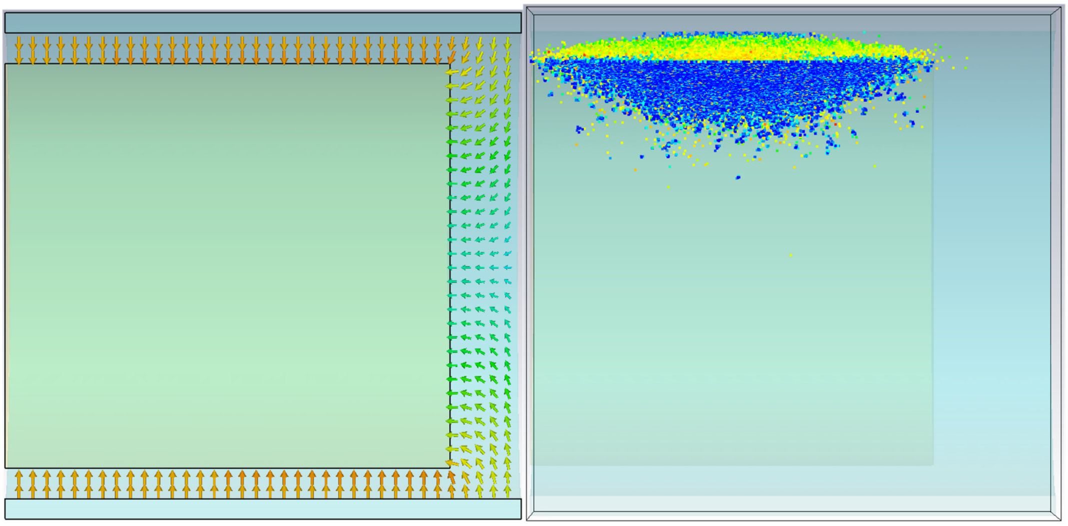

Figure 1.3: Electric field in the coaxial line of the SRF gun (left). Electron population under the presence of the electric field shown in the left (right).

1.3 Objectives and Outline of the Thesis

The objective of this research is to deepen the understanding of MP at the cathode unit of SRF guns based on simulation, and simple analytical analysis. Most importantly, our investigation is focused on developing a new (or an improved) design of the photocathode channel, which is an essential component for developing an MP-free SRF gun. This development should enable the injector to operate up to the desired peak electric field of 50 MV/m. The development of an MP-free cathode unit serves particularly the further development at ELBE and thus the increase of the performance of existing and future large devices and compact accelerators. Nonetheless, the concrete and methodological results obtained here are of high value for similar projects as well; for instance, for the development of an SRF photoinjector for bERlinePro [91]. There is also significant international interest in using an SRF gun with comparable cathode unit with efforts to simplify the design as well as the negative influence of adsorbates as a result of cathode coating and the operation at cryogenic temperatures.

This study includes three main subtasks to build a new design of the photocathode channel: an investigation of the occurrence of MP in the existing design of ELBE SRF photoinjector, employing various mitigation techniques of multipactor discharge, and a systematic multi-objective optimization for a newly designed cathode stem. Moreover, a stochastic method is applied to evaluate the new model of the cathode stem based on the variability of the most influential input parameters of the SEY model to resulting quantities of interest such as the average SEY.

The topics covered in this dissertation are structured as follows. In the following chapter, Chapter 2, the theoretical background required to understand the multipactor phenomenon is offered by taking a look at the electron dynamics in the presence of EM fields as well as the numerical approach to simulate multipaction. The theory includes electron dynamics in EM fields; Maxwell's equations; EM waves and Helmholtz equations; EM waves in a closed structure; numerical solutions of Maxwell's equations by discretization methods such as finite integration technique and finite element method; particle-in-cell method; multipactor discharge; secondary electron emission mechanism; secondary electron emission model of Furman.

Analytical and numerical studies of multipactor discharge in the photocathode channel are presented in Chapter 3. The definition of our model is provided. The numerical simulation results for multipactor breakdown are compared using 2D and 3D software tools. On the other hand, a comparison of theoretical and numerical studies on a coaxial line multipactor is also given.

Chapter 4 covers numerical studies for various possible techniques to mitigate MP. There are four mitigation approaches applied such as DC biasing voltage, geometric modification, microstructure (grooving) of the cathode surface. A detailed analysis of the latter technique, including rectangularly grooved surface, sawtooth triangularly grooved surface, and isosceles triangularly grooved surface are given. These methods are found to be effective to suppress MP. An optimized model of this grooved structure using a trust-region algorithm is discussed. Moreover, simulation results for the anti-MP coating are included. Experiments carried out by others provide the measurement data for some surface materials.

Chapter 5 offers a global sensitivity analysis using polynomial chaos technique. The theory of this technique in the frame of our study is given. Results computed from polynomial chaos-based Sobol' indices for the grooved surface of the cathode stem are presented.

The closing chapter, Chapter 6, contains a discussion and a summary of this study. It provides the occurrence of MP at the photocathode channel of the SRF gun and its several suppression methods. It is also underlined that effective techniques to suppress MP could be obtained from this study.

2 Basics of Multipactor Discharge

Numerical MP studies demand the solution of the equation of motion of electrons in the electromagnetic field, with the appropriate boundary conditions on the boundaries of the computational region. The computation of the motion of the charged particles is a very complex problem, as an external EM field, self-induced EM field, the motion of particles, particle interactions with other particles, and their interaction with solid objects can be involved. In this chapter we will discuss the basics of the electron dynamics in the RF fields in the context of MP, which also considers the interaction between particles and a solid object.

2.1 Electron Dynamics in Electromagnetic Fields

The dynamics of the electrons in EM fields are described by two sets of equations, namely Maxwell′s equations and the equations of motion. The electric field strength **E** and magnetic flux density **B** steer the charged particles in vacuum. The fields, which will be shortly described by Maxwell′s equations, are coupled with the motion of particles by the *Lorentz force* **F**. The current and the charge density caused by the moving particles are assumed as a source in the Maxwell′s equations and the electric and magnetic field result in the force **F** as described in the *Lorentz equation*:

$$\mathbf{F} = q(\mathbf{E} + \mathbf{v} \times \mathbf{B}), \tag{2.1}$$

where $\mathbf{v}$ is the velocity of moving particles.

The Lorentz equation (2.1) expresses that the *electric force*, $q\mathbf{E}$, due to the **E** field exerted on the charged particle (with an *electric charge* q), changes the momentum of the particle, $\mathbf{p}$, by transferring energy to the particle. The direction of the motion of the particle guided by the *magnetic force*, $\mathbf{v} \times \mathbf{B}$, is perpendicular to the direction of motion.

Assuming a bunch of particles with charge q and mass m are at position $\mathbf{r}$ at a certain time t and are moving with the velocity $\mathbf{v}$ under the influence of the external force **F**, *the second Newton's law of motion* dictates that:

$$\mathbf{F} = \frac{d\mathbf{p}}{dt} = \frac{d(m\mathbf{v})}{dt} \qquad m = m_0. \tag{2.2}$$

If the particle moves with relativistic velocity ($\mathbf{v} \approx c$), where the normalized velocity and the relativistic momentum of a particle are given by $\beta = \mathbf{v}/c$ and $\mathbf{p} = \gamma m_0 \mathbf{v}$, respectively, Eq. (2.2) becomes

$$\mathbf{F} = \frac{d\mathbf{p}}{dt} = m_0 \frac{d(\gamma \mathbf{v})}{dt}. \tag{2.3}$$

The mass m is increased by a so-called *Lorentz factor* γ relative to the rest mass m_0, where γ is given by $1/\sqrt{1-\beta^2}$. By combining Eq. (2.2) and Eq. (2.3), the equations of motion for relativistic particles can be expressed as follows

$$\frac{d\mathbf{r}}{dt} = \mathbf{v} = \frac{\mathbf{p}}{\gamma m_0}, \tag{2.4}$$

and

$$\frac{d\mathbf{p}}{dt} = \mathbf{F} = q(\mathbf{E}(\mathbf{r}, \mathbf{t}) + \mathbf{v} \times \mathbf{B}(\mathbf{r}, \mathbf{t})). \tag{2.5}$$

2.2 Maxwell′s Equations

A complete set of basic equations describing the EM field which James Clerk Maxwell provided [80] are commonly known as Maxwell′s equations. Various mathematical models for electromagnetic fields are represented using Maxwell′s equations. These equations in fact govern all macroscopic electromagnetic phenomena [31], [147] and their differential formulation reads:

$$\nabla \cdot \mathbf{D}(\mathbf{r}, t) = \rho(\mathbf{r}, t), \tag{2.6}$$

$$\nabla \cdot \mathbf{B}(\mathbf{r}, t) = 0, \tag{2.7}$$

$$\nabla \times \mathbf{E}(\mathbf{r}, t) = -\frac{\partial}{\partial t}\mathbf{B}(\mathbf{r}, t), \tag{2.8}$$

$$\nabla \times \mathbf{H}(\mathbf{r}, t) = \frac{\partial}{\partial t}\mathbf{D}(\mathbf{r}, t) + \mathbf{J}(\mathbf{r}, t), \tag{2.9}$$

where $\mathbf{D}(\mathbf{r}, t)$ is the *electric flux density* in $\mathrm{As/m^2}$, $\rho(\mathbf{r}, t)$ is the *electric charge density* in $\mathrm{C/m^3}$, $\mathbf{B}(\mathbf{r}, t)$ is the *magnetic flux density* in $\mathrm{Vs/m^2}$, $\mathbf{E}(\mathbf{r}, t)$ is the *electric field strength* in V/m, $\mathbf{H}(\mathbf{r}, t)$ is the *magnetic field strength* in A/m, $\mathbf{J}(\mathbf{r}, t)$ is the *electric current density* in $\mathrm{A/m^2}$, $\frac{\partial}{\partial t}$ denotes the temporal derivative, and $\mathbf{r}$ and t stands for the spatial and time dependency, respectively. These equations, (2.6) - (2.9), are the differential forms of the four fundamental time-varying Maxwell's equations.

The differential forms of Maxwell′s equations can be transformed into integral forms by applying *Gauss' theorem* theorem and *Stokes' theorem.* The general integral forms of time-varying Maxwell′s equations can be written as:

$$\oiint_{\partial\Omega} \mathbf{D} \cdot d\mathbf{A} = \iiint_{\Omega} \rho(\mathbf{r}, t) \cdot dV, \tag{2.10}$$

$$\oiint_{\partial\Omega} \mathbf{B} \cdot d\mathbf{A} = 0, \tag{2.11}$$

$$\oint_{\partial\Gamma} \mathbf{E}(\mathbf{r},t) \cdot d\mathbf{s} = -\iint_{\Gamma} \frac{\partial}{\partial t}\mathbf{B}(\mathbf{r},t) \cdot d\mathbf{A}, \tag{2.12}$$

$$\oint_{\partial\Gamma} \mathbf{H}(\mathbf{r},t) \cdot d\mathbf{s} = \iint_{\Gamma} \Big(\mathbf{J}(\mathbf{r},t) + \frac{\partial}{\partial t}\mathbf{D}(\mathbf{r},t)\Big) \cdot d\mathbf{A}. \tag{2.13}$$

Gauss's law for electric fields Eq. (2.10) describes that the electric flux passing through a closed boundary $\partial\Omega$ equals to the total electric charge contained in the domain Ω. *Gauss's law for magnetism* Eq. (2.11) states that the net magnetic flux out of any closed boundary is zero. *Faraday's law of induction* Eq. (2.12) expresses that the integration of the electric field along the boundary of the closed surface $\partial\Gamma$ is equal to the negative rate of change of the magnetic flux through the surface Γ. *Ampere's law* with Maxwell's extension Eq. (2.13) specifies that the circulation of the magnetic field along $\partial\Gamma$ is equal to the flux of current density plus the time rate of change of the electric displacement through Γ. That means the change in the flux of the electric field and the electric current causes the magnetic field.

The vectorial EM field quantities involved in the above equations are interrelated through *constitutive parameters.* These parameters depend on the properties of materials in the computational domains such as *linear* and *nonlinear*, *homogeneous* and *inhomogeneous*, *isotropic* and *anisotropic* materials. Linear, isotropic, and lossless materials are employed in this research. In some cases lossy materials are also considered. The quantities $\mathbf{D}(\mathbf{r},t)$ and $\mathbf{E}(\mathbf{r},t)$ are related by *permittivity*, ε:

$$\mathbf{D}(\mathbf{r},t) = \varepsilon\mathbf{E}(\mathbf{r},t), \tag{2.14}$$

where ε is the product of the *permittivity* of vacuum, $\varepsilon_0 = 8.85418782 \cdot 10^{-12}$ F/m, and a material-dependant relative *permittivity*, ε_r. The relation between $\mathbf{B}$ and $\mathbf{H}$ can also be described by permeability μ:

$$\mathbf{B}(\mathbf{r},t) = \mu\mathbf{H}(\mathbf{r},t). \tag{2.15}$$

The permeability μ is the product of the permeability of vacuum $\mu_0 = 4\pi\cdot 10^{-7}$ H/m and a material-dependent relative permeability μ_r. Analogously, by introducing conductivity σ, the relation between electric current and electric field can be described by *Ohm's law* in a linear approximation:

$$\mathbf{J}(\mathbf{r},t) = \sigma\mathbf{E}(\mathbf{r},t) + \mathbf{J_e}(\mathbf{r},t), \tag{2.16}$$

where $\mathbf{J_e}(\mathbf{r},t)$ is the external current density.

The term displacement current in Eq. (2.13) is introduced by Maxwell as an extension to *Ampère's law.* This leads us to the conservation of charges, which is one of the crucial features of Maxwell′s equations. By applying one of the vector identities, that is the divergence of a curl equal to zero ($\nabla \cdot \nabla \times \mathbf{A}$, where $\mathbf{A}$ is any vector field), to the differential form of *Ampère's law* Eq. (2.9), its left-hand side vanishes:

$$\nabla \cdot \nabla \times \mathbf{H}(\mathbf{r}, t) = \nabla \cdot \frac{\partial}{\partial t}\mathbf{D}(\mathbf{r}, t) + \nabla \cdot \mathbf{J}(\mathbf{r}, t), \tag{2.17}$$

then it can be written as

$$0 = \frac{\partial}{\partial t}\nabla \cdot \mathbf{D}(\mathbf{r}, t) + \nabla \cdot \mathbf{J}(\mathbf{r}, t), \tag{2.18}$$

and introducing the Gauss law Eq. (2.6) to the first term of the right side of the above equation results in

$$\frac{\partial}{\partial t}\rho(\mathbf{r}, t) + \nabla \cdot \mathbf{J}(\mathbf{r}, t) = 0, \tag{2.19}$$

this is called the continuity equation. The integral form of this equation can be obtained by taking the volume integral and using Gauss's theorem for the volume integral of the divergence of a vector field:

$$\frac{\partial}{\partial t}\iiint_{\Omega} \rho(\mathbf{r}, t) \cdot dV + \oiint_{\partial\Omega} \mathbf{J}(\mathbf{r}, t) \cdot d\mathbf{A} = 0. \tag{2.20}$$

The integral conservation equation Eq. (2.19) describes that the rate of change of electric charge within the domain Ω is equal to the rate of flow of electric current through the boundary $\partial\Omega$ of Ω. That means the density of charge in Ω changes only if the current of charge flows in or out of Ω.

2.2.1 The Electromagnetic Wave and Helmholtz Equations

The EM wave equations are solutions of Maxwell′s equations. One approach in order to do that is to first decouple the equations for $\mathbf{E}$ and $\mathbf{H}$ by taking the curl of the differential form of *Faraday's law* Eq. (2.8) on both sides:

$$\nabla \times (\nabla \times \mathbf{E}(\mathbf{r}, t)) = \nabla(\nabla \cdot \mathbf{E}(\mathbf{r}, t)) - \nabla^2\mathbf{E}(\mathbf{r}, t) = -\frac{\partial}{\partial t}\Big(\nabla \times \mathbf{B}(\mathbf{r}, t)\Big). \tag{2.21}$$

The standard vector identity is applied in the above Eq.: $\nabla \times \nabla \times \mathbf{A} = \nabla(\nabla \cdot \mathbf{A}) - \nabla^2\mathbf{A}$, where $\mathbf{A}$ is any vector field. The order of curl and the time derivative is changed in the right-hand side of the above equation. Then, the curl of the magnetic field will be substituted by the right side term of (2.9) (*Ampère's law*) in order to eliminate $\mathbf{B}(\mathbf{r}, t)$ and the *constitutive* relations stated in Eq (2.14) for electric flux $\mathbf{D}(\mathbf{r}, t)$ is applied:

$$\nabla(\nabla \cdot \mathbf{E}(\mathbf{r}, t)) - \nabla^2\mathbf{E}(\mathbf{r}, t) = -\frac{\partial}{\partial t}\Big(\varepsilon\mu\frac{\partial}{\partial t}\mathbf{E}(\mathbf{r}, t) + \mu\mathbf{J}(\mathbf{r}, t)\Big). \tag{2.22}$$

For further simplification, the term $\nabla(\nabla \cdot \mathbf{E}(\mathbf{r},t))$ is substituted by Eq. (2.6)) and with some rearrangement the equation becomes:

$$\nabla^2 \mathbf{E}(\mathbf{r},t) = \varepsilon\mu \frac{\partial^2 \mathbf{E}(\mathbf{r},t)}{\partial t^2} + \nabla\Big(\frac{\rho(\mathbf{r},t)}{\varepsilon}\Big) + \mu \frac{\partial}{\partial t}\mathbf{J}(\mathbf{r},t), \tag{2.23}$$

this is called the *wave equation for electric fields.* Similarly, by eliminating **E** in favor of **H**, the *wave equation for the magnetic fields* can be obtained:

$$\nabla^2 \mathbf{H}(\mathbf{r},t) = \varepsilon\mu \frac{\partial^2 \mathbf{H}(\mathbf{r},t)}{\partial t^2} - \nabla \times \mathbf{J}(\mathbf{r},t). \tag{2.24}$$

The wave equations describe the propagation of EM waves through different medium. Here, the homogeneous medium is considered. In a vacuum case, where the sources for electric and magnetic fields (charges and currents) don't exist, the wave equations for **E** and **H** Eq. (2.23) and (2.24) then become

$$\nabla^2 \mathbf{E}(\mathbf{r},t) = \varepsilon\mu \frac{\partial^2}{\partial t^2}\mathbf{E}(\mathbf{r},t), \tag{2.25}$$

and

$$\nabla^2 \mathbf{H}(\mathbf{r},t) = \varepsilon\mu \frac{\partial^2}{\partial t^2}\mathbf{H}(\mathbf{r},t), \tag{2.26}$$

In case of the sinusoidal time-dependent fields at the fixed angular frequency ω, the time-harmonic form can be derived from the above wave equations by introducing the complex valued functions of

$$\mathcal{E}(\mathbf{r},t) = e^{-i\omega t}\mathbf{E}(\mathbf{r}) \tag{2.27}$$

and

$$\mathcal{H}(\mathbf{r},t) = e^{-i\omega t}\mathbf{H}(\mathbf{r}). \tag{2.28}$$

Then by putting Eq. (2.27) and Eq. (2.28) into Eq. (2.25) and Eq. (2.26), respectively, the *Helmholtz wave equation* can be written as

$$\nabla^2 \mathcal{E}(\mathbf{r}) = k^2 \mathcal{E}(\mathbf{r}), \tag{2.29}$$

and

$$\nabla^2 \mathcal{H}(\mathbf{r}) = k^2 \mathcal{H}(\mathbf{r}), \tag{2.30}$$

where the constant k is the wave number given by $\frac{\omega}{c}$. Here c represents the speed of light equal to $\sqrt{\frac{1}{\varepsilon\mu}}$ and ω denotes angular frequency.

2.2.2 Electromagnetic Wave in a Closed Structure

The *Helmholtz wave equations* ((2.29) and (2.30)) are second-order partial differential vector equations, which describe the propagation of EM waves through a medium. Finding solutions for these equations in a bounded region of interest requires boundary conditions (BC). There are different types of BCs to solve boundary value problems including *Dirichlet* boundary condition, where the value of the vector function is specified on the boundary $\partial\Omega$, *Neumann* boundary condition, where the derivative of the vectors is prescribed on $\partial\Omega$, and *mixed* boundary condition, that allows imposing several BCs on different parts of the boundaries.

The EM wave can be confined in a closed metal structure as in an RF cavity and can also be guided through partly enclosed conducting structures such as *waveguides.* Such structures are usually considered to be made of perfect conductor, where the material is assumed to have infinite electric conductivity ($\sigma = \infty$)[1]. This assumption implies that the losses are zero at the surface. The medium is therefore referred to as *perfect electric conducting* (PEC). Mostly either PEC or perfect magnetic conductor (PMC)[2] BCs are appropriate in the sense of SRF injector simulations, where the cavity could be modeled by PEC material and filled with vacuum. Thus, in case of perfect conducting boundary, the electric fields should satisfy the following BCs

$$\mathbf{E} \times \mathbf{n}|_{\partial\Omega} = 0 \tag{2.31}$$

and

$$\mu\mathbf{H} \cdot \mathbf{n}|_{\partial\Omega} = 0 \ , \tag{2.32}$$

where $\mathbf{n}$ is the unit vector normal to the surface. The boundary conditions stated in (2.31) and (2.32) are derived from *Gauss's law for electric fields* Eq.(2.10) and *Gauss's law for magnetism* Eq. (2.11), respectively, under some conditions.

For PMC, the tangential component of magnetic field vanishes and this condition can mathematically be stated as

$$\mathbf{H} \times n|_{\partial\Omega} = 0 \tag{2.33}$$

and

$$\mu\mathbf{E} \cdot n|_{\partial\Omega} = 0. \tag{2.34}$$

The symmetric boundary condition for electric field can be also applied in case of two media with the same *permittivity*, otherwise the tangential field components should be continuous at the boundary between the two media.

Moreover, the boundary of the structure could be defined with a so-called *waveguide port boundary condition.* The port is used as feed to provide excitation, i.e., initial

---

[1] The wall losses due to energy conversion to thermal energy can be calculated a posteriori by the so-called power loss method that is based on perturbation approach.

[2] PMC BC is often used as symmetry BC in order to exploit geometrical symmetries and thus significantly reduce the computational costs.

fields, to the connected computational model. This includes exciting the structure with an EM field and at the same time, absorbing the returning EM field.

One example of the time-harmonic fields are plane waves. Assuming the plane wave propagates along one direction in space, e.g. in the z-direction, the propagating mode is referred to as *transverse electric* and *magnetic* (TEM) *mode* if **E** and **B** fields are transverse to the direction of propagation. The EM waves in unbounded vacuum are in fact TEM, which is characterized by $E_z = 0$ and $H_z = 0$, where the axis of the propagation is assumed as the z-axis. In case of bounded media, TEM waves can be propagated in a two-conductor lines. For instance in a coaxial line structure a single TEM *mode* is the dominant mode. The time varying fields in the coaxial structure can be excited by a *waveguide port* with appropriate conditions at the boundaries. When it comes to a closed-cavity, two types of modes could be excited. The modes, i.e. *transverse electric* (TE) mode, where **E** is always transverse to the direction of propagation, and *transverse magnetic* (TM) mode, where **H** is always transverse to the direction of propagation, can propagate in the structure above their cut off frequency, which is determined by the size of the structure. These modes are associated with mode numbers, namely **n**, **m** and **p**, which represent the variation of field in x, y and z directions in Cartesian coordinate, respectively. The TM mode, namely TM_{010}, is widely used for acceleration of particles in RF cavities.

The field components of the TEM mode in the coaxial line will be briefly discussed here, as this structure is a region of interest in this research. As noted above, the coaxial transmission line is considered to be centered on the z-axis in the cylindrical coordinate system (r, ϕ, z). The inner and outer coaxial conductors are assumed to be prefect conductors, and the gap between them is filled with a perfect dielectric medium, i.e. $\sigma = 0$. As long as there are no electric and magnetic field components in the direction of propagation for a TEM wave, the transverse field of a TEM wave is basically equivalent with the static field, which implies that the electric field can be expressed as a gradient of some scalar potential. The expressions of **E** and **H** in the scalar potential Φ and the vector potential **A**, which are functions of space and time, are usually written as

$$\mathbf{E} = -\nabla\Phi - \frac{\partial \mathbf{A}}{\partial t}, \tag{2.35}$$

and

$$\mathbf{H} = \frac{1}{\mu}\nabla \times \mathbf{A}, \tag{2.36}$$

where Φ and **A** refer to the *electric scalar potential* and *magnetic vector potential* respectively. According to the Lorenz condition for potentials (*Lorenz gauge*)[76], the relation between Φ and **A** is expressed by

$$\nabla \cdot \mathbf{A} = -\mu\epsilon\frac{\partial \Phi}{\partial t}. \tag{2.37}$$

In the case of source free region (i.e $\rho = 0$ and $\mathbf{J} = 0$), the homogeneous wave equation for the scalar potential Φ in the gap is obtained by substituting Eq. (2.35) into Eq. (2.6) and by imposing the *Lorenz gauge*, this results

$$\nabla^2\Phi = \mu\epsilon\frac{\partial^2\Phi}{\partial t^2}. \tag{2.38}$$

The wave equation can be solved in different coordinate systems. Here we may assume that the fields produced in the coaxial line are cylindrically symmetric. Thus, the representation of the Laplace operator ∇^2 for the above scalar (Helmholtz's) wave equation (2.38) involving a quantity ψ in a cylindrical coordinate system (r, ϕ, z) can be expressed as

$$\frac{1}{r}\frac{\partial}{\partial r}(r\frac{\partial\psi}{\partial r}) + \frac{1}{r^2}\frac{\partial^2\psi}{\partial\phi^2} - \beta^2\psi = -k^2\psi. \tag{2.39}$$

As noted before, the fields are assumed to have no azimuthal dependence ($E_z = 0$ and $H_z = 0$), then the cutoff wave-number, $k_c = (k^2 - \beta^2)^{1/2}$, is zero for TEM waves as $k^2 = \beta^2$ here. In this case the electric and magnetic field in terms of scalar potential can be approximated as [81]

$$\mathbf{E}_r = -\frac{\partial\Phi}{\partial r} = \frac{\Phi_0}{r\ln(\frac{r_{out}}{r_{in}})}e^{i(k-\omega t)}, \qquad (r_{in} < r < r_{out}), \tag{2.40}$$

and

$$\mathbf{B}_\phi = \frac{\mathbf{E_r}}{v}, \tag{2.41}$$

where r_{in} and r_{out} denote the inner and outer radius of the coaxial transmission line, respectively.

2.3 Numerical Solution of Maxwell's Equations

The analytical solution of Maxwell's equations for EM fields exists only for very simple geometrical structures. For complex geometries, for instance a TESLA-like (SRF) cavity, a numerical solution is required to solve the *Helmholtz equation*. Therefore, different numerical methods have been developed over the last few decades to provide a solution for a system that is represented by partial differential equations (PDEs). The common approaches, such as finite element methods (FEM) [32], finite integration technique (FIT) [155], [156] and finite-difference time-domain (FDTD), [170], are based on either differential or integral form of Maxwell′s equations. The detailed mathematical formulation and the specific applications of these numerical methods are described in vast number of publications along with [170], [155], [29], [28], [147].

The basic algorithm of the latter two approaches for homogenous media, namely FIT and FDTD are similar. FIT is even considered as a generalization of FDTD, where the computational model is approximated by *Yee cell* [170]. Besides, in contrast to FDTD, and FEM, FIT discretizes the integral form of Maxwell′s equations. As the numerical simulation was based on FIT and FEM in this work, the basics of the two approaches will be briefly discussed below.

2.3.1 Finite Integration Technique

Finite integration technique is a discretization scheme for solving Maxwell's equations in their integral form which is suitable for modern computer simulations. It discretizes Maxwell′s equations in space and time. FIT is initially introduced by T. Weiland [155], [156] in 1977 and has been implemented in different simulation software to solve various EM wave, static and quasistationary problems. The development has been continued with the involvement of other scientists. Moreover, the technique has been adapted for a wide range of applications. FIT discretizes the finite volume $\Omega \in \mathcal{R}^3$ of a simulated computational domain and provides the numerical formulations for static problems and in the time as well as in the frequency domain.

A continuous Maxwell's formulation has to primarily be transformed into a discrete form using a mesh to obtain a numerical solution for the EM field problems. The accuracy of this solution depends on the mesh cell size (grid size). A highly accurate solution can be achieved from a perfectly fine mesh. However, for explicit time-integration schemes such as in FDTD or FIT, the smallest grid size used in the discretization of the structure has a direct impact on the discrete-time step width, Δt. There the field components are recursively updated to compute the new values according to the previous calculation. The relation between the mesh cell size and the time step is given by *Courante-Friedrich-Levy* condition:

$$\Delta t \leq \frac{\varepsilon\mu}{\sqrt{\frac{1}{\Delta x^2} + \frac{1}{\Delta y^2} + \frac{1}{\Delta z^2}}}, \tag{2.42}$$

where Δx, Δy, Δz represent spatial grid sizes in the Cartesian coordinate direction x, y and z, respectively. Thus, in case of a complex structure which demands a very fine mesh (a very small grid size) that might result in a large total number of mesh cells, a very long computational time and powerful computing infrastructure is required. In order to address these issues in our simulation, a *local mesh refinement* (LMR), as implemented in CST MICROWAVE STUDIO® (CST MWS) [3], is considered along a mesh convergence study which should satisfy Eq. (2.42). LMR therefore ensures that a higher accuracy in the critical region of interest is obtained by refining the mesh locally, and at the same time the total number of mesh cells used for the whole computational model is reduced. Basically, the *Courante-Friedrich-Levy* condition Eq. (2.42) needs to be fulfilled for explicit time integration schemes in order to avoid instability.

The FIT employs two computational grids for the decomposition of spatial domain Ω, which is here considered to be a brick shape, in the Cartesian coordinate. The *primary grid*, G decomposed into FIT cells V_i with I, J and K nodes in x, y and z direction, respectively. Then, the total number of nodes, N_p, in G is given by $N_p = I\ J\ K$. The secondary grid so called *dual grid*, $\widetilde{G}$, is placed by a half grid step of the *primary grid*, G, in each direction as shown in Fig. 2.1. The field

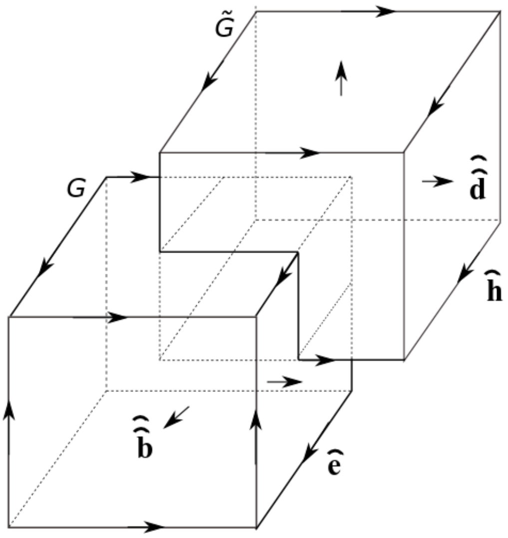

Figure 2.1: A *primary grid*, G and *dual grid*, $\widetilde{G}$ for a FIT cell on the Cartesian grid system. The allocation of the field components on the three dimentional staggered grid. Adapted from [147].

components are specified on the staggered grid and then generate so-called *Maxwell's Grid Equations* (MGEs). The derivation of these equations using a single FIT cell in Cartesian coordinate is presented in [147]. Then, the representation of MGEs of the integral form of Maxwell′s equations (2.10) - (2.13) leads to a unique solution [29], [41]:

$$\widetilde{\boldsymbol{\mathcal{S}}}\,\widehat{\widehat{\mathbf{d}}} = \widehat{\widehat{\boldsymbol{\varrho}}}, \tag{2.43}$$

$$\boldsymbol{\mathcal{S}}\,\widehat{\widehat{\mathbf{b}}} = 0, \tag{2.44}$$

$$\boldsymbol{\mathcal{C}}\,\widehat{\mathbf{e}} = -\frac{\partial}{\partial t}\widehat{\widehat{\mathbf{b}}}, \tag{2.45}$$

$$\widetilde{\boldsymbol{\mathcal{C}}}\,\widehat{\mathbf{h}} = -\frac{\partial}{\partial t}\widehat{\widehat{\mathbf{d}}} + \widehat{\widehat{\mathbf{j}}}, \tag{2.46}$$

where the *electric grid voltages* $\widehat{\mathbf{e}}$ and the *magnetic fluxes* $\widehat{\widehat{\mathbf{b}}}$ are located on the edges and facets of the primary grid G whereas the *magnetic grid voltages* $\widehat{\mathbf{h}}$ and the *electric fluxes* $\widehat{\widehat{\mathbf{d}}}$ are defined on the edges and facets of its dual grid $\widetilde{G}$. The *electric grid charge* $\widehat{\widehat{\boldsymbol{\varrho}}}$ and the *electric grid current* $\widehat{\widehat{\mathbf{j}}}$ are allocated on the dual grid. The topology matrices $\widetilde{\boldsymbol{\mathcal{S}}}$, $\boldsymbol{\mathcal{S}}$, $\boldsymbol{\mathcal{C}}$ and $\widetilde{\boldsymbol{\mathcal{C}}}$ represent discrete div- and curl- operators on the grid G and dual grid $\widetilde{G}$. The tilde indicates that the operator is acting on the dual grid.

In the discretization of FIT, the relation between the state variables on G and $\widetilde{G}$ is described by constitutive material equations. These equations introduce the *discrete* *material matrices* such as the matrix of permittivity $\mathbf{M}_\epsilon$, the matrix of permeability $\mathbf{M}_\mu$, and the matrix of conductivity $\mathbf{M}_\sigma$ and read in the linear and time-invariant case as follows:

$$\widehat{\widehat{\mathbf{d}}} = \mathbf{M}_\epsilon \widehat{\mathbf{e}}, \tag{2.47}$$

$$\widehat{\widehat{\mathbf{b}}} = \mathbf{M}_\mu \widehat{\mathbf{h}}, \tag{2.48}$$

$$\widehat{\widehat{\mathbf{j}}} = \mathbf{M}_\sigma \widehat{\mathbf{e}}. \tag{2.49}$$

Consequently, the EM field problem can be now solved according to these matrix equations ((2.43) - (2.49)) on the discrete grid space.

As it is noted, the FIT method can also be formulated in the frequency domain by applying the method of complex phasor notation. Then the time derivative $\frac{d}{dt}$ in Eq. (2.61) and in Eq. (2.62) of MGEs is substituted with the factor $i\omega$, and the phasor form of discrete Maxwell's equations in the frequency domain becomes

$$\widetilde{\boldsymbol{\mathcal{S}}}\ \underline{\widehat{\widehat{\mathbf{d}}}} = \underline{\widehat{\widehat{\widehat{\boldsymbol{\varrho}}}}}, \tag{2.50}$$

$$\boldsymbol{\mathcal{S}}\ \underline{\widehat{\widehat{\mathbf{b}}}} = 0, \tag{2.51}$$

$$\boldsymbol{\mathcal{C}}\ \underline{\widehat{\mathbf{e}}} = -i\omega \underline{\widehat{\widehat{\mathbf{b}}}}, \tag{2.52}$$

$$\widetilde{\boldsymbol{\mathcal{C}}}\ \underline{\widehat{\mathbf{h}}} = -i\omega \underline{\widehat{\widehat{\mathbf{d}}}}\ +\ \underline{\widehat{\widehat{\mathbf{j}}}}, \tag{2.53}$$

FIT hexahedral (HEX) based meshes are used in most cases of the computational results presented in the following chapters. However, in some parts of this work, FEM tetrahedral (TET) based meshes were also used. Hence, a short description of it will be given in the next section.

2.3.2 Finite Element Method

Finite element method [32] is one of the frequently used discretization methods for solving EM problems that discretizes Maxwell's equations on unstructured grids, where most often triangular and TET elements are employed. It provides an approximate solution of the PDEs, for instance, wave equation, Poisson equation, and Fourier's law. These are examples of elliptic, hyperbolic, and parabolic PDEs, respectively. Then these equations will be solved by providing appropriate boundary conditions.

The approaches based on the structured grids, e.g. FDTD or FIT, provide a very efficient numerical algorithm to solve the PDE. However, it is often not suitable for discretizing complex geometries. In the case of unstructured grids, the computational domain is decomposed into different subdomains, and for each subdomain, the mesh is generated separately. The flexible nature of unstructured grids allows approximating any complex geometry, in contrast to structured grids.

The finite element method discretizes the computational domain Ω using the sub-domain elements as already noted. The elements have a finite number of nodal points, i.e., the order of polynomial in x, y, and z directions called the *finite elements*. The finite element cells can be, in three-dimensional cases, tetrahedral, hexahedron, and prism. The field variables are interpolated over the element domain using interpolation functions. It follows the establishment of a system of algebraic equations for each finite element (e) by applying *weighted residual method* (e.g., *Galerkin method*), using the governing equation of problem, that includes all the sources and boundary information on the boundaries, $\partial\Omega$. The construction of the system of the finite element equation results in the matrix equation, which relates the nodal values of the unknown function to other parameters. Then the solution of the system is obtained by solving the system of equations, either linear or nonlinear, using a direct or an iterative method.

Assume that the problem to be solved with the unknown function is u in bounded section Ω of the physical domain D. Moreover, assuming that the source (excitation function) is s, the governing equation can be written as $L[u(x)] = s(x)$, where L is a linear differential operator. And its boundary condition can be described by $B(u) = 0$, which is defined on $D \subseteq \partial\Omega := \Gamma$. An approximation of the solution, which is obtained by expansion of the unknown function in a finite number of *basis functions*, $\varphi_i(x)$, can be expressed as

$$u^e(x) \approx \tilde{u}^e(x) = \sum_{i=1}^{n^e} u_i^e \varphi_i^e(x), \qquad x \in \Omega, \tag{2.54}$$

where $u_i^e(i = 1, ..., N^e)$ are unknown coefficients in the expansion that corresponds to the nodal values of $\tilde{u}(x)$. The *basis functions*, $\varphi_i(x)$, can be either a vectorial or a scalar function depending on the type of the problem. In case of $u(x,t)$, where u also depends on time, the expression in (2.54) becomes

$$u^e(x,t) \approx \tilde{u}^e(x,t) = \sum_{i=1}^{n^e} u_i^e(t) \varphi_i^e(x), \tag{2.55}$$

As an example a solution of *Helmholtz wave equation* for electric field Eq. (2.29) can be formulated using the Nédélec elements approach [89], [90]. In this equation the unknown variable is the electric field and the expansion becomes $\mathbf{E} = \sum_{j=1} u_j \varphi_j^{3D}$, where φ_j^{3D} are the edge-based vector basis functions and u_j, $j = 1, ..., n$ denotes the expansion coefficients of the basis. These unknown weighting coefficients are collected in a vector variable $\mathbf{u}$. Then, the system of equation can be represented by

$$A^{3D}\mathbf{u} - B^{3D}\mathbf{u} = 0, \tag{2.56}$$

where the matrices A^{3D} and B^{3D} are specified by

$$A_{ij}^{3D} = \iiint_{\Omega} (\nabla \times \varphi_i^{3D}) \cdot (\nabla \times \varphi_j^{3D}) d\Omega, \tag{2.57}$$

and

$$B_{ij}^{3D} = \iiint_{\Omega} (\varphi_i^{3D} \cdot \varphi_j^{3D}) d\Omega, \tag{2.58}$$

respectively. The boundary conditions for (2.56) have to be considered in order to establish the total system of equations.

2.4 Particle-in-Cell

The Particle-in-Cell (PIC) [16], [17] simulation method is usually applied for the computation of the motion of charged particles in the presence of EM fields. PIC code has been developed in many simulation tools and applied in various computational applications. Among them, Track3P module from ACE3P [68], [92], Magic [161], [77], MOEVE PIC Tracking [79], [78], MultiPac [175], EGUN and IGUN [59], [12], KARAT [111], [7], CST PARTICLE STUDIO® (CST PS) solver from CST STUDIO SUITE® [128], [53], [23], [13], [18], [98], can be mentioned. The latter tool combines EM field simulation, multi-particle tracking and advanced probabilistic emission models, which are not incorporated en masse in most codes.

There are two basic steps to determine the motion of charged particles: calculating the EM fields by solving Maxwell's equations [cf. Eq. (2.6) - (2.9)] along with the boundary conditions and then computing the motion of particles due to the fields applied on the particles by solving the equations of motion (in case of non-relativistic)

$$\frac{d\mathbf{r}_i}{dt} = \mathbf{v_i}, \quad i = 1, ..., N \tag{2.59}$$

and

$$m_i \frac{d\mathbf{v}_i}{dt} = \mathbf{F_i} = q_i \left(\mathbf{E}(\mathbf{r}_i) + \mathbf{v}_i \times \mathbf{B}(\mathbf{r}_i) \right), \quad i = 1, ..., N, \tag{2.60}$$

where F_i is the *Lorentz force* acting on the i^{th} particle. In general, the PIC algorithm works in the time domain for tracking the trajectory of the particle and includes different parts in its computation, namely the field solver, the particle mover with appropriate boundary conditions and the particle source, weighting of particles and fields. Basic scheme of computational cycle of the PIC solver is visualized in Fig. 2.2. Each part is briefly discussed below.

The PIC code, similar to FIT and FEM, approximates the continuous computational domain by a discrete number of cells. The physical quantities (e.g., charge

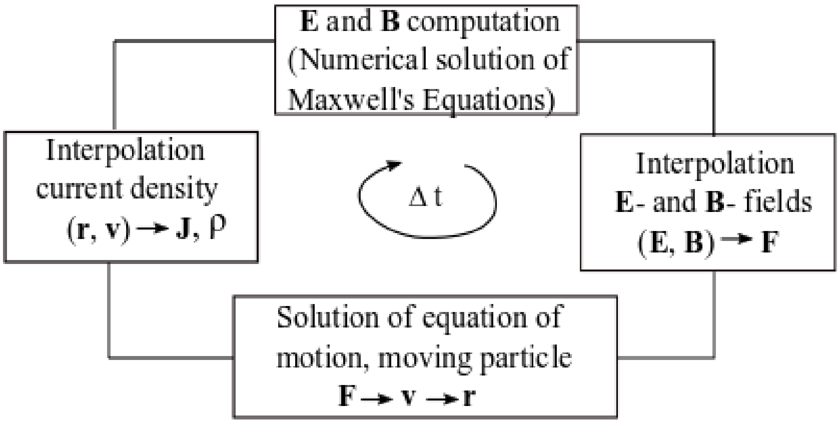

Figure 2.2: Partile-in-Cell algorithm implemented in PIC solver of CST Particle Studio®.

densities) are computed in these cells at the given time moments. A macroparticle[3] with a given charge, mass and velocity is initially located in the cell at position $\mathbf{r}$ at time $t = 0$, according to any given distribution, such as uniform or Gaussian distribution. The latter was employed to for the particle emission source. Particles are defined over the surface at $\mathbf{r}$ with the initial velocity $\mathbf{v} = 4$ eV. The emission model will be explained shortly.

Then the charge density of the simulation particle is assigned onto the grid nodes of computational cells, which is referred as *charge weighting.* In order to allocate the densities on the grid points, there are different interpolation schemes, depending on the accuracy required and the computational cost. For instance, *a first order weighting* or *area weighting* can be employed in the two, or three-dimensional space [16]. In this approach, in general, the closest node from which the particle originated receives the largest fraction. Consequently, the total charge density $\rho(t = 0, \mathbf{r})$ is computed on the grid.

The prior computed or self-consistent **E** and **B** fields are considered over the whole simulation domain. The fields can be computed by solving Maxwell's curl equations

$$\mathcal{C}\,\widehat{\mathrm{e}} = -\frac{\partial}{\partial t}\widehat{\widehat{\mathbf{b}}}, \tag{2.61}$$

and

$$\widetilde{\mathcal{C}}\,\widehat{\mathbf{h}} = -\frac{\partial}{\partial t}\widehat{\widehat{\mathbf{d}}} + \widehat{\widehat{\mathbf{j}}}, \tag{2.62}$$

---

[3] Macroparticles refer to a rescale of several real particles to make the computation efficient. That means one particle in the simulation represents many physical particles. This transformation is possible as the ratio charge-to-mass is invariant.

which are discussed in Section 2.3.1. One of possible schemes to calculate fields numerically is a *leap frog* scheme [170]. For example, *leap frog* scheme based the time domain FIT solver calculates $\widehat{\mathbf{e}}$ and $\widehat{\widehat{\mathbf{b}}}$ in the discrete time moments at time samples separated by half a time step Δt. Thus both are located interchangeably between the consecutive time samples. For example, while $\widehat{\mathbf{e}}$ is defined at $t = n\Delta t$, $\widehat{\widehat{\mathbf{b}}}$ is at $t = (n + 1/2)\Delta t$ time moments. Then, in the case of loss free, using a time central differences, the two curl equations can be written as

$$\widehat{\widehat{\mathbf{b}}}^{(n+1/2)} = \widehat{\widehat{\mathbf{b}}}^{(n-1/2)} - \Delta t \boldsymbol{\mathcal{C}}\widehat{\mathbf{e}}^{(n)}, \tag{2.63}$$

and

$$\boldsymbol{\mathcal{C}}\widehat{\mathbf{e}}^{(n+1)} = \boldsymbol{\mathcal{C}}\widehat{\mathbf{e}}^{(n)} + \Delta t \mathbf{M}_{\epsilon}^{-1}\left(\widetilde{\boldsymbol{\mathcal{C}}}\mathbf{M}_{\mu^{-1}}\widehat{\widehat{\mathbf{b}}}^{(n+1/2)} - \widehat{\widehat{\mathbf{j}}}^{(n+1/2)}\right), \tag{2.64}$$

considering the constitutive material equations. Then, similar to the charge interpolation, the fields must be calculated at the particle. Therefore, the fields are then interpolated from the mesh to the particle position via *field weighting*. As a result, the particles move relative to the fields and occupy any position in grid space. For *charge and field weighting*, a higher-order weighting, such as quadratic and cubic splines, results in a higher accuracy by smoothening the fluctuation of densities and fields; however, they require a higher computational cost.

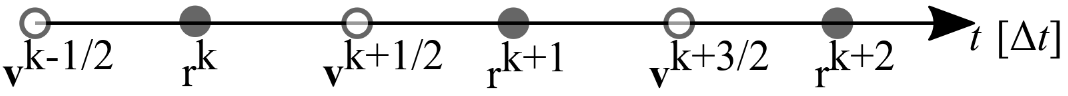

Figure 2.3: The time-centered *Leap frog* method to calculate the velocities and positions of particles.

Once the force $\mathbf{F}_i$ due to the fields exerted on each particle is obtained, the new positions and velocities of the particle can be computed by solving the equations of motion (Eq. (2.66) and Eq. (2.60)) by introducing, similar to the above, Yee's *Leap Frog* method [170]. Similarly, the PIC code calculates a physical quantities A in the discrete time moments based on a time integration scheme of the *Leap Frog* method, where the computational time moments can be expressed as: $t \to t_k = t_0 + k\Delta t$ and $A(t) \to A_k = A(t = t_k)$ with $k = 0, 1, 2, ...$ where t is time, t_0 is the initial moment and Δt is the time step. Therefore, the first order differential equations (Eq. (2.66) and Eq. (2.60)) can be replaced by the *finite-difference equations* using *Leap Frog* method [39]:

$$\frac{\mathbf{v}_i^{k+1/2} - \mathbf{v}_i^{k-1/2}}{\Delta t} = \frac{\mathbf{F}_i^k}{m_i}, \qquad \frac{\mathbf{r}_i^{k+1} - \mathbf{r}_i^k}{\Delta t} = \mathbf{v}_i^{k+1/2}, \tag{2.65}$$

and then the *Lorentz force* $\mathbf{F}_i^k$ due to the electric $\mathbf{E}_i^k$ and magnetic $\mathbf{B}_i^k$ fields acting on the i^{th} particles can be rewritten as

$$\mathbf{F}_i^k = q\left(\mathbf{E}_i^k + \frac{\mathbf{v}_i^{k+1/2} + \mathbf{v}_i^{k-1/2}}{2} \times \mathbf{B}_i^k\right), \tag{2.66}$$

The method calculates the positions $\mathbf{r}_i$ and velocities $\mathbf{v}_i$ of particles at time samples separated by half a time step Δt as illustrated in Fig. 2.3. The particle velocity $\mathbf{v}$ at $t = (k + 1/2)\Delta t$ is computed from the velocity at the previous step $t = (k - 1/2)\Delta t$ using the force calculated at time $t = 0$.

2.5 Multipactor Phenomenon

The synchronization between the RF electric field and the *secondary electron emission* (SEY) phenomenon under vacuum condition may result in electrons avalanche, this effect is called *multipactor* [148]. This limits the maximum electric field gradient of SRF cavities as noted in Chapter 1. Multipactor discharge has been studied theoretically and experimentally in different structures, for example, rectangular waveguides [118], [93], circular waveguides [119], coaxial lines [144], and accelerating cavities [173], [122], [121] and others. Furthermore, some experiments and computer simulation results show that MP can also exist in SRF cavities, for e.g. Cornell ERL injector cavity [46] and KEK Ichiro and KEKB crab cavity [86], [22] as well as at the photocathode of SRF injector at ELBE [134], [142] and in the HOM couplers of TESLA like cavity at DESY [69].

The basic principle is that the *primary electrons* are released from one of the structure's walls. Such electrons, which are undesirable, are triggered by certain conductive conditions as described before. RF fields accelerate these free electrons and impact the surface at an angle (θ_0). The electrons interact with the material and its structure and transfer energy. Consequently, further electrons excited from inside of the material and escape the surface depending on their impacting energy and angle. They are denoted as *secondary electrons.* Therefore, the MP takes place in the case of the electron avalanche build-up due to the enhancement of these secondary electrons. The population of the secondary electrons mainly depends on the surface characteristics, the impact energy of the primary electron (U_0) and the impact angle of the primary electron (θ_0) [42]. This phenomenon of resonant electron multiplication may cause degradation of vacuum, local heating, power reflection and fluctuation, sparking, and surface damage. Moreover, it may lead to thermal breakdown [96]. Therefore, this undesired scenario must be controlled.

In this thesis, the source of the emission of the electrons is assumed to have a Gauss emission type model, as illustrated in Fig. 2.4. CST Particle Studio® (CST PS) incorporates various types of emission models, some of which are *DC* emission, *Gauss* emission, *field* emission and *fixed* emission models. For MP, Gauss emission

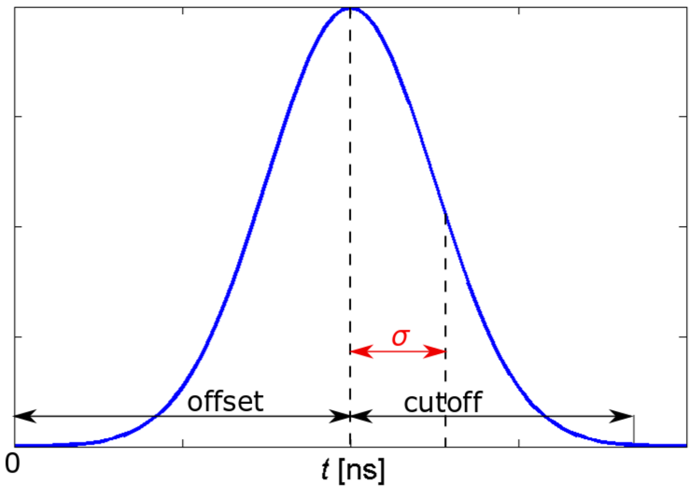

Figure 2.4: A Gaussian emission model of initial charged particles distribution as a function of time.

model is suitable [108]. This model allows to terminate the emission of particles after a certain time, as MP simulation only requires an initial seed. Then further stage of emission process is governed by the secondary emission properties of the surface material and by the dynamics of the RF fields. A macroparticle with a homogeneous type of charged particles, e.g. $q_t = 10^6\ e^-\ [C]$, is considered at the position $\mathbf{r}$ and uniformly distributed over the emission area. The particle motion is described by the ideal path (coordinate), s[4]. The distribution of the charge $q(s)$ as a function of coordinate s is then given by

$$q(s) = q_t \frac{1}{\sqrt{2\pi}\sigma} e^{\left(-\frac{s^2}{2\sigma^2}\right)}. \tag{2.67}$$

The model parameters used for this research are presented in chapter three.

The common types of MP in the literature are: *one-point* (*one-sided*) MP, where the electron trajectories refer only to one surface of the structure, and *two-sided MP*, where the electron hits two different surfaces of the structure while *two-point MP* refers to the electron hitting two opposite impact sites on the same surface.

A *one-point MP* is primarily discovered in a pill-box like cavities. This type of MP occurs by repeatedly impacting the same surface and roughly the same site where the electron was initially emitted. The transit time of the electrons between impacts needs to be an integer number of RF periods [148]. However, the latter might not always be true as the one-point MP may take place without requiring an integer number of RF periods between impacts [54]. An example of a trajectory of first to third order one-point MP is illustrated in Fig. (2.5). The *one-sided MP* mainly

---

[4] Ideal path is referred to as any given arbitrary path that the particle is supposed to follow

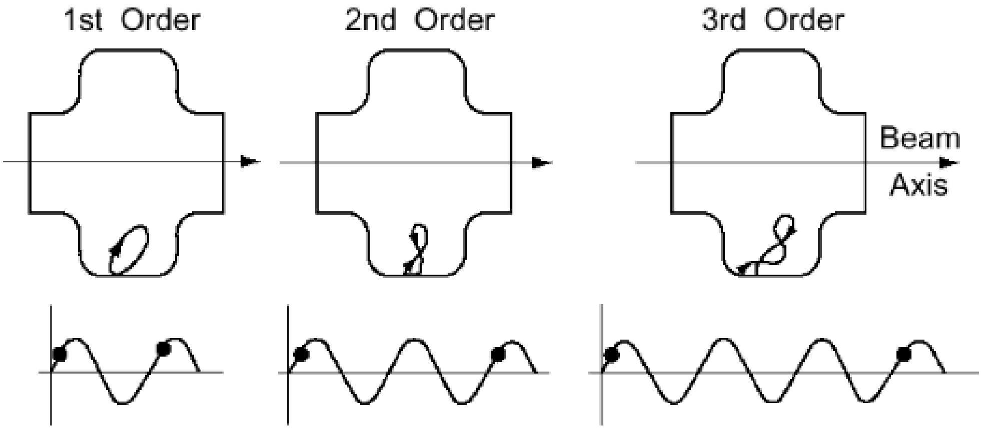

Figure 2.5: A visualization of one-point multipacting for the first three orders at the cavity wall. Reprinted from [96] with permission.

occurs in the region where the magnetic field is distributed homogeneously and the electric field has a normal component. For SEY greater than unity, a possible MP barrier for each order of one-point MP in the cavity can be approximated by [14], [95], [44]

$$f/N \propto eB/2\pi m \tag{2.68}$$

where f denotes RF frequency, N order of MP, B local magnetic field, e and m the electron charge and mass, respectively. The corresponding impact energy, U, is given by

$$U \propto \frac{e^2\mathbf{E}_n^2}{m\omega_g^2}, \tag{2.69}$$

where $\mathbf{E}_n$ is the normal electric field. The cavity's one-point MP was tackled by developing a proper cavity shape such as spherical or elliptical [65], [66]. This design compels the emitted electron to drift toward the equator, where the normal electric field $\mathbf{E}_n$ is nearly zero, and as a result, the MP is suppressed.

Another example of a *one-sided MP* is a study of MP in a coaxial line structure with standing wave fields. According to [127], the power that assists MP to occur in a coaxial structure can be predicted by the *scaling law*:

$$P_{\text{one-point}} \sim (fd)^4 Z, \tag{2.70}$$

where d stands for a size parameter and Z for the line impedance. The associated average impact energy of the electrons can be approximated by

$$U_a \sim (fd)^2. \tag{2.71}$$

MP analysis in two parallel plates (see Fig.(2.6)), which is a typical example of a *two-sided MP*, has been studied by different experts. Let's assume that an electron e^- starts from the inner conductor with initial phase φ_0 and moves toward the outer conductor (in y direction) via the RF field. The homogeneous perpendicular electric field distribution across the gap is assumed to be $E = E_0 \sin(\omega_g t + \varphi_0)\hat{y}$, where ω_g is the angular frequency, t is the time and $E_0 = \frac{V_g}{d}$. V_g is the RF voltage across the gap and the gap width d is given by $d = D_{out} - D_{in}$, where D_{out} is the outer conductor diameter and D_{in} is the inner conductor diameter. Then, based on the two conditions, multiplication of the number of electrons takes place by impacting the structure's wall repeatedly. First, the trajectory of the secondary electrons should fulfill specific resonance conditions in case of two-sided MP. The order of multipactor can be defined as the number of RF periods taken for the electrons to transit from the

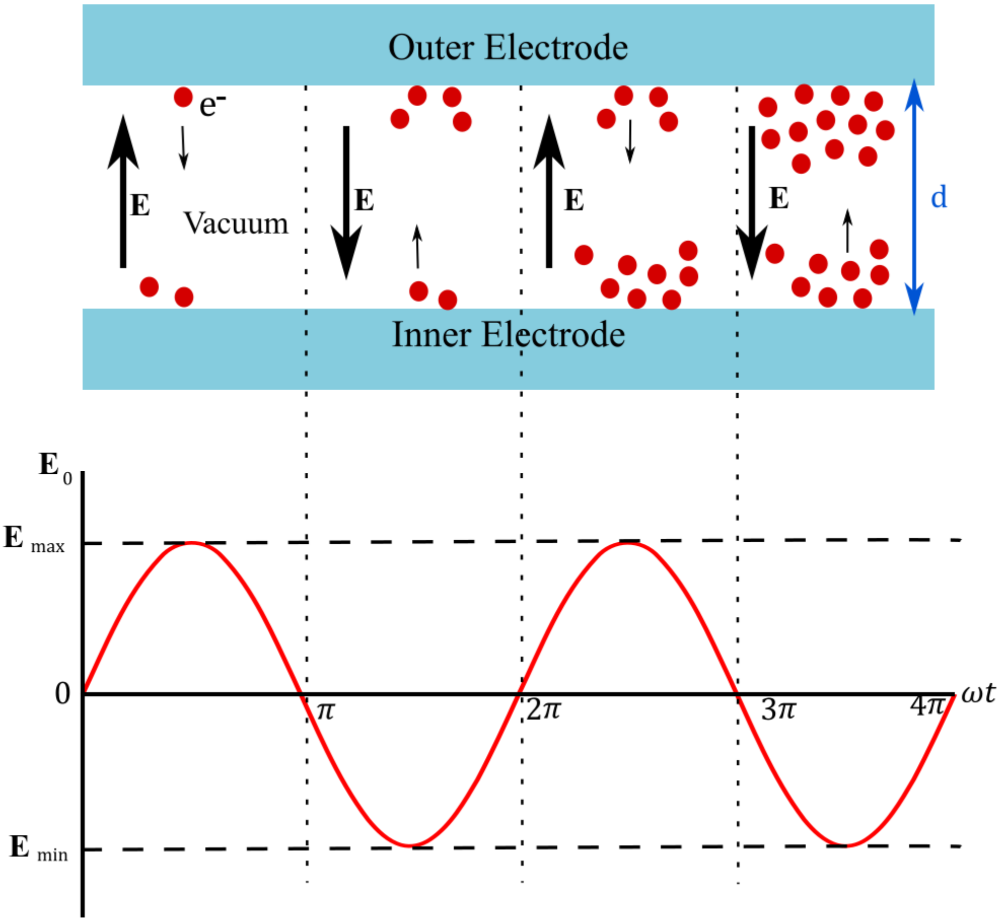

Figure 2.6: A common example of motion of electrons in a normal RF electric field between two plane surfaces.

initial point until they hit the wall of the structure. In this case the transit time of the electrons should be an odd integer number $(2n-1)$ of half RF periods [56],[148], [63], [96], [120], where n is the order of MP. This condition is commonly described by the frequency, f, the gap width, d and the RF voltage, V_g. As presented in [154], the two-sided MP can take place in the two parallel plates in the range of

$$V_{g\ min} = \frac{m(2\pi f)^2 d^2}{e} \frac{1}{\sqrt{4+(2n+1)^2\pi^2}}, \qquad n = 1, 2, 3, ..., \tag{2.72}$$

and

$$V_{g\ max} = \frac{m(2\pi f)^2 d^2}{2e}, \tag{2.73}$$

where $V_{g\ min}$ and $V_{g\ max}$ denote the minimum and maximum voltage.

As illustrated in Fig.(2.6), an electron escapes the wall of the structure at the maximum electric field $\mathbf{E}_{max}$ and hits the opposite surface at the maximum field in the reverse direction. In the two parallel plate case, the electric field limit beyond which MP does not occur is

$$\mathbf{E}_{g\ max} = \frac{V_{g\ max}}{d} = \frac{m(2\pi f)^2 d}{2e}. \tag{2.74}$$

The resonant condition may not be satisfied at a higher field as the transit times are too short.

The first condition noted above must coincide with an SEY coefficient, δ, of the surface material larger than unity for multipacting to occur [42]. This value ($\delta > 1$) is determined by two parameters, namely first crossover energy, U_{c1}, and second crossover energy, U_{c2}, which are material dependent. This condition will be discussed shortly in Sec. 2.3.

A *two-sided* cavity MP is another instance of a *two-sided* MP and will be discussed briefly. The trajectories of secondaries in the cavity is desplayed in Fig. (2.7) a. This process is represented by a very simplified equivalent circuit model [62], as shown in Fig. (2.7) b. The RF cavity, which corresponds to a resonance circuit, is modeled by a lumped **RLC** circuit and an ideal source current, which provides an accelerating voltage or the gap voltage V_g of the circuit. The ideal current source I_d is assumed to be $I_{d0} sin(\omega_g t + \varphi_0)$. The shunt impedance, $\mathbf{R}$, relates the accelerating voltage produced in the cavity to the power dissipation in the cavity walls, $\frac{V_g^2}{2P_{diss}}$. The accelerating voltage is regarded as the line integral of the electric field along the traversing path of a particle, $V_g = \int \mathbf{E}\mathbf{e}^{\mathbf{i}\omega\mathbf{z}}\mathbf{dz}$. The energy stored in the magnetic and electric field is represented by $\mathbf{L}$ and $\mathbf{C}$, respectively. The width of d separates the two plates that describe MP current in the cavity. The induced MP current I_m due to the motion of the electrons in the two plates is attached to the **RLC** circuit of the cavity. Assuming a single electron sheet with a charge density σ (in C/m^2) is positioned at x and accelerates with the velocity v, MP current becomes

$$I_m(t) = -\sigma \frac{d}{dt} x(t). \tag{2.75}$$

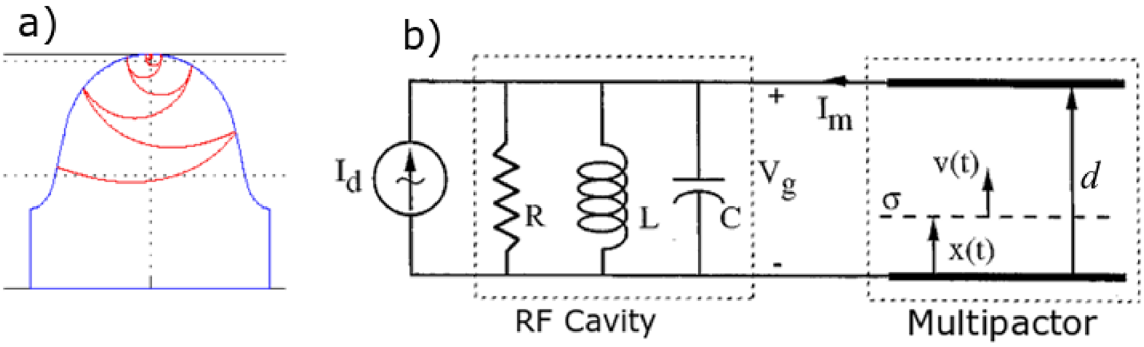

Figure 2.7: a) A trajectory of a two-sided multipactor in the cavity due to the symmetry; b) a simplified equivalent circuit diagram of the multipacting discharge in the RF cavity represented by planar structure, taken from [62] with permission. The two planes are separated by d, and a single electron sheet is placed at the position of x. The electron will be accelerated with the velocity v based on force law between the plates. As a result, the secondary electrons can be produced and MP current, I_m may occur. x and v are a function of time t.

Further formulation of *two-sided MP* established by Padamsee [96] is presented in Appendix A.

The other type of MP is a *two-point MP*. This kind of MP also occurs near the cavity's equator, as shown in Fig.(2.8) [122]. However, in most cases, a two-point MP does not affect the cavity performance since it is eliminated after processing [96]. Some studies yet indicate that the problem persists in the equator region [173], [121]. Unlike the parallel plates MP, the magnetic field has a higher effect on the motion of electrons in this region of the cavity rather than the electric field. Therefore, according to Shemelin [121], the occurrence of MP near the equator is determined by the magnetic parameter M, which is defined by $e\mathbf{B}_0/m\omega$, and the geometrical parameter p given by $(d\mathbf{E}_n/dx)/\omega\mathbf{B}_0$. p describes the curvature near the equator. $\mathbf{B}_0$ represents the magnetic field at the equator and $\mathbf{E}_n$ is the normal electric field at MP site. Moreover, the electric field level, $\mathbf{E}_{MP}$, of which MP near the equator is most likely to happen, can be calculated by

$$\mathbf{E}_{MP} = \frac{\mathbf{B}_0(1+\epsilon)}{\mathbf{B}_{pk}/\mathbf{E}_{acc}}, \tag{2.76}$$

where $\mathbf{B}_{pk}/\mathbf{E}_{acc}$ is the ratio of the peak magnetic field and accelerating field. This ratio is one of the figures of merit for the development of SRF cavities. ϵ stands for the value of the deviation between the peak field and the field at the equator. The detailed derivation and analysis can be found in [121].

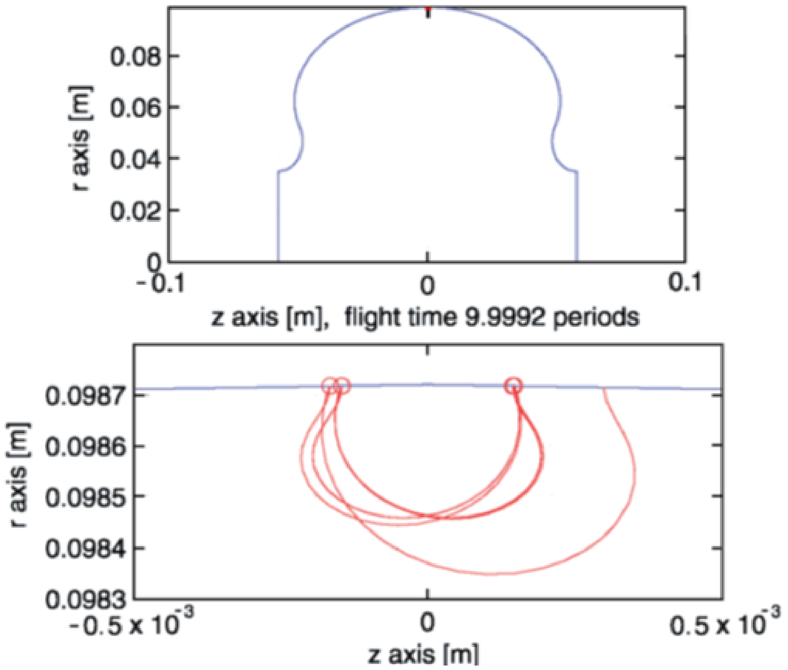

Figure 2.8: Motion of the electrons in a normal RF electric field near to the cavity equator, taken from [121] with permission.

2.5.1 Secondary Electron Emission Mechanism

There are a number of experimental studies as well as theoretical treatments of the secondary electron emission process, including [11], [19], [149], [8], [42]. The emission of electrons from the materials takes place as the electrons with certain energies strike the wall materials. The emission depends not only on the energy and the angle of primary electrons but also on the properties of the surface material. Furthermore, the number of emitted secondaries is determined by surface conditions, e.g., surface contamination. This emission of secondaries may lead to a significant impact on the performance of the RF system. As noted before, the coefficient of the emission is usually known as the secondary electron yield (SEY) coefficient, δ, which can be defined as the ratio of the secondary emission current (incident), I_s, to the primary electron current (emitted), I_0:

$$\delta = I_s/I_0. \tag{2.77}$$

As illustrated in fig.(2.9), the model distinguishes three different ways of generating secondary electrons [42]: elastic reflection (backscattered electrons), true secondary electrons, and inelastic reflection (re-diffused electrons). The corresponding electron currents are denoted as I_{bs}, I_{ts} and I_{rd}, respectively. When the incident electrons (I_0 or e_0) strike the surface, certain electrons are elastically reflected back, which

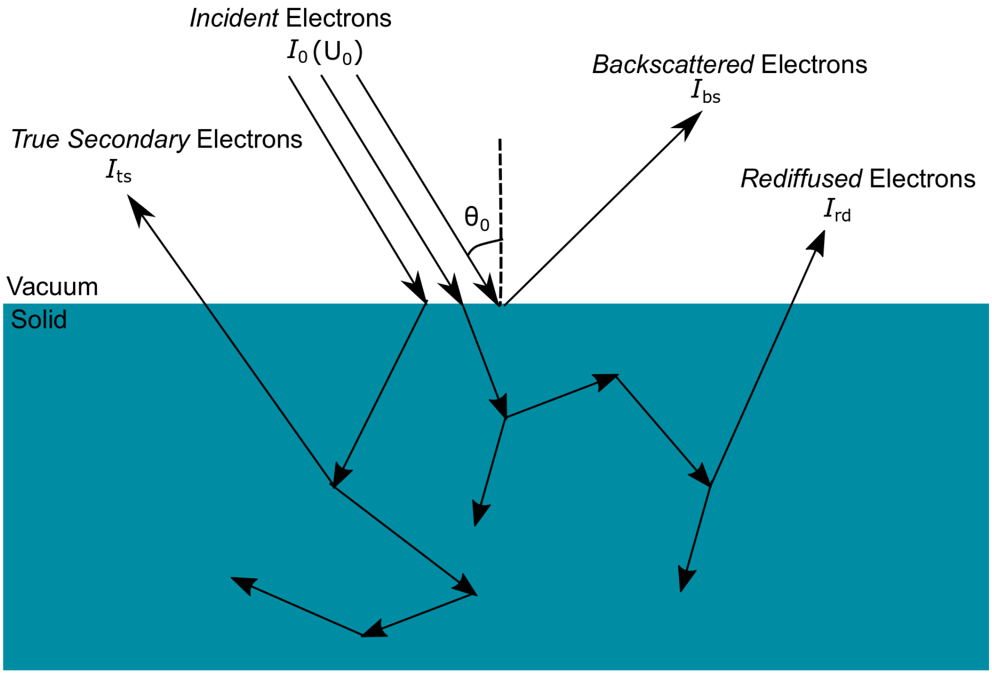

Figure 2.9: A sketch of electron-surface (electron-material) interaction; and the dependency of secondary electrons emission process on incident energy, U_0, and angle, θ_0.

are called *backscattered* electrons, while the remainder penetrate into the material. Some electrons interact in a more complicated way with the material and produce more electrons which are called *true* secondary electrons. The remaining electrons are scattered back out of the material and are called $rediffused$ electrons. The SEY is therefore the contribution of all the three secondaries (see example of Furman model for copper (Cu) Fig.(2.10)), then Eq. (2.77) can be written as

$$\delta = (I_{bs} + I_{ts} + I_{rd})/I_0. \tag{2.78}$$

As mentioned earlier, SEY is a function of the impact energy U_0 of the incident electron and its incident angle θ_0:

$$\delta(U_0, \theta_0) = \delta_{ts}(U_0, \theta_0) + \delta_{bs}(U_0, \theta_0) + \delta_{rd}(U_0, \theta_0). \tag{2.79}$$

These secondaries are distinguished based on their energy distribution (see e.g. [73], [19], [42]). The electrons with low energies contribute more to the generation of secondary electrons than the electrons with higher energies. Therefore, in general MP is a low gradients phenomenon compared to the acceleration gradient utilized in the cavity. However, in rare cases MP can also happen at high gradients in the RF components.

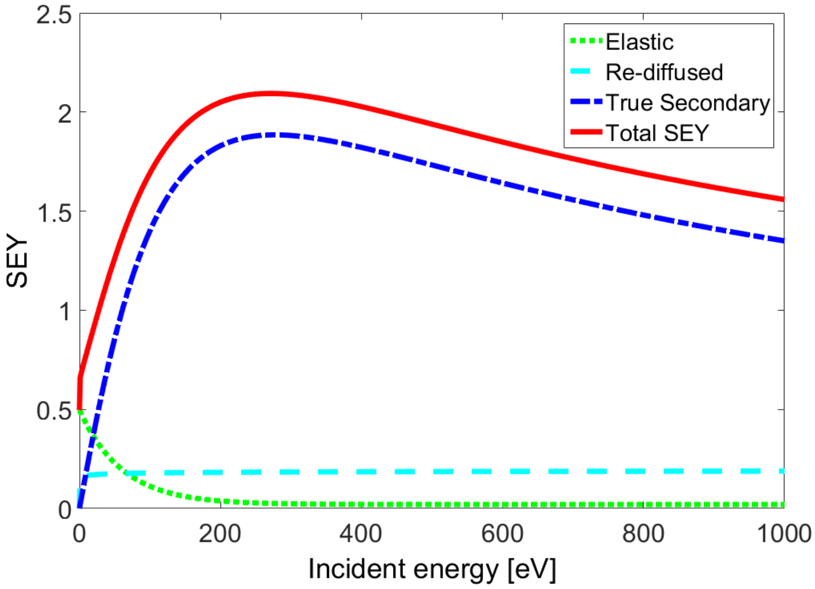

Figure 2.10: Furman's three types of secondary emission models for copper as a function of incident energy at zero incident angle.

The secondary emission process is commonly described by SEY curves, which are characterized by the first crossover of energy, U_{c1}, the second crossover of energy, U_{c2}, where δ crosses the line with $\delta = 1$, and a peak SEY $\hat{\delta}$ at a certain incident energy $\hat{U}$. Figure 2.11 shows the total δ (Eq. (2.79)) as a function of primary energies U_i. The shape of this curve is determined by the penetration depth of the incident electron. The latter measures how deep the electrons can penetrate the material, after which the generation of the secondary electrons is triggered. The number of secondaries is proportional to the energy of the primaries at low energy, $U_0 < U_{c1}$. In this case, a larger part of the secondaries escapes the wall material as the primary electrons strike the wall with "short penetration depth". For that reason, only a small number of secondaries are generated, which results in the SEY value below one. In the range of the two crossover energies, i.e. $U_{c1} < U_0 < U_{c2}$, more secondaries are produced at greater depth. Thus within the range of these impact energies, the number of resonant electrons might multiply exponentially. The highest generation of secondaries is also expected at the peak SEY, $\hat{\delta}$ with the corresponding energy, $\hat{U}$, for perpendicular incidence. Eventually, for higher energies, namely $U_0 > U_{c2}$, the primary electrons penetrate extensively deep into the surface and interact with its material. Consequently, many secondaries are not able to escape the surface as they loose their energies.

The emission of secondaries can be described by three different emission models in the CST PS: an advanced probabilistic emission model developed by Furman and

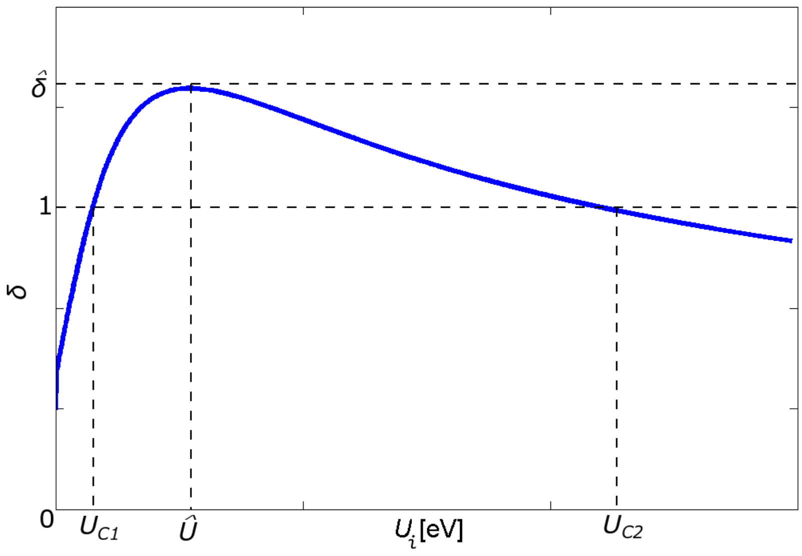

Figure 2.11: An example of the SEY curve as a function of impact energy. At $\delta = 1$, there are two important parameters, namely the first and the second crossover energy, U_{c1} and U_{c2}, respectively. Electron multiplication takes place between U_{c1} and U_{c2}. The SEY reaches its peak, $\hat{\delta}$, at the impact energy, $\hat{U}$.

Pivi [42], an emission model developed by Vaughan [149] and an *imported emission model*. The two former models are often used to simulate multipactor in accelerating cavities and other RF structures. A short comparison of these models, including some multipactor simulation results based on the two models, are presented in [106].

In the case of *imported emission model*, the measurement data is employed. Once the measured δ data is loaded into the simulated structure, the setting of the parameter of the SEY model is straightforward. *Imported emission model* also supports using a graphics processing unit (GPU), which provides an excellent runtime reduction for a simulation. The general formulation of the imported emission model is included in Appendix D of this thesis.

Vaughan's SEY model [148] is also computationally simple as only a small number of parameters are needed to be configured. Similar to the *imported emission model* only the true secondary of the SEY curve is modeled. Moreover, the emission process is not specified, e.g., a zero-energy approximation for the emitted secondary electrons. In Vaughan's model, the contribution of δ is not considered at low energy, namely below 12.5 eV, i.e. $U \to 0$ and $\delta \to 0$.

The SEY model of Furman [42] is the most accurate but sophisticated model with 45 parameters. The model comprises all the three types of emissions which are noted above. Most importantly, the emission process is specified stochastically, particularly, the emission energy spectrum of the secondary electron $d\delta/dU$ and angular distribution. Additionally, contrary to Vaughan's SEY model, the SEY contribution at low energy, $U \rightarrow 0$ and $\delta \rightarrow \neq 0$, is well analyzed. The model is also in a very good agreement with the measurement data. Therefore, it provides a reliable and accurate prediction of MP. However, as the model is based on a stochastic scattering process, a Monte Carlo simulation approach is required to compute the emission of secondaries, which results in high computer memory and time consumption. Moreover, both Vaughan's and Furman's models do not yet support GPU based PIC simulations. The latter model is briefly discussed below as it was employed in the computational results presented in the following chapters.

2.5.2 Secondary Electron Emission Model of Furman

The Furman model considers each *event*, where a single electron hits the wall, and describes the emission process of secondaries *event-by-event*. When the electron collides with the wall with kinetic (impact) energy U_0 and incident angle θ_0, n secondaries will be generated with a probability $P_n(U_0, \theta_0)$, $n = 1, ..., \infty$. All the information from the initial state, where the electron initially emitted at a specified energy U_0 and angle θ_0, and final state, where the electrons emitted after the impact with kinetic energies $U_1, U_2, ...U_n$ and angles $\Omega_1 = (\theta_1,\phi_1)$, $\Omega_2 = (\theta_2,\phi_2)$,...$\Omega_n = (\theta_n,\phi_n)$, of the emission process is described by *phase-space probabilities* $\mathbb{P}_n$ [42]:

$$\mathbb{P}_n = \frac{dP_n}{dU_1 d\Omega_1 dU_2 d\Omega_2 ... dU_n d\Omega_n}, \qquad 1 \leq n < \infty, \tag{2.80}$$

where θ and ϕ denote the polar and azimuthal angle, respectively. The condition to be generated after the impact for δ_{bs} and δ_{rd} is only in events $n = 1$, while for δ_{ts} is in events $n \geq 1$. Otherwise the incident electron is absorbed by the material.

The measurement data of δ and $d\delta/dU$ are the main input parameters of Furman's SEY model to describe a set of probability functions of emitted secondaries. The mathematical representation of $d\delta/dU$ is given by

$$\frac{d\delta}{dU} = \sum_{n=1}^{\infty} \int (dU)_n (d\Omega)_n \mathbb{P}_n \sum_{k=1}^{n} \delta(U_k - U). \tag{2.81}$$

The term $\sum_{k=1}^{n} \delta(U_k - U)$ of Eq.(2.81) confirms that the emitted energy of the secondaries should be $\geq U$, for electrons to be counted.

Figure (2.12) depicts an example of the energy distribution curve (energy spectrum) of secondary electrons for Cu. There is no clear-cut distinction between the three types of emitted electrons in this curve. The energies below 27 eV, where the limit is arbitrary, represent *true* secondary electron region, while between 27 eV and 95 eV is $rediffused$ emission region. The *backscattered* emission region lays above 95 eV. The value of δ_{ts}, δ_{rd} and δ_{bs} of δ can be obtained by integrating over the range $[U_1, U_2]$ for each. One important feature of Furman's model is taking into account the electrons with low energies as the contribution of such electrons is considerable in the yield.

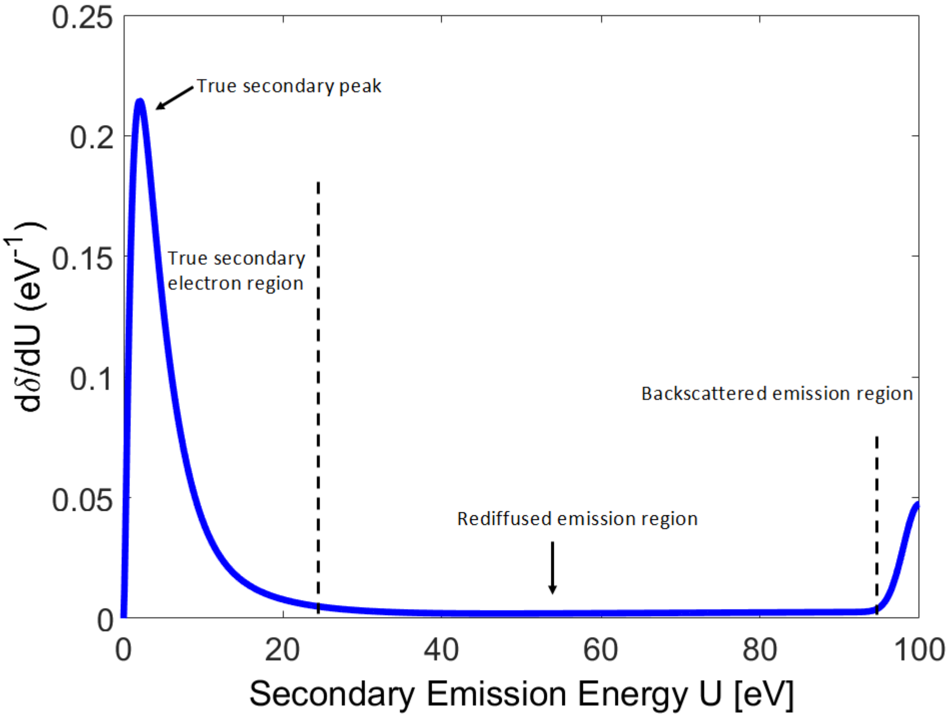

Figure 2.12: Energy spectrum of electrons emitted for Cu at incident energy $U_0 = 100$ eV and angle 0° as implemented in CST PS.

The probability $P_{n,ts}$ for emitting n true secondary electrons is assumed to be a binomial distribution:

$$P_{n,ts} = \binom{M}{n} p^n (1-p)^{M-n} \ , \tag{2.82}$$

where M is the maximum number of secondary electrons. The emission process of these electrons is characterized by the energy probability density function (PDF), then as Furman formulated the PDF of the *true* secondaries reads:

$$f_{n,ts} = \theta(U) F_n U^{p_n - 1} e^{-U/\epsilon_n} \ , \tag{2.83}$$

where U is the secondary energy, F is the normalized energy spectrum to unit height and p_n and ϵ_n are fitting (adjusting) parameters, which vary for each material. The dependency of the generation of *true* secondary component on incident energy, U_0 as well as on incident angle with respect to the surface normal, θ_0, is given by

$$\delta_{ts}(U_0, \theta_0) = \hat{\delta} D(U_0/\hat{U}), \tag{2.84}$$

where $\hat{\delta}$ is a peak value of SEY that occurs at energy $\hat{U}$. $D(x)$ is a weighting function for δ_{ts} and formulated as $D(x) = \frac{sx}{s-1+x^s}$, that provides a good fit to the measurement data. s is again an adjustable or fit parameter of the yield (e.g. for Cu $s = 1.54$). Furman has also presented an alternative formulation for δ_{ts} using some other weighting functions (see Appendix F in [42]). The peak value of *true* SEY δ_{ts} as a function of incident angle θ_0 is defined as:

$$\hat{\delta}(\theta_0) = \hat{\delta}_{ts}[1 + t_1(1 - cos^{t_2}\theta_0)] \ , \tag{2.85}$$

and the model is assumed to have its peak at the normal incident angle of primary electrons and at the energy $\hat{E}$:

$$\hat{U}(\theta_0) = \hat{U}_{ts}[1 + t_3(1 - cos^{t_4}\theta_0)] \ , \tag{2.86}$$

where t_1, t_2, t_3 and t_4 are material parameters, e.g. their values for Cu are 0.66, 0.8, 0.7 and 1, respectively.

In the case of *backscattered* component, the electrons are assumed to be elastically reflected back from the impact point with the same energy as incident. Its PDF, which has a Gaussian distribution, is approximated by

$$f_{1,bs} = \theta(U)\theta(U_0 - U)\delta_{bs}(U_0, \theta_0)\frac{2\exp(-(U - U_0)^2/2\sigma_{bs}^2)}{\sqrt{2\pi}\sigma_{bs}erf(U_0/\sqrt{2}\sigma_{bs})}, \tag{2.87}$$

and $\delta_{bs}(U_0, \theta_0)$ will be obtained by integrating Eq.(2.87) over energy U:

$$\delta_{bs}(U_0, \theta_0) = \delta_{bs}(U_0, 0)[1 + e_1(1 - cos^{e_2}\theta_0)]. \tag{2.88}$$

If incident angle assumed to be normal, i.e. $\theta_0 = 0$, equation (2.88) becomes:

$$\delta_{bs}(U_0, 0) = P_{1,bs}(\infty) + [\hat{P}_{1,bs}]\exp(-\frac{|U_0 - \hat{U}_{bs}|^p}{p^{Wp}}), \tag{2.89}$$

with the assumption of $\hat{P}_{1,bs} > P_{1,bs}(\infty)$, where the function reaches its peak at $U_0 = \hat{U}_{bs}$. For instance for Cu, $\hat{P}_{1,bs} = 0.496$ and $P_{1,bs}(\infty) = 0.02$.

For *rediffused* electrons, the PDF is assumed to have an exponential distribution and the function reads:

$$f_{1,rd} = \theta(U)\theta(U_0 - U)\delta_{rd}(U_0, \theta_0)\frac{(q + 1)U^q}{U_0^{q+1}} \ . \tag{2.90}$$

The yield for *rediffused* electrons is given as:

$$\delta_{rd}(U_0, \theta_0) = \delta_{rd}(U_0, 0)[1 + r_1(1 - cos^{r_2}\theta_0)], \tag{2.91}$$

and if $\theta_0 = 0$ (normal incidence), Eq. 2.91 will be modified as:

$$\delta_{rd}(U_0, 0) = P_{1,rd}(\infty)[1 - \exp(-(U_0/U_{rd})^r)]. \tag{2.92}$$

Except the energy, U, and the angle θ, all parameters mentioned in the formulation of energy probability density function and the yield (from Eq.(2.87) to Eq.(2.92)) are fitting parameters, which are material dependant. The detailed derivation and analysis of the Furman model is given in [42].

3 Numerical Study of Multipactor

Multipactor discharge has been recently observed in various SRF structures, for instance [20],[166],[75],[98],[103]. Similarly, the discharge exists in the ELBE's SRF gun [6] as noted before. The occurrence of MP limits the performance of the gun. Figure 3.1 shows the schematic diagram of the ELBE'S SRF gun I. MP was predicted in the gun in early design stages. The results from simulations and measurements at HZDR indicated multipactor in the gap between the cathode stem and the cavity [6].

Here we describe a numerical study of multipactor discharge that allows us to analyze MP in RF structures by solving the non-relativistic equation of motion of electrons in time-harmonic RF fields. The study should also consider the SEY coefficients of the structure's materials, as mentioned in chapter two. This makes the computation more challenging. The numerical simulations were mainly carried out using the 3D simulation software CST STUDIO SUITE® [3]. The results will be compared to experimental data, as well as to the results from 2D*Multipac* code [175]. Our theoretical solution (see Appendix B) and initial numerical computations confirmed the susceptibility of MP in the vicinity of the cathode. Therefore, to better understand the MP behavior and identify the range of the electric field in which it occurs, intensive simulation studies with realistic assumptions have been performed [139],[142]. Furthermore, various MP suppression techniques have been studied. Part of our results are published elsewhere [140],[141],[142].

3.1 Simulations using CST Studio

Generally, there are three steps for MP simulations: The first step is the geometry definition and the calculation of the EM field for the given geometry. The second step is calculating and tracking the motion of a large number of particles in the EM field distribution along with the structure. Finally, the third step is identifying a possible MP behavior in the collection of particle tracking data. All three steps can be done using CST STUDIO SUITE® [3]. Other features of this software worth mentioning include the availability of numerous data in the material library, an advanced probabilistic emission model, and adequate post-processing tools of CST PARTICLE STUDIO® (CST PS). Therefore, the Particle-in-Cell (PIC) solver of CST PS was chosen for these numerical studies on MP. PIC solver of CST PS allows us to compute and analyze multipactor discharge in fully three-dimensional RF structures. There are also recent MP studies on coaxial waveguides [107], low beta spoke cavities [109],[13] and quarter-wave SRF photoinjector [98] using CST

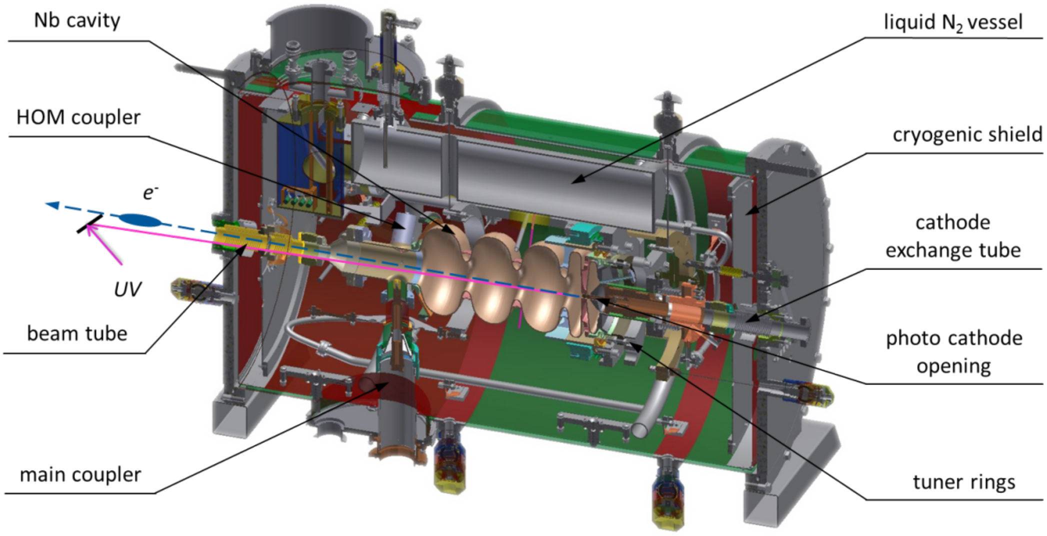

Figure 3.1: The schematic diagram of the ELBE'S SRF gun I. Reprinted from [5], with permission from Elsevier

PS that provide detailed technical procedures.

The EM field simulation software package CST MICROWAVE STUDIO® (CST MWS) was employed to compute the operating frequency and the corresponding EM field pattern within the SRF gun. A complete CST MWS model of the ELBE's SRF gun is illustrated in Fig 3.2 (a). The simulated structure was initially designed at ELBE and imported into CST MWS. The design of this gun was discussed in detail in [5],[4]. In different stages of the numerical studies, different simplifications of the complete model of the gun were regarded. Three different models are referred to in this thesis:

- A simplified model comprised of a half-cell cavity, a cathode unit and a chock filter (Model A)

- A coaxial structure plus half-cell cavity (Model B)

- And just the coaxial part of the SRF gun (Model C)

The first step to study and analyse the MP behavior was to compute the EM field, and MP within Model A. The obtained numerical results allow us to evaluate and analyze the occurrence of MP in the cathode unit of the gun. Moreover, the range of the electric fields in which MP occurs is identified. A detailed description and results are presented below.

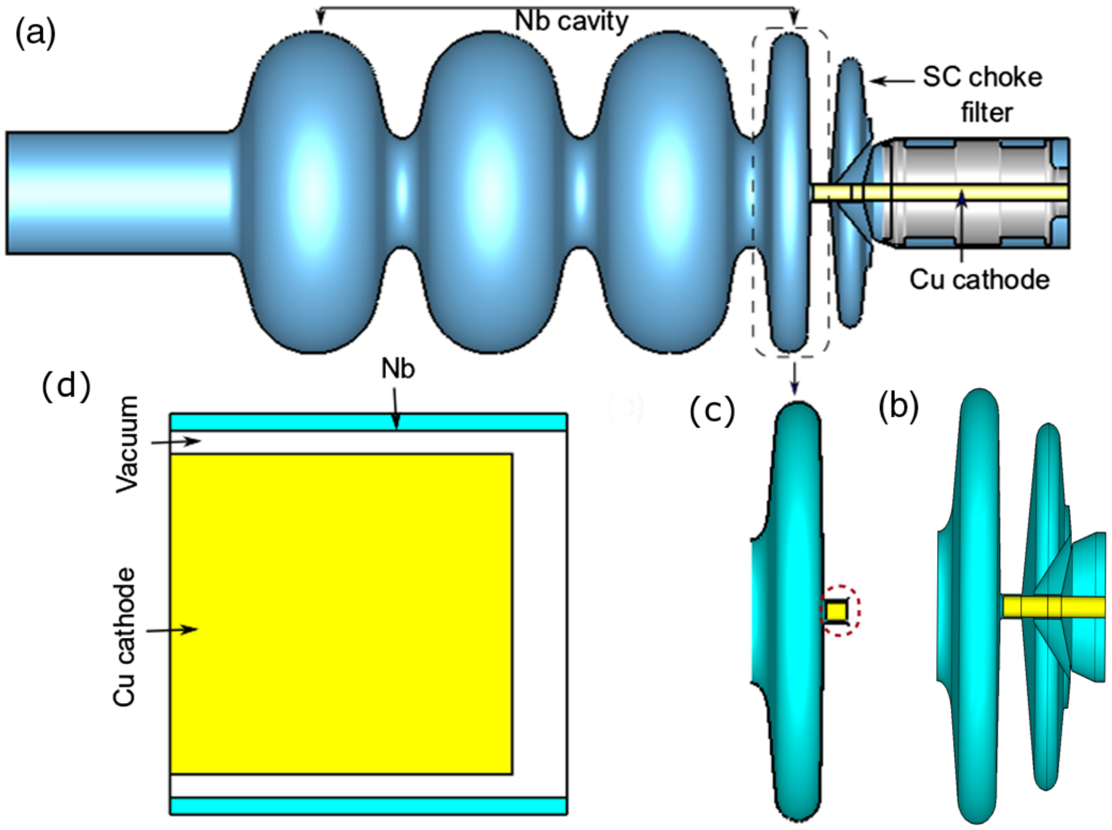

Figure 3.2: (a) A complete CST MWS model of the SRF gun that comprises a 1.3 GHz 3.5 cells TESLA-like Nb cavity, a NC photocathode, and a SC choke filter; (b) Model A. This model consists of a half-cell cavity, a cathode unit and a chock filter; (c) The coaxial structure (marked in red) plus half-cell cavity structure (Model B); (d) a simplified model covering just the coaxial part (Model C) that is most relevant with respect to MP. The coaxial structure of the cathode region. The structure consists of Cu stem (in yellow) and Nb pipe (in blue green).

3.1.1 Computation of Electromagnetic Field and Multipactor Discharge within Model A

A complete CST model of the SRF gun comprises a 1.3 GHz 3.5 cells TESLA-like niobium cavity, a normal conducting (NC) photo-cathode, and a superconducting (SC) choke filter. The NC photo-cathode is inserted at the circular end of the niobium half-cell cavity with a 1 mm vacuum gap for thermal and electrical insulation. The photo-cathode is surrounded by the choke filter to prevent leakage of the RF field from the cavity. Different eigenmodes, such as TM-Monopole, TM-Dipole, TM-Quadrapole, TM-Sextupole, TE mode, and hybrid TE and TM, are computed inside the structure. All the necessary data of the model is published in [4]. The fundamental mode of the RF cavity of the gun used for beam acceleration is TM_{010} (Monopole) at a frequency of 1.3 GHz.

To decrease the number of required mesh cells and reduce simulation time, the CST's complete model was simplified to Model A as noted above. Model A consists of a Nb half-cell cavity, a Cu cathode and a Nb choke filter as illustrated in Fig. 3.3 (b). The Eigenmode solver of CST MWS was utilized to compute EM fields of the eigenmodes within Model A. Appropriate boundary conditions and sufficient mesh resolution of the mathematical model are significant to obtain an accurate result. The perfect electric boundary at the surface and perfect magnetic boundary conditions at the end of the structure were specified. Moreover, the partial volume of Model A with proper BC was simulated to enhance the computing efficiency, as the model is cylindrically symmetry. Two symmetry planes modeled by magnetic BC were applied, as shown in Fig. 3.3 b, which reduces the computational time by a factor of four as only 1/4 of the simulated volume needs to be calculated.

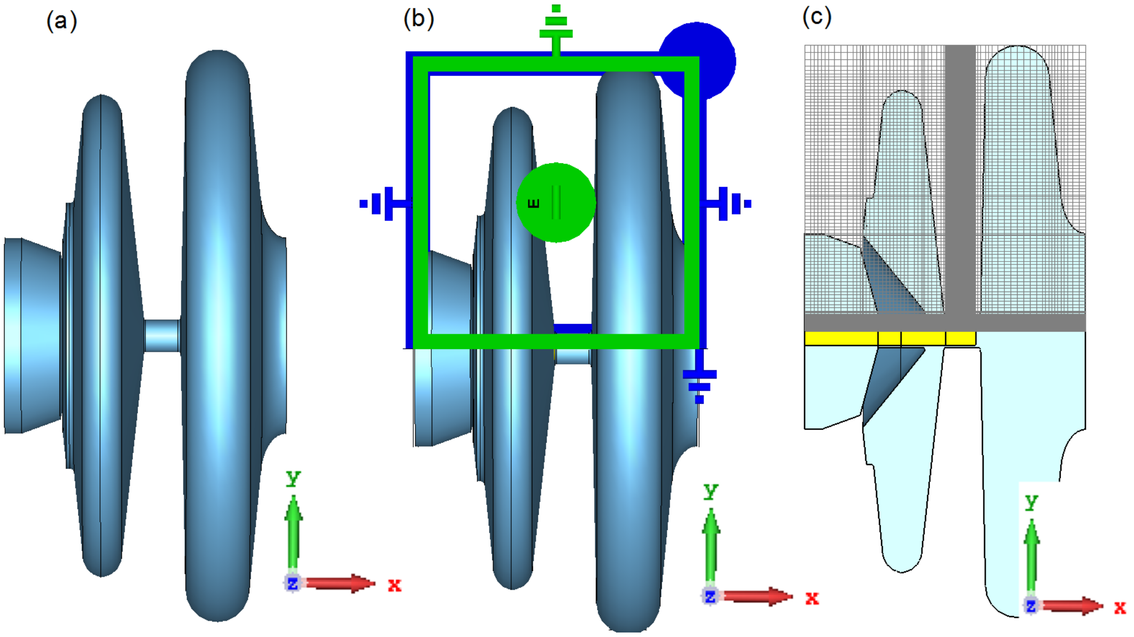

Figure 3.3: (a): Model A; (b): BC conditions of this model; (c): A hexahederal mesh representation of Model A.

Among several simulation parameters which may affect the computational results of MP, suitable mesh size is usually critical for reliable simulation results. Therefore, a certain effort was made to optimize the meshing of each simulated model. In principle, finer mesh-sizes produce more accurate numerical results. However, a finer mesh requires larger computational resources. For that reason, a *mesh refinement study* is required to make a good compromise between accuracy and computational demands. For the field calculation, the *mesh refinement study* for the entire geometry was conducted, please see Appendix E. Moreover, the growth rate of multipactor avalanche depends on the local amplitude of the RF electric field. Therefore, a finer mesh was applied to the region of interest, i.e., the cathode vicinity, using the *local mesh refinement* to obtain a local field map with higher precision. The *local mesh refinement* approach is one of the features of CST to provide a more accurate representation of the region of interest. As CST PS only supports HEX meshes with Perfect Boundary Approximation® (PBA) technique [71] for MP simulations, such meshing was also chosen for EM field computation as illustrated in Fig. 3.3 (c). The PBA technique is an efficient approach to represent curved geometry and very large computational model accurately even on rather coarse HEX meshes [71],[87].

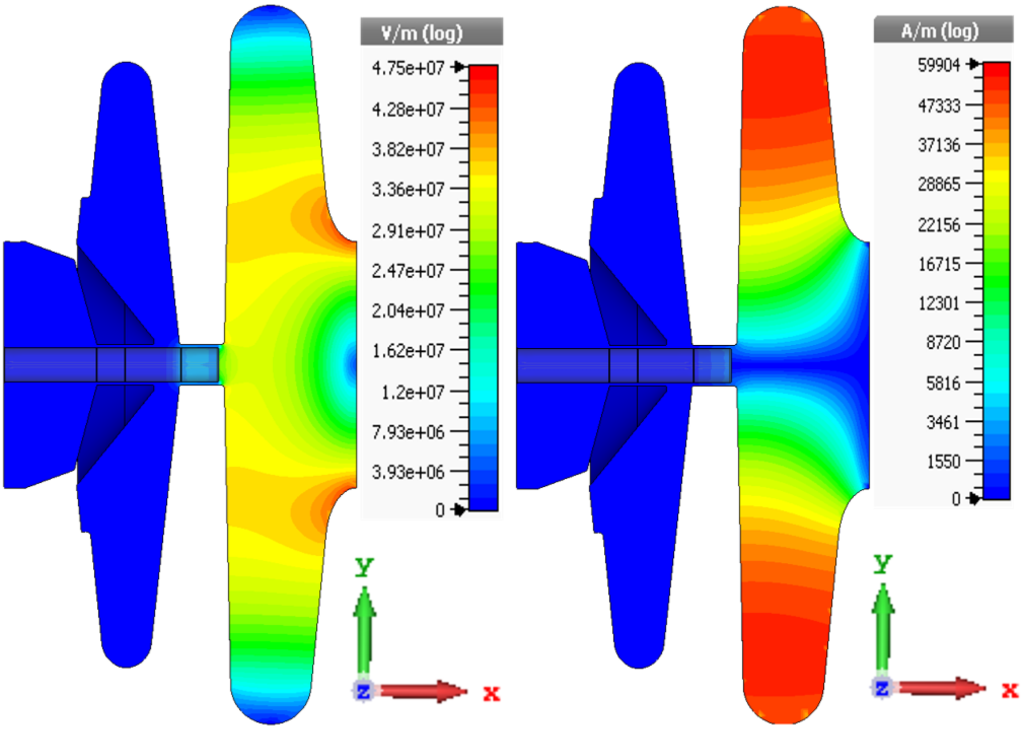

Figure 3.4: Distribution of electric and magnetic fields for Model A. Left: the electric magnitude of the TM_{010} mode on z-cut plane at 0 deg phase; Right: magnetic field distribution of the TM_{010} mode on z-cut plane at 90 deg phase.

The distribution of electric and magnetic fields of the TM_{010} mode within Model A, shown in Fig. 3.4, had values defined for $N_x = 115$, $N_y = 77$, $N_z = 76$ nodes. The corresponding total number of mesh cells is 649,800. The computed resonant frequency is 1.298 GHz. The peak electric field on-axis is 18.3 MV/m, which is normalized by 1 J in the eigenmode solver, whereas the highest field on the surface in the half-cell cavity is about 47.5 MV/m. The calculated field was imported into the PIC solver of CST PS for MP simulation.

In PIC solver, the imported MWS model presented in Fig. 3.2 (a) was constructed from a "vacuum" body and PEC material was considered as the background material. However, the background material of PEC is not recognized in the PIC solver. Thus the model was modified in CST PS by creating a cavity wall with some thickness to define a different material property on the wall. CST material library provides a number of materials with predefined secondary emission properties based on three emission models, namely, an advanced probabilistic emission model developed by Furman and Pivi [42], an emission model developed by Vaughan [149] and an *imported emission model.* In simulations, the material Cu for the cathode (inner surface) and Nb (300°C Bakeout) for the outer surface was used for the RF surface. Figure 3.5 shows the three kinds of emitted electrons and the contribution of all to the total SEY curve of Furman's model for Cu and Nb, which is a function of the impact energy (U_i) of the incident electron and its incident angle (θ_0). The peak SEY, $\hat{\delta}$, of Cu is 2.1 at 250 eV of corresponding impact energy, $\hat{U}$. Similarly, the $\hat{\delta}$ of Nb is 1.49 at 300 eV of $\hat{U}$, for perpendicular incidence.

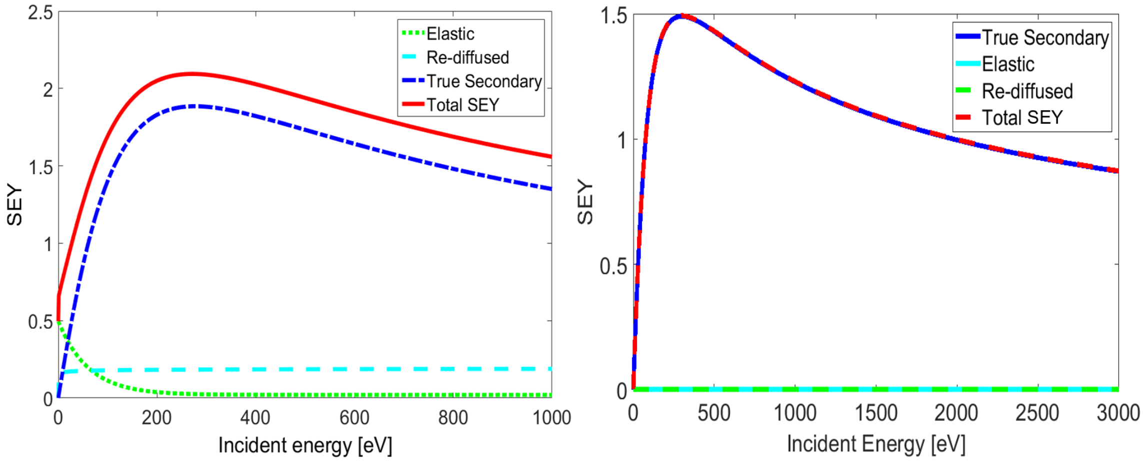

Figure 3.5: Furman's Models of SEY curves. Left: SEY curves for Cu as a function of the impact energy of the incident electron; Right: SEY curves for Nb as a function of the impacting energies.

Unlike CST MWS, symmetry plains are not supported in the PIC solver as trajectories of particles might not be symmetrical. Thus, the whole geometric domain was discretized with a mesh of around 2.5 million mesh cells. Then the EM fields were internally imported, which is illustrated in Fig.3.4. The amplitude of the on-axis accelerating field was scaled in PIC solver as the energy of field was normalized to 1 J in CST MWS. The adjustment or calculation of the scaling factor was based on the actual accelerating field gradient of the cavity.

Having imported EM fields, initial electrons (seed electrons) are required to initiate the multipactor discharge. Thus initial electrons, including initial energy of electron, electron emission phases and initial position are assigned for the calculation. The initial electrons can be assumed using various types of emission models in CST PS. Since the susceptibility region was already known, a particle source was assigned to a single point on the cathode using the Gaussian model. This type of initial source is denoted as "particle point source" in CST PS. The parameters of this particle source used in our simulations are displayed in Table 3.1.

Table 3.1: Set up of the Particle Source

Source type	Point
Particle type	Electron
Emission model	Gaussian
Bunch	1
Bunch charge (C)	$1.0e^{-18}$
Sigma (ns)	5.0
Cutoff (ns)	0.1952
Offset (ns)	0.1952
Emission type	Energy
Kinetic energy (eV)	4

The *point source* assumption was reasonable since it is well known that even the appearance of a single particle at the right time can initiate MP. Nevertheless, to check for the existence of stochastic fluctuation in the results (if any), an area source covering the complete inner conductor was also considered for the simulation. Since both results agreed very well, and to save simulation time, we decided to use the particle point source throughout the following simulations. Moreover, the space charge effects were neglected in the PIC simulations as recommended in [34, 84].

The seed electrons were launched during the first period of the RF cycle. When the electrons hit the opposite wall, a number of secondaries were calculated according to Furman's emission model. The discharge process depends on the dynamics of the fields and the secondary emission properties of the material as discussed in previous chapters. Two approaches were adopted to identify and analyze MP, i.e evaluate the time evolution of the number of particles and calculate the average SEY along the average impact energy. The growth in the number of particles as a function of time within the volume of the structure is a common characteristics to indicate and verify MP. Thus, the number of particles over time was evaluated in the Model A for different levels of the electric field. Figure 3.6 shows the number of particles within 50 ns. The scaling factor was determined such that the electric field in the gap varied from 85 to 175 kV/m. This range corresponds to a cavity field in the range of 1.11 to 2.21 MV/m. Close observation of these results reveals that the increment of the number of particles within 50 ns takes place between electric field levels of 1.25 MV/m and 1.85 MV/m. That means resonant conditions for secondary emission occur at these field levels that lead to the electron avalanche. Moreover, the maximum generation of secondaries occurs at 1.55 MV/m, which is in good agreement with experimental data. The CPU time needed to complete one MP simulation within 50 ns was around 6 hours using Intel(R) Xeon(R) CPU E5 with 3.30 GHz and 256 GB.

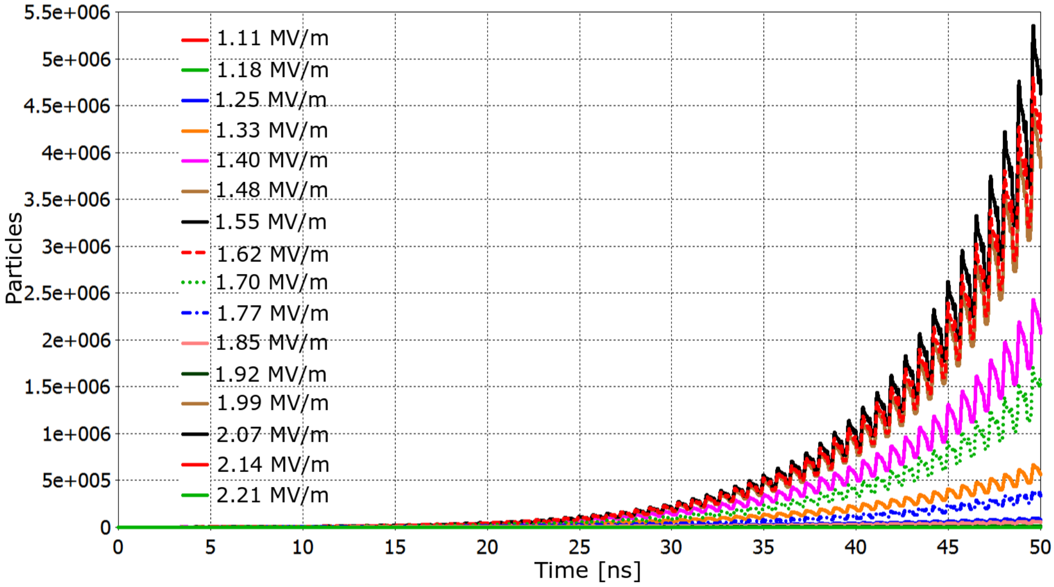

Figure 3.6: The number of particles in Model A after 50 ns for different field levels.

The development of MP in time in the cathode region at 127.7 kV/m is shown in Figs. 3.7. The corresponding maximum impact energy is 147 eV. These trajectories demonstrate the stable electron trajectories during their back and forth oscillations. Moreover, their motion between two opposite impact points and time between impacts demonstrated the type of MP, i.e. the *1st order two-sided* MP. The resonant condition of the trajectories of such kind of MP is discussed in chapter two.

For the detailed analysis of the intensity of MP at the critical field levels and to easily correspond the results with the MP threshold condition, the average SEY (δ_a) and the average impact energy (U_a) were then calculated. A field-level for a δ_a function larger than unity indicates a potential multipactor. This implies that more than one secondary is produced on average for every electron impact, which results in the rise of the number of electrons in time. The calculations were done for each separate surface from the collision and emission currents and the collision and emission powers generated by CST PS. These data enable us to calculate the δ_a [13] that is defined as the integral of the emission current divided by the integral of the collision current. The calculation was made for inner and outer surfaces separately.

Figure 3.8 illustrates the simulation result for Cu (inner cathode surface) and Nb (outer surface) with a vacuum gap width of 0.75 mm. The δ_a curve for Cu shows

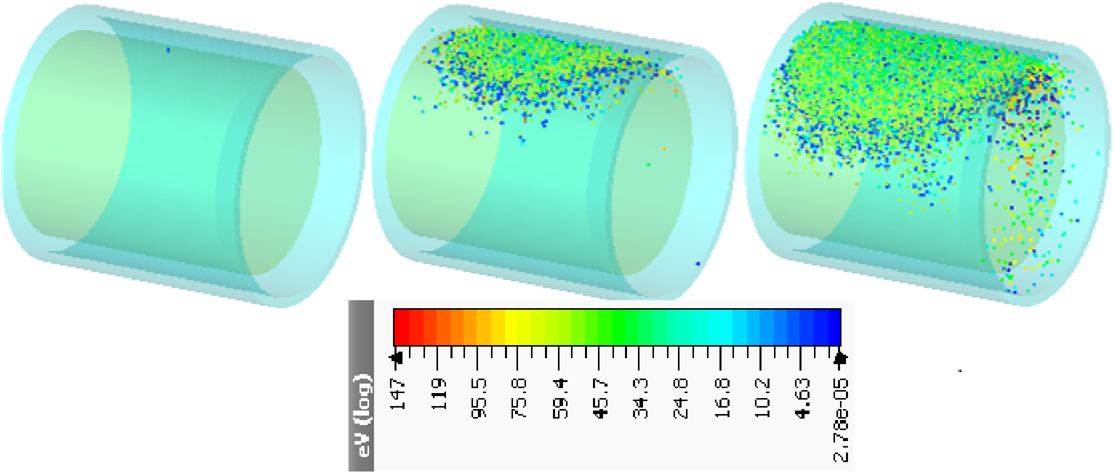

Figure 3.7: Development of MP in time in the cathode vicinity at 127.7 kV/m after 0.2 ns (left), after 13.4 ns (middle) and after 25.7 ns (right).

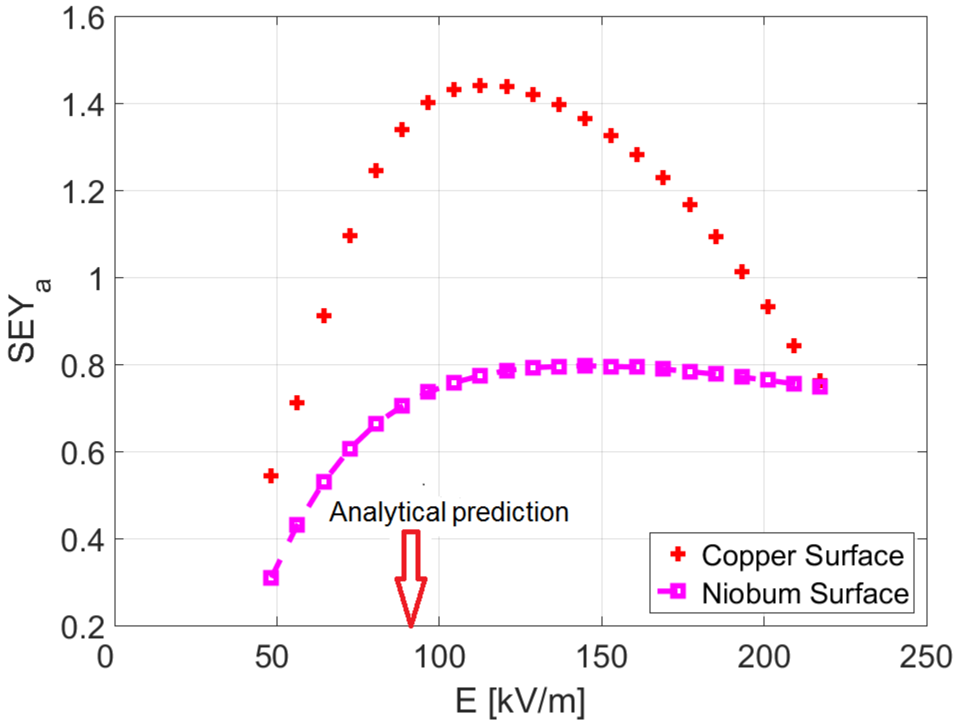

Figure 3.8: Average SEY as a function of electric field for copper and niobium surfaces. The analytical prediction of the field level causing MP is indicated by the red arrow.

that the lower limit E_{min} and the upper limit E_{max} of the electric field amplitude were 70 kV/m and 194 kV/m, respectively. The δ_a was larger than one for U_a values between 35 and 50.8 eV. The δ_a of 1.44 was produced at the gap electric field of

112.6 kV/m. Additionally, the analytical estimation of the field level and the impact energy for 1^{st} order *two-sided* MP in a vacuum gap width of 0.75 mm (see Table I in Appendix A) were within the MP limits obtained by numerical simulation. Similarly, the δ_a for the Nb surface was calculated. The result is displayed in the same figure (Fig.3.8). The δ_a of Nb was below one in the whole range of field levels. Thus, the contribution of the Nb surface to MP was negligible.

3.2 Multipacting Simulation Using Multipac 2.1

Another MP simulations were carried out using 2D code MultiPac 2.1 [175], [174] to compare with those of previously achieved results using CST MWS and the PIC solver of CST PS. The program follows similar procedures of MP simulations used in CST PS. The software provides a MATLAB graphical user interface called *MultiPac Graphical User Interface* (MPGUI) to monitor the entire operation and to visualize the results [174]. The field solver of the code computes EM fields at the frequency of interest based on the FEM with special third-order elements [172]. For MP simulation, the code allows assigning all parameters, such as frequency, field level ranges, SEY, initial energy of electron, electron emission phases and an initial number of particles. The motion of a charged particle moving in EM fields is calculated based on the Runge-Kutta-Fehlberg method [175].

MultiPac supports only the axial symmetric RF structures. An ASCII-file for the geometry was generated using AutoCAD 2016 [72]. A further simplification of Model A was required to improve the exact representation of the simulated structure and compatibility. The simplified model (Model B) comprises a half-cell cavity and a simplified cathode and cathode vicinity. The outline of Model B is shown in Fig. 3.9 (a). A perfect electric boundary at the surface and perfect magnetic boundary conditions at the end of the structure were employed. Figure 3.9 (b) illustrates a TET mesh representation of the model as used in our simulations. The total number of mesh elements is around 600,000.

Then the EM fields were calculated at 1.3 GHz. The normalized electric and magnetic fields are shown in Fig. 3.10. For MP simulation, the fields were then scaled between 1 MV/m and 4 MV/m with the step of 0.5 MV/m. The seed electrons were set on the cathode wall. The electrons were emitted with an initial velocity of 4 eV and were considered to be perpendicular to the wall. Then the electron trajectories were initially calculated for one full RF period of the field, which is from 0° to 360°, with the step size (*Phase step*) of 5°. When the electrons strike the opposite wall, the generation of secondaries was calculated. The calculation was governed by the imported SEY function. Figure 3.11 shows a typical SEY model of Cu and Nb used for this simulation.

The simulation ran for a number of impacts, N, of 20. The trajectories were then computed within the specified field levels. The energy of the electron at each impact

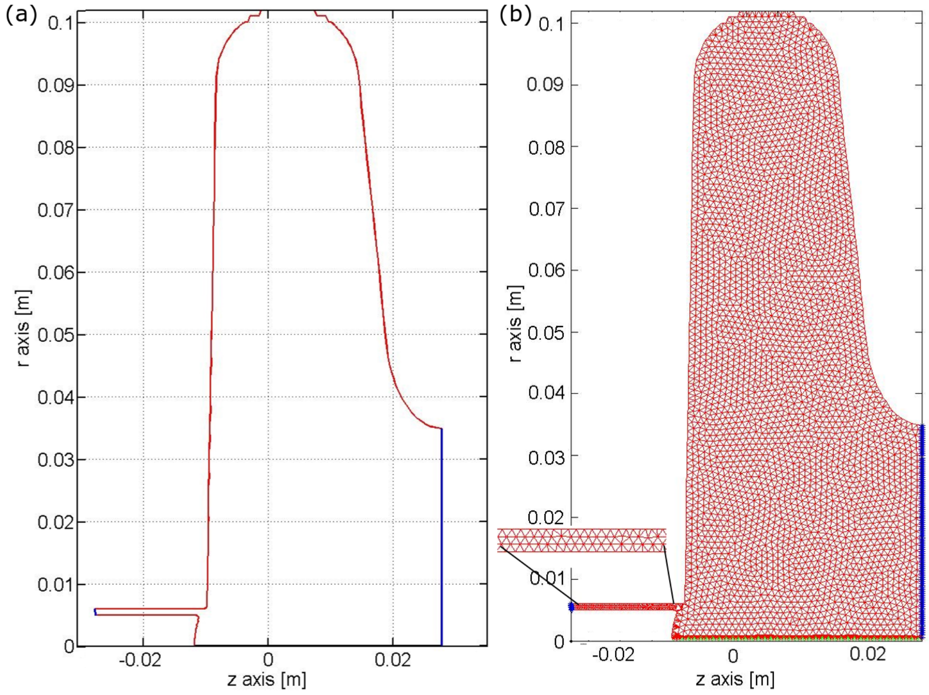

Figure 3.9: (a) The outline of Model B with a perfect electric boundary at the surface (in red) and perfect magnetic boundary conditions at the end of the structure (in blue); (b) A TET mesh used for Model B and a mesh representation of the coaxial part is shown in a zoom.

as well as the average energy of the electron for 20 impacts were also calculated. Moreover, the possible MP was evaluated as the program calculates the number of free electrons, the number of secondary electrons, the total number of electrons and the impact energy of the surviving electrons after 20 impacts. Figures presented in 3.12 illustrate trajectories of the electrons within Model B. The trajectories in the cathode vicinity were calculated over a period of 10 ns. During this time, the electrons gained sufficient energy and their motion synchronized with the fields, which resulted in stable trajectories in the vicinity of the cathode that led to 1^{st} order two-sided MP. Additionally, the peak SEY, which is greater than unity, was obtained at a field level of 112 kV/m and an impact energy 50.3 eV. The final energy of the electrons after 10 ns was 50.7 eV. The simulation results obtained here are very similar to that of CST PS results.

3.2.1 Validating Model C

With respect to MP, the cathode region is the most critical part as noted before. Also, MP is mainly confined to the cathode region. Therefore, this region is of main interest when aiming to reduce MP and it is reasonable to confine the simulation

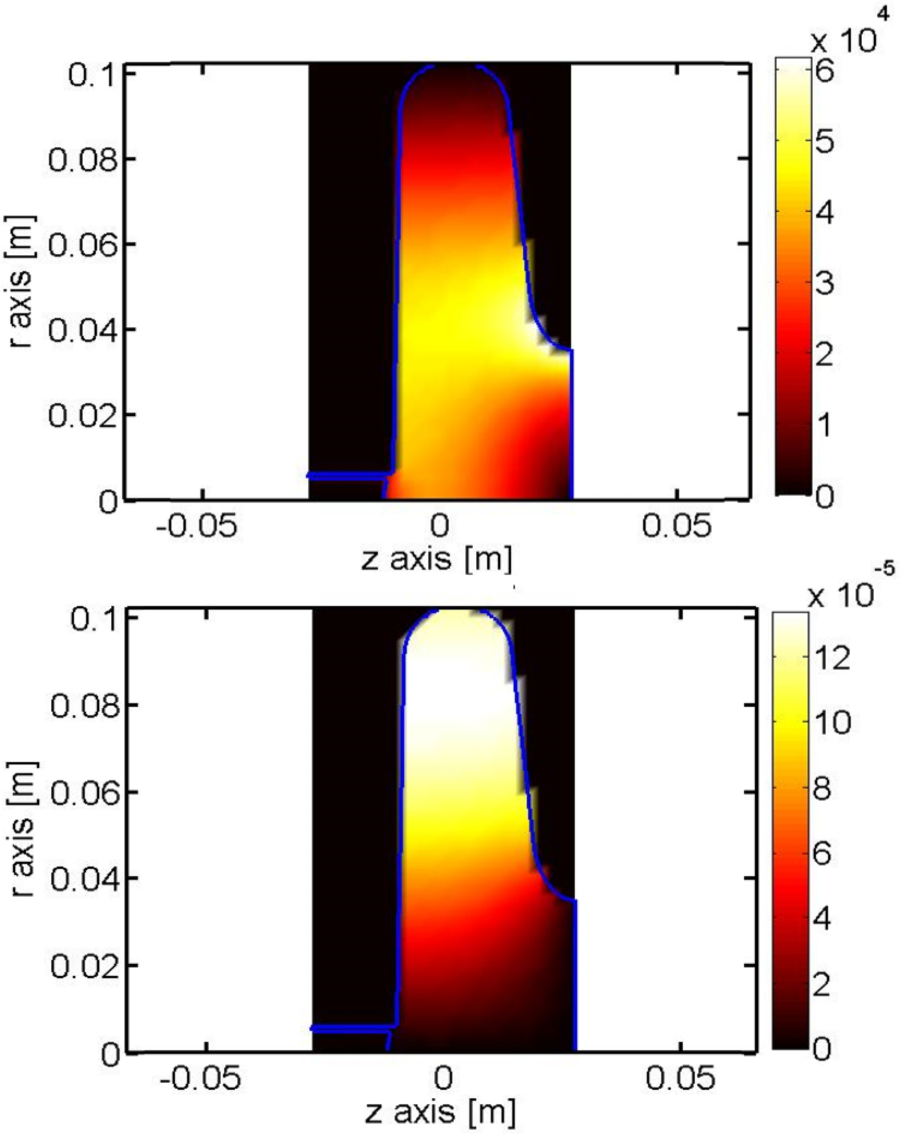

Figure 3.10: EM fields calculation for Model B using MultiPac 2.1. Upper: Electric field map; Lower: Magnetic field map.

domain to it. A simplified model would thus be covering just the coaxial part of the cathode region (Model C). The model allows employing a sufficient mesh resolution for MP simulations, while keeping the computational effort low enough for systematic optimization studies under various aspects. Model C is validated through comparison with the simulation result of Model B.

First, the distribution of the electric and magnetic fields in the Model B were calculated at 1.3 GHz using the eigenmode solver of CST MWS. The maximum electric field on-axis (accelerating gradient) was 18.3 MV/m, where the field energy

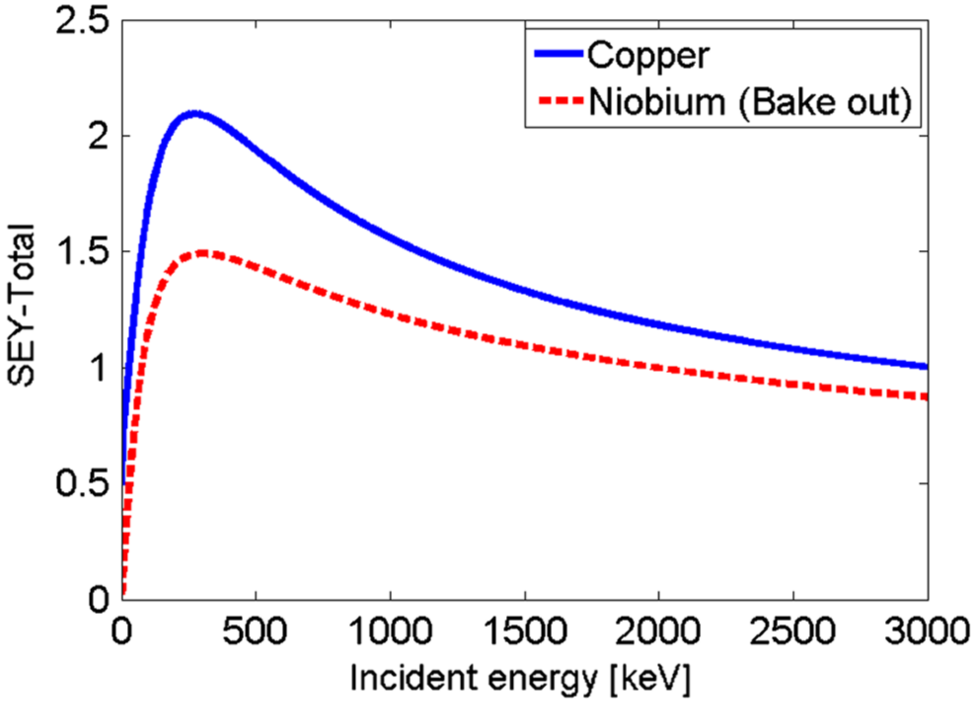

Figure 3.11: SEY of Cu and Nb used for MP simulation in MultiPac 2.1.

was normalized to 1 J. The calculated EM field was imported to the PIC solver of CST PS to track the electrons' movement in the field. Similar to the previous simulations, the δ_a for Cu at different field levels was calculated from the emission and collision data produced by the PIC solver. The calculated δ_a as a function of electric field is presented in Fig. 3.15.

Next, the simulations were carried out for a further simplified model (Model C), shown in Fig. 3.2 (d). The model just comprises a part of the cathode's vicinity having the inner conductor diameter of ∅ 10 mm and outer conductor diameter of ∅ 12 mm. Like previous models, mesh refinement studies were performed (see Appendix C). The frequency domain (FD) solver of CST MWS was applied to calculate the EM fields at 1.3 GHz utilizing a waveguide port shown in Fig. 3.13 (b). Based on the boundary conditions shown in Fig. 3.13 (a), one obtains a standing wave field in the coaxial line structure of Model C with a maximum electric field of 15.03 kV/m for an input power at the waveguide port of 1 W. The field pattern in Model C is illustrated in Fig. 3.14. Then, the calculated EM fields were imported into the PIC solver of CST PS to compute MP.

Figure 3.15 illustrates that the peak δ_a was obtained at the gap field of 112.6 kV/m. The corresponding electric field in the half-cell cavity for that case was 1.55 MV/m. In the same figure, the δ_a curve (in red) for Model C shows that the field level of the gap field is in the same range of Model B, although the field interval with MP

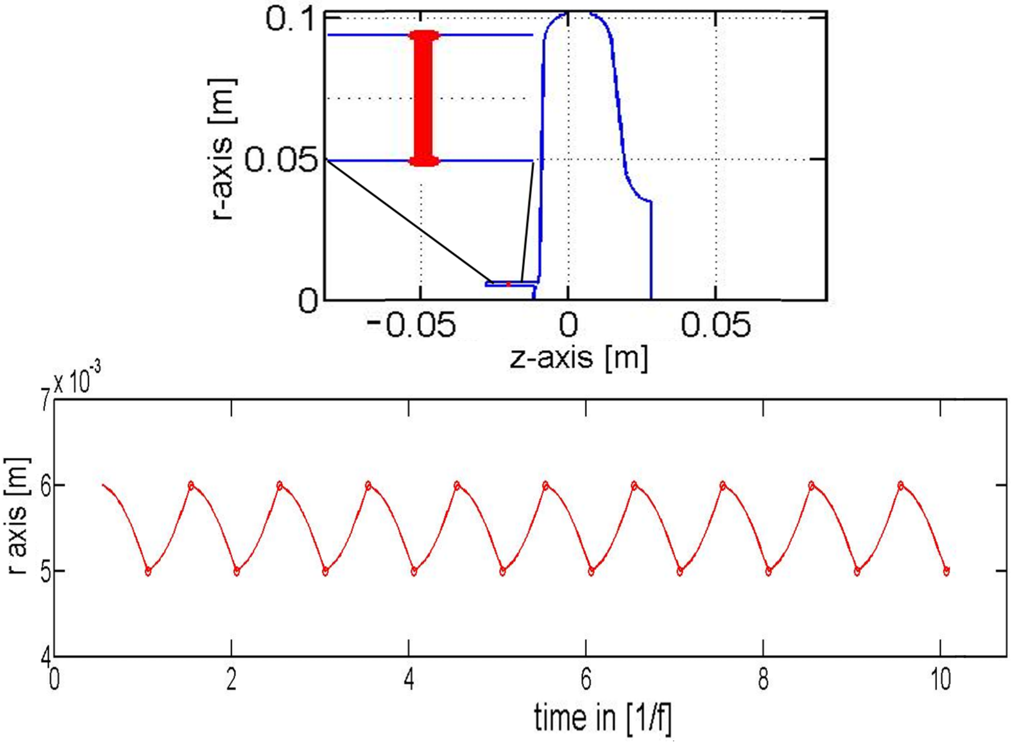

Figure 3.12: The computation of the electron trajectories using MultiPac 2.1.; The upper plot shows the whole geometry plus the trajectory in its coaxial part in r,z coordinates. To see the trajectory closely, the coaxial part is shown in zoom-view in the same figure. The lower plot shows the trajectory of the electrons as a function of time.

is somewhat narrower. Since the values close to the maximal δ_a were similar, it is reasonable to consider only the coaxial part of the structure, i.e., Model C, for further investigation.

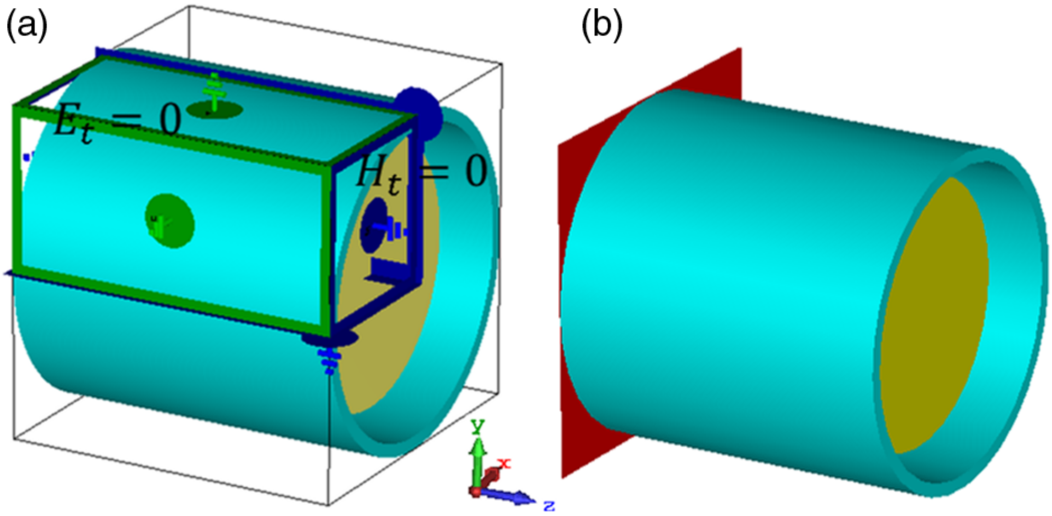

Figure 3.13: (a) The PEC (green) and PMC (blue) are specified on the boundary and the symmetry plane. (b) A waveguide port (in red) is used as the excitation source.

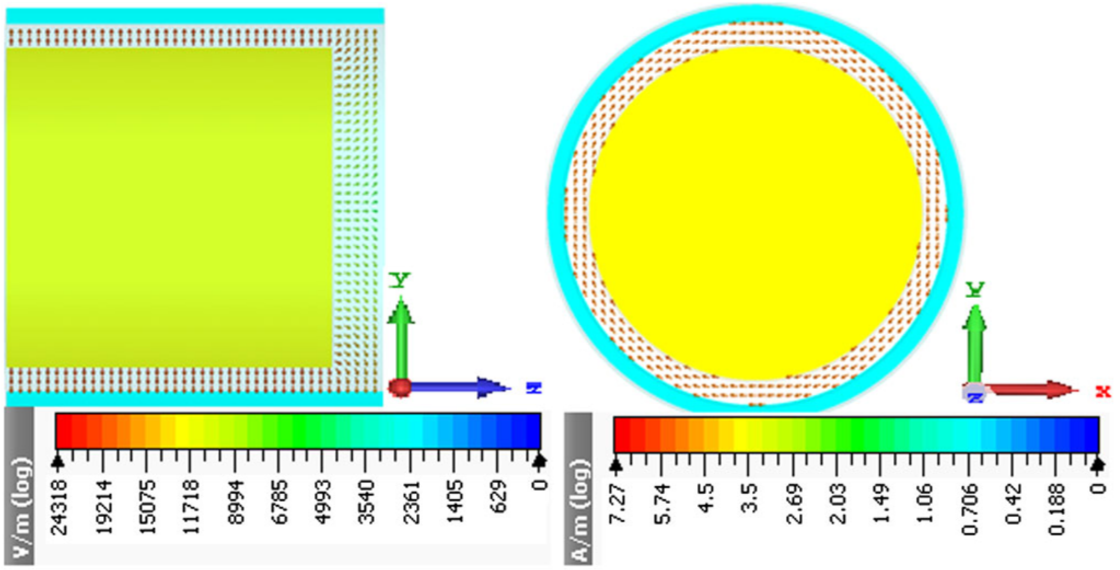

Figure 3.14: Electromagnetic field in the coaxial line structure at 1.3 GHz. Left: Distribution of the electric field; Right: Distribution of the magnetic field.

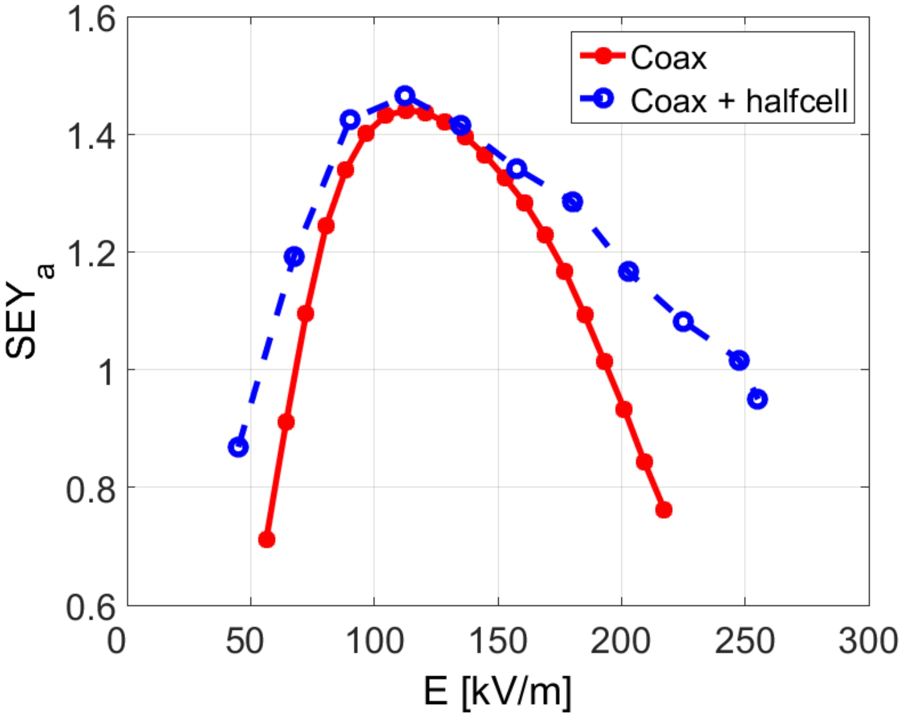

Figure 3.15: Comparison of the two models: coaxial (Model C) vs. the coaxial structure plus half-cell cavity (Model B). The SEY$_a$ curves as a function of the electric field for a Cu surface.

4 Multipactor Suppression Techniques

Several methods have been proposed and investigated to develop effective approaches to mitigate MP phenomena for different RF components. For example, RF conditioning of the RF structures in order to raise the voltage above the MP zone before the discharge has time to build up [165]. However, this technique is time-consuming and can not always stop MP at the operating gradient level. Treatment of metal surfaces by pulsed-laser irradiation [145] and cleaning the surface of the RF components [60] are other approaches. Cleaning is an effective method to prevent MP by avoiding impurities from the inner surfaces and to make SEY_a low. To set up the cleaning procedure is nevertheless complicated in most cases as the RF structures are usually complex. Anti-MP coatings, such as Titanium-based, e.g. titanium nitride and thin titanium metal films, and Carbon-based coatings, have been also recommended to introduce low surface conductivity [94],[113],[153],[150]. An experimental study of carbon films demonstrated a reduction of SEY below unity [113],[150]. Yet, the film coating is generally challenging in the sense of obtaining the material which is compatible with the requirements of high-Q RF systems. Another approach is geometry modifications or choosing geometries that are less susceptible to MP, e.g., elliptical cavity shapes that diminish MP phenomenon from superconducting cavities [65], [67]. Biasing a DC electric or magnetic field on the surface (static perturbation) can also be used to perturb the resonant conditions of the particle trajectory. Ylä-Oijala presents a detailed numerical analysis of the effectiveness of the DC electric biasing method to mitigate MP in straight coaxial lines and ceramic windows [171],[176],[75]. Similarly, numerical studies of DC magnetic field biasing technique demonstrate suppression of MP in a rectangular coupler waveguide and in a coaxial line [45],[49],[50]. Although the static perturbation method is effective to subdue MP in such structures, they might cause one-sided or other types of MP, e.g [171]. The other technique for MP suppression is anti-multipactor grooves, e.g., rectangularly and triangularly grooved surfaces, that breaks a resonant condition of MP by trapping the electron in its wall. Recent theoretical and experimental studies show that changing surface profiles (surface-grooving) of different RF structures is a good candidate to suppress MP and improve the breakdown threshold for multipactor [129],[70],[152],[102],[25],[2],[168], [112],[100].

In the present work, the latter four approaches, namely geometric modifications, such as frusto-conical cathode and varying the gap width, static electric field perturbation, anti-multipactor grooves of the cathode's surface including rectangular, sawtooth, isosceles, and anti-MP coatings, were investigated numerically to tackle

MP in the SRF gun. Those remedies were applied to the cathode vicinity of the SRF gun to check if they allow the MP conditions to be broken down. The results are discussed below.

4.1 Geometry Modification

A larger gap between the choke and the half-cell should be advantageous to improve the cleaning of the choke filter. According to the scaling law for the MP threshold, which was studied in [176], MP may be cured by modifying the dimensions of the inner and outer conductors of the coaxial line. Therefore, this concept was carefully adapted in this study, as the geometry of the SRF gun cannot be changed. For this method, the numerical investigations were performed in two approaches: first, varying the diameter of the outer conductor and second, developing the frusto-conical shape of the cathode stem.

4.1.1 Varying the Gap Width

In case of the *two-sided* or/and the *two-point* MP for coaxial lines, the discharge process of MP depends on the RF frequency, f and dimension of the gap given by the diameter D_o of the outer conductor (see Fig. A.1 in Appendix A). Based on the latter two parameters, the scaling law for the average impact energy (U_a) is approximated as [126]

$$U_a \sim (f D_o)^2. \tag{4.1}$$

Therefore, the MP behavior of larger gap widths was investigated at 1.3 GHz numerically. The computations were carried out for gap widths d [cf. A.1] of 0.75, 1.5, and 3 mm by changing the diameter of the outer conductor D_o [cf. A.1] to 11.50, 15.50, and 17.50 mm, respectively. The inner diameter D_i of the cathode was kept constant at 10 mm. Moreover, the simulation results of these gaps were compared with a theoretical prediction summarized in Table 4.1. The formulas can be found in Appendix A.

Gap width	d = 0.75 mm		d = 1.5 mm		d = 3 mm	
Order of MP	n = 1	n = 2	n = 1	n = 2	n = 1	n = 2
V_g [V]	67.7	22.6	270.8	90.3	1083	361
E [kV/m]	90.3	30.1	180.5	60.2	361	120.3
U [eV]	43.1	4.8	172.4	19.2	689.5	76.6

Table 4.1: Analytical solution for first and second order of two sided MP in 0.75 mm, 1.5 mm and 3 mm gap width d.

For the following comparison of the three models, only the results for Cu (cathode surface) are discussed in the sense of a worst-case study due to its larger SEY_a or δ_a. Figure 4.1 shows the evolution of the aggregate number of particles as a function of time for the d of 1.5 mm. Already within the first 10 ns a significantly higher number of secondary electrons was produced than at $d = 0.75$ mm. Since the simulation above 153.7 MV/m would also lead to a disproportionately high computing time, the calculation was limited to the first 10 ns due to this clear result. The calculated δ_a with respect to the lower and upper field limits, as well as the corresponding impact energy for this model, is illustrated in Fig 4.2. The peak SEY_a (~2.1) was only generated at the average gap field of 165.5 kV/m with a corresponding U_a of 162 eV. The E_{min} and E_{max} are ~95 and 336 kV/m with impact energies of ~35 and 206 eV, respectively. In comparison to the present gap of 0.75 mm, the enlargement to 3 mm is considerably shifting MP upwards to higher field levels. The peak δ_a (~2.1), for example, was only generated at 353.8 kV/m with a corresponding impact energy of 387.3 eV. The same is true for E_{min} and E_{max} of ~190 and ~596 kV/m as well as impact energies between ~40.1 and 712 eV. Very strong and consistent MP barriers were observed for 1.5 and 3 mm gaps. Also, a larger gap shifts all fields to higher values. However, the SEY_a are about the same for 1.5 and 3 mm, although at different field levels. In general, the field range in which MP occurs increased by a factor of approximately 1.8 when doubling the gap width. As Fig. 4.2 shows, a

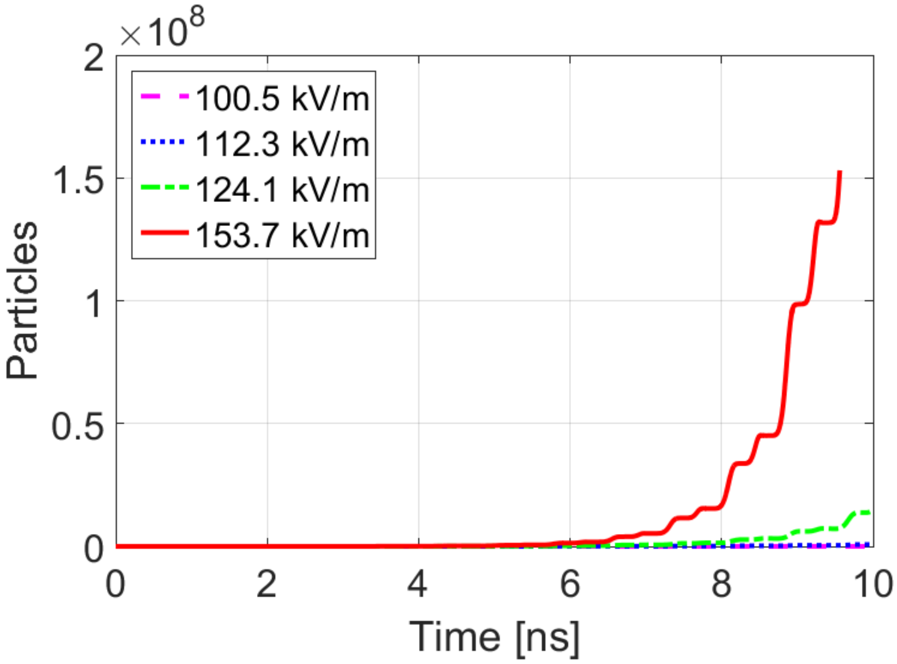

Figure 4.1: Number of particles as a function of time (in ns) for 1.5 mm gap width of the coaxial line structure.

3 mm gap improves the lower electric field threshold for MP compared to the other two gap widths. However, MP is even stronger and broader at higher fields. More specifically, as previously mentioned, for the latter gap, MP would occur between E_{min} and E_{max} with ∼190 and ∼596 kV/m gap electric field, respectively. This range of fields corresponds to 2.66 to 8.2 MV/m in the half cell. These fields are still in the working range of the SRF gun. Therefore, due to the higher δ_a and the broader field range where MP may occur, the larger gaps are not preferable here.

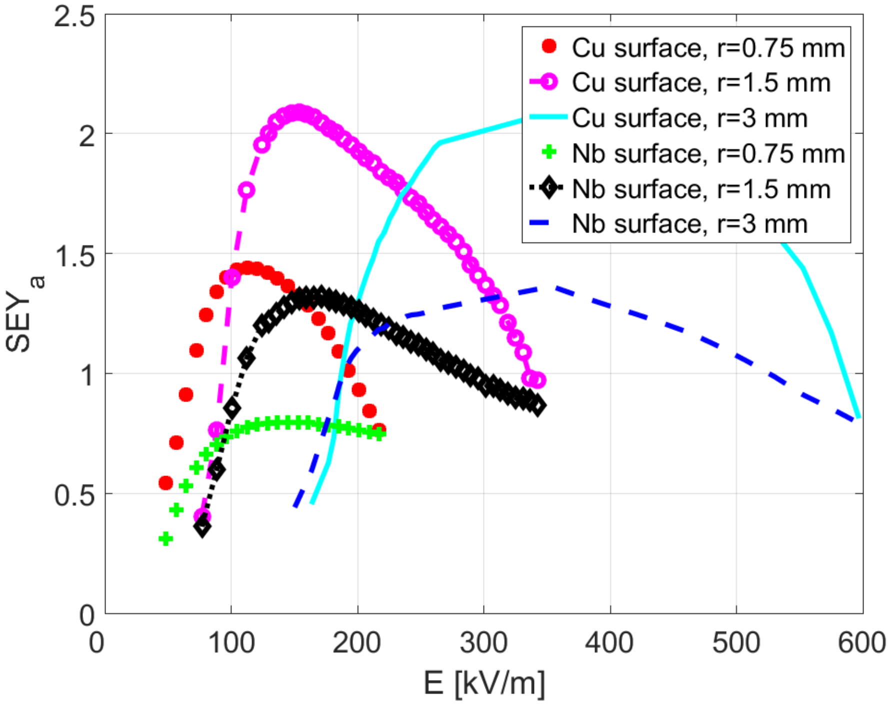

Figure 4.2: Average SEYs of Cu and Nb surfaces as a function of gap electric field amplitude for 0.75, 1.5 and 3 mm gap width of the coaxial line structure.

4.1.2 Frusto-Conical Cathode

The other method of geometrical modification is the frusto-conical cathode, as noted before. To have a better understanding of the effect of this model on MP, at least three cases were considered in this work. The three models are depicted in Fig. 4.3. The model consists of the outer part of Nb and the cathode stem (inner side) of Cu. To develop the shape and to vary the geometry at different positions separately, the cathode stem was cut into two parts. The diameter D of the cathode stem at three positions were varied, while the existing diameter of the cathode was 10 mm. Then,

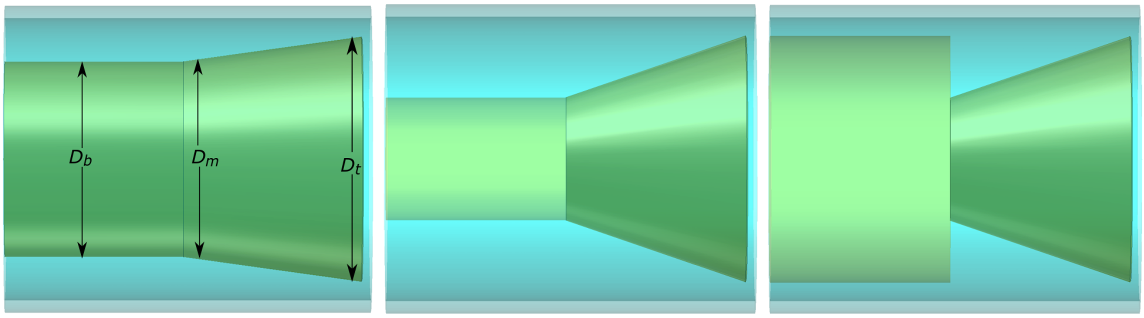

Figure 4.3: Frusto-conical cathode models for three cases of geometry setup. Left: Case-1 with 5 mm of D_t, 4 mm of D_m and 4 mm of D_b ; middle: Case-2 with 5 mm of D_t, 2.5 mm of D_m and 2.5 mm of D_b; right: Case-3 with 5 mm of D_t, 2.5 mm of D_m and 5 mm of D_b.

three geometrical parameters, namely D_b, D_m, D_t, were considered for each of the three cases. The values of these parameters are listed in Table 4.2.

Parameter	Case-1	Case-2	Case-3
D_t [mm]	5.0	5.0	5.0
D_m [mm]	4.0	2.5	2.5
D_b [mm]	4.0	2.5	5.0

Table 4.2: Geometric Parameters for Frusto-conical like Cathodes.

The EM field was calculated in the models using the FD solver of CST MWS. A waveguide port was utilized for the excitation source. The BC of PEC and PMC were applied on the surface and on both ends of the structure, respectively. Moreover, two symmetry planes modeled by magnetic BC were applied, which reduced the computational domain by a factor of four. As noted before, this is not the case in PIC solver, as PIC simulation doesn't support symmetric BC. The EM field distribution was computed on meshes with $\mathrm{N}_x = 69$ $\mathrm{N}_y = 40$ $\mathrm{N}_z = 40$; $\mathrm{N}_x = 69$ $\mathrm{N}_y = 40$ $\mathrm{N}_z = 40$; $\mathrm{N}_x = 69$ $\mathrm{N}_y = 41$ $\mathrm{N}_z = 41$; of nodes for the first, second and third of model, respectively. The calculated EM field was imported into the PIC solver for MP simulations. In the PIC solver, the *point-source-like* initial electron emission was assumed for the inner side of the Nb surface. The detailed set up of the particle source is presented in Table 3.1.

Figure 4.4 presents the electric field distribution of the three proposed models. A heterogeneous field distribution is depicted within the models. The strongest field distribution is observed nearby the end of the half-cell (at D_t). The shape of the models was assumed to break down the resonant conditions by disrupting the transit time of the electrons between impacts as well as by trapping the electrons, where the electric field strength is weak. However, almost in all cases, the close observances on

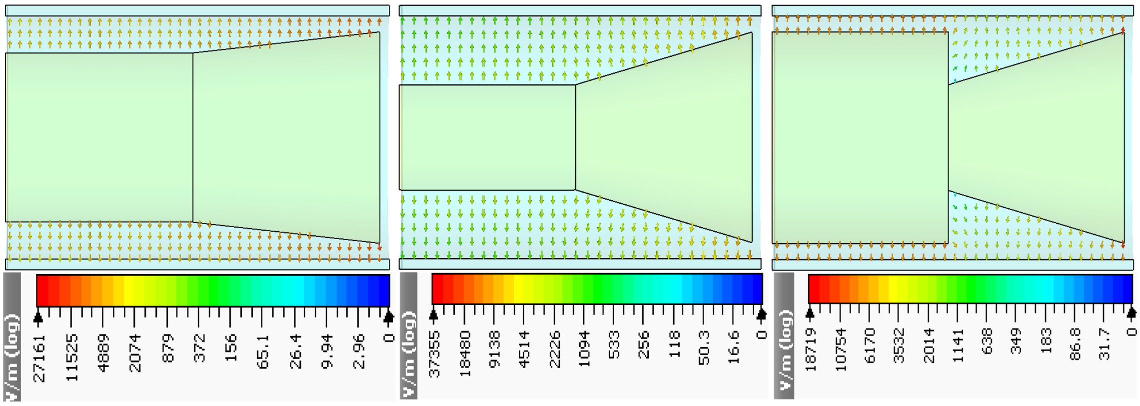

Figure 4.4: Electric field distribution within three Fursto-conical-like models on the cut plane (2D). Left: Case-1; middle: Case-2; right: Case-3. The maximal field values are clamped to different values for better visualization of the results, i.e. 27,161 V/m for Case-1, 37,355 V/m for Case-1, and 18,719 V/m for Case-3, respectively.

the particle trajectories revealed that certain electrons flew to nearby the end of the half-cell. As a result of that, the secondary electrons were gaining sufficient energy to grow exponentially due to the locally higher electric field magnitude. The δ_a was also

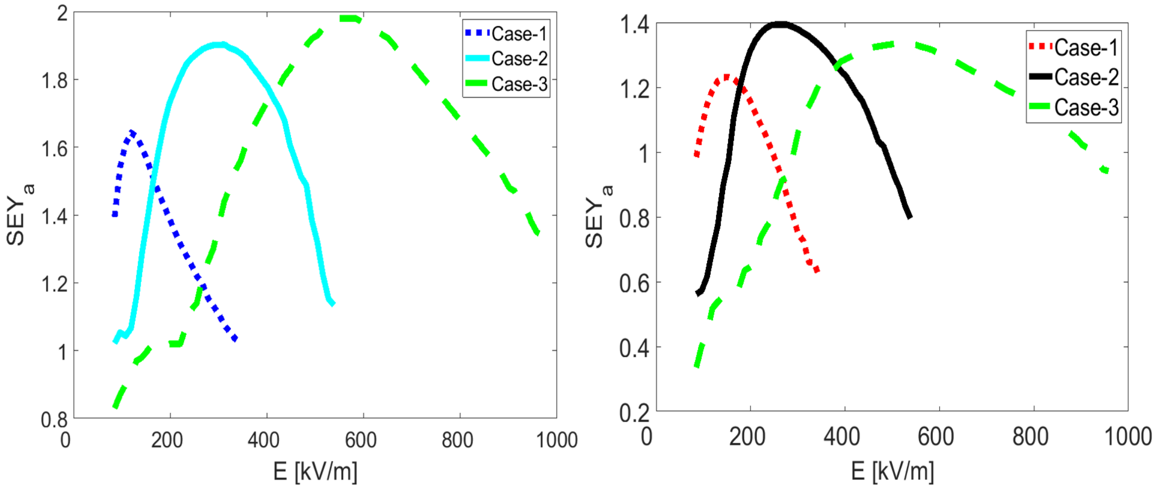

Figure 4.5: The SEY$_a$ for three cases of Fursto-conical models as a function of the electric field. Left: SEY$_a$ function for Nb surface; Right: SEY$_a$ function for Cu surface.

calculated for the Cu and Nb surface for various field levels separately. Figure 4.5 illustrates that almost in the case of all three setups, the δ_a values for the Cu surface are above unity for the entire range of field level. These results also revealed that strong emissions in all cases of Cu surface rather exist for the broader range of field compared to the result obtained within Model C, as presented in Fig. 3.8. Moreover, unlike Model C, the Nb surface has a considerable contribution to the emission of secondary electrons. Thus the Frusto-conical-like models were unsuccessful in being a cure for MP.

From the close monitoring of the particle trajectories, the Case-3 geometry setup seems to be a promising model as the decreasing number of particles was observed at 112 kV/m, where the peak δ_a was obtained in Model C, in the first few ns of simulation time. Yet, the number of particles started to rise after a certain time due to the surviving particles reaching the top of the cathode, where the magnitude of the electric field is high. Then, these particles continued to produce secondaries by impacting the wall with adequate energy. Furthermore, the secondary electron emissions for Cu surface have occurred in a vast range of electric field levels of 153 kV/m to 969.1 kV/m. The peak δ_a of 1.98 was obtained at $\sim$562 kV/m. The corresponding impact energy is 350.3 eV. In the case of Nb surface, although the δ_a values were low in those ranges of electric fields, they were not negligible as some values were still above unity.

The Frusto-conical-like geometries of Case-1 and Case-2 models also exhibited possible secondary emissions and multipactor effect. The former model showed less electron emission compared to the other two models (Case-2 and Case-3). However, the δ_a values of the Cu surface were greater than unity at all field levels. The peak δ_a of this surface is 1.64 at $\sim$119 kV/m. In the second model, the peak δ_a of $\sim$1.903 and $\sim$1.394 for Cu and Nb surfaces, respectively, at field level of 311.7 kV/m. The peak secondary electron emissions at both surfaces corresponded to impact energy $\sim$ 282.51 eV and $\sim$ 318 eV, respectively.

4.2 DC Biasing (Static Electric Perturbation)

The *two-sided* MP is commonly observed in the coaxial and rectangular couplers. A similar kind of MP was observed in the coaxial line structure of the cathode vicinity of the SRF gun in Dresden-Rossendorf, as noted in chapter 3. Successful suppression of MP is demonstrated in these kind of structures by DC biasing method [176],[45],[50]. A detailed analysis of this method to suppress MP in coaxial lines was discussed in [126],[176]. The idea behind applying a DC electric bias is to perturb the flight time of the particles between impacts so that the resonant conditions for MP can be disrupted [64]. In general, the set up of these simulation studies closely follows the DC electric bias method for a coaxial coupler. In a coaxial line structure, the optimal suppressing DC voltage for the standing wave can be set by [126]

$$E_{DC}(r, z) = \frac{V}{\ln \frac{r_{\text{out}}}{r_{\text{in}}}} \frac{1}{r}, \tag{4.2}$$

where r_{out} and r_{in} are the outer and the inner radius of the structure and $(r,\, z)$ are the radial and longitudinal coordinates of a field point in a cylindrically symmetric structure. The suppressing DC voltage (V) satisfies the following general scaling law:

$$V \sim Dzf, \tag{4.3}$$

where f is the frequency, and D is the outer diameter of the coaxial line. To study the effect of the DC electric bias on MP in the cathode vicinity, the simulation has been performed in two ways: defining the voltage directly at the cathode and importing an electrostatic field to the cathode region after computing it separately. In both cases, the results were similar. The results were obtained by varying the suppressing DC voltage in the range of 15 to 500 V. As it is illustrated in Fig. 4.6, MP is totally suppressed from the vicinity of the cathode in the case of 100 V after 1.5 ns. It could also be sufficient to supply 50 V to the device in order to suppress MP. However, practically, a high voltage (up to 7 kV) is required at the cathode to suppress MP [134]. Therefore, further experimental studies might be required to match the results.

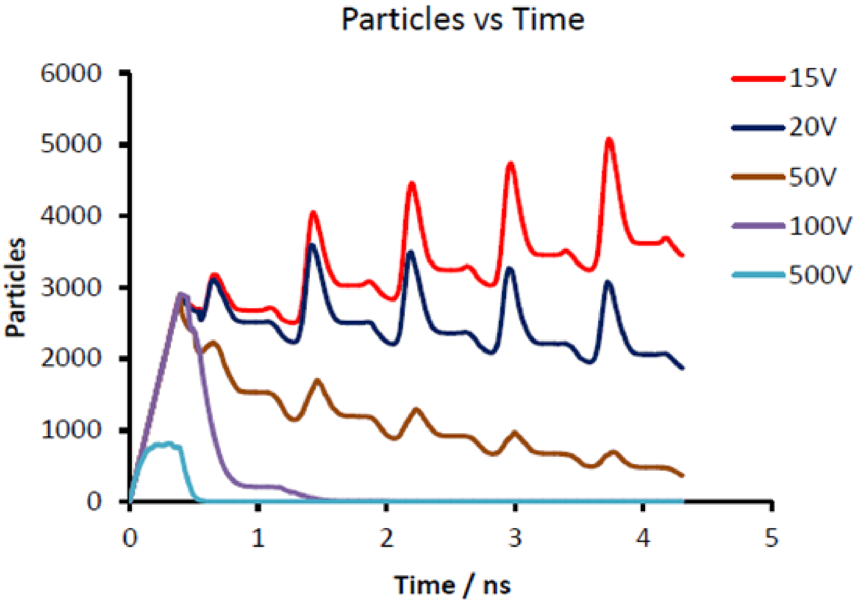

Figure 4.6: Number of particles as a function of time for various DC bias voltages. MP can be suppressed in case of 500 V and 100 V.

4.3 Anti-Multipactor Grooved Surface

The basic principle to suppress MP discharge using a grooved structure is to disturb the resonant condition by altering the trajectories of the electrons and by diminishing the transit time. Consequently, the secondaries are trapped by the grooved surface. Such kind of surface was first proposed in [70]. Recent experimental and numerical studies exhibited the success of this approach in reducing the emission of secondary electrons for different RF structures [152],[20],[102],[2],[153],[169]. This work closely follows the general concept of those studies. The grooved surface can be manufactured, for example, mechanically by rolling or extrusion and by infrared laser [151].

In the present study, the models, such as cylindrically symmetric rectangular groove (CSRG), cylindrically symmetric isosceles groove (CSIG), and cylindrically symmetric sawtooth groove (CSSG) on the cathode stem surface, were developed. The Cu material of the inner surface and the Nb material of the outer surface with a peak SEY of 2.1 and 1.4, respectively, were considered in all three cases. Because of practical reasons, grooving was considered only on the Cu wall, i.e., the inner part of the coaxial line structure.

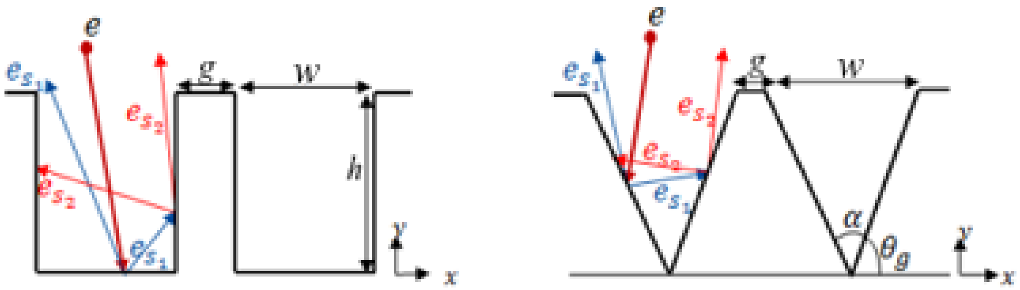

Figure 4.7: The movement of exemplary secondary electrons in the grooved surfaces. Left: Rectangularly grooved surface; Right: Isosceles triangularly grooved surface ($\theta_g + \frac{\alpha}{2} = \frac{\pi}{2}$).

Figure 4.7 displays a graphical sketch of the motion of exemplary secondaries in the rectangular and triangular grooved surfaces. The electron e^- enters this surface and hits the wall with a certain impact angle. Thus, the first secondaries (e_{s_1}) are produced. Some of these secondaries might escape the groove depending on the impact angle. The others hit the opposite side of the wall, where either they might be absorbed or a second-generation electron (e_{s_2}) might be produced. This process is repeated until the energy of the higher generations becomes too low, and all secondaries are absorbed by the surface [102]. In general, most secondaries are unlikely to survive after multiple collisions.

The success of this method to mitigate multipactor discharge was intensively investigated in this work. The numerical studies of the grooved models demonstrate a significant reduction of the number of particles during the first 5 ns of the computation. Therefore, based on these simulation results, the models were then further optimized using a *Trust-Region* algorithm so that the optimal geometry was found to suppress MP. Up to now, there are only few research results on geometric parameters of such kind of grooved models. To the best of this author's knowledge, such an approach of global optimization wasn't considered for grooved types of models yet. The optimization algorithm will be briefly discussed below.

4.3.1 Multi-dimensional Optimization using Trust-Region Algorithm

First, the geometric parameters of the grooved surfaces with respect to the number of particles over time were optimized manually. The optimization results will be discussed below. This gives certain flexibility to choose dominant parameters for further optimization studies. Then optimizing the geometric parameters of the models was done using the so-called trust-region algorithm, which is implemented in CST [3]. The initial parameters were chosen based on the manual optimization results, which was already close to optimum. The automated optimization of the grooved surfaces is based on the optimization goal that the δ_a is lower than the threshold, i.e., less than unity, for each possible combination of parameter values. Additionally, the impact energy is expected to be lower than the first crossover energy of the SEY curve for the materials.

Line search and *trust region* methods are two traditional numerical iterative methods for solving optimization problems. Unlike the line search approach, the trust-region method (TRM) calculates a new iterative point within a *trust-region* at the current iterate, while line search method computes a new iterative point along a descent direction at each iteration. K. Levenberg initially introduced the TRM in 1944 as a modified version of the Gauss-Newton method [74]. The work was then extended and advanced by many researchers. The method is well reviewed in [177], [178].

The TRM basically carries out three main steps to obtain optimum parameters. First, based on a model function, the objective function will be approximated within a *trust-region* in which we trust our model. The original objective function $\min_{x \in X} f(x)$, where $X \subset \mathbb{R}^n$, is approximated either by a quadratic or a linear model. In CST PS, the linear model function $m_k(s)$ is used to approximate $f(x)$. With a given initial point, the $m_k(s)$ builds up in a *trust-region.* In the case of our optimization problem, the initial parameter values and the initial parameter bounds or the initial trust-region radius, Δ_k, were chosen based on our previous manual optimization work, which will be discussed in the following sections. In the next step, the algorithm solves the trust-region subproblem to determine a candidate trial step (s_k). TRM resolves the subproblem if the trial step results in an increase in the objective function. Then, if the solution indicates an acceptable reduction of the goal function, the radius of the trust-region will be updated (increased) for the next evaluation. This will be repeated until convergence. The basic algorithm is stated in Appendix D. The algorithm can be chosen as a global or local optimization in CST PS.

4.3.2 Effect of CSRG Surface on Multipactor Discharge

The CSRG surface is depicted in Fig.4.8 (left). The structure is mainly described by three parameters, the width, w, the depth, h, of each groove, and the distance or gap between two neighboring grooves, g. The grooves tips and valleys were rounded with a radius of 0.05 mm and 0.001 mm, respectively. Such a structure provides an attenuated amplitude of the electric field at the bottom surface, and thereby the electron energy was reduced remarkably. More importantly, this surface limits the electron transit distance so that many electrons might impact the sidewalls and the bottom of the grooved surface with low energy several times during a half RF period. Thus, the resonant condition discussed in Section 2.5 might not be fulfilled, and thereby the δ_a reduces.

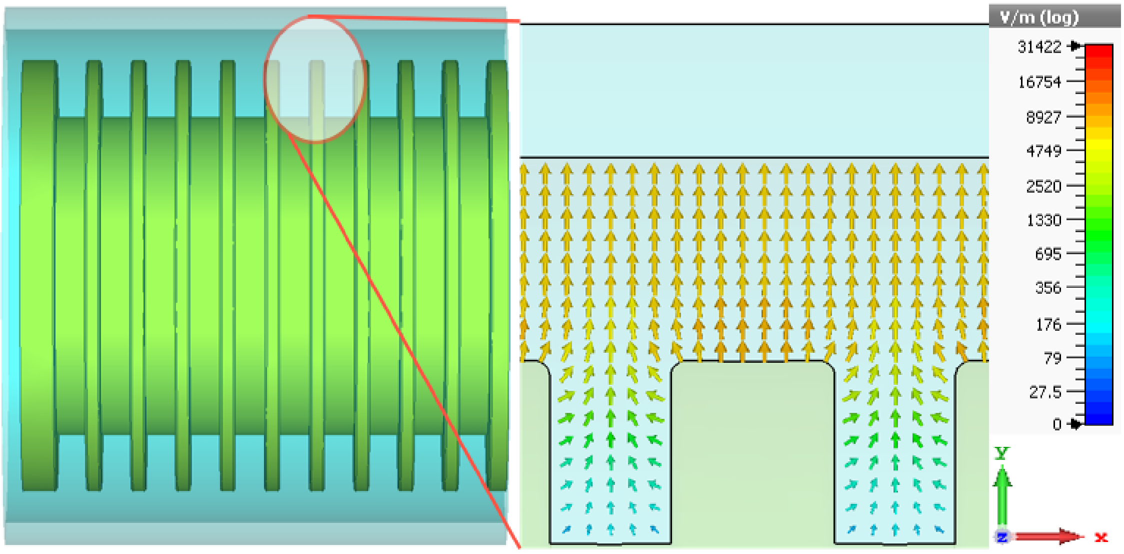

Figure 4.8: Left: The profile of CSRG surface; Right: Electric field distribution inside of two CSRG surfaces on the z-cut plane.

The EM fields at 1.3 GHz were calculated using the FD solver of CST MWS. The electric field distribution in the CSRG model is shown in Fig. 4.8. The model was equipped with a *waveguide* port similar to model C shown in Fig.3.13. The PEC and the PMC BCs were used at the surface and at the end of the structure, respectively. Furthermore, the two symmetric boundary planes modeled by magnetic BC were applied, as illustrated in Fig. 3.13. The latter reduces the computational resources, such as computation time and memory, due to the reduced domain size. To obtain a field map with sufficient accuracy, for a reduced calculation domain of CSRG surface, 65 cells per wavelength, were required, resulting in a number of about 743,444 mesh cells (with $N_x = 222$, $N_y = 59$ and $N_z = 59$ nodes). The calculated EM fields were imported into the PIC solver to proceed with the MP simulation. The amplitude of the electric field was scaled in the PIC solver based on the actual electric field in the cavity.

The motion of the electron is usually closely associated with the initial condition of the seed electron and the field pattern. The parameters used for the initial electrons are similar to the previous simulations in Chapter 3. Gaussian PIC emission model with the kinetic energy of 4 eV was considered as a *point-like* particle source in the cathode vicinity. The electrons emitted at the 210° phase of the field, were the highest number of particles observed within Model C. Furman's SEY models have been considered for the cavity pipe wall as well as the cathode. In the case of PIC simulation, as a full computational model was considered, around 2.9 million mesh cells were utilized. The solver used a computational time of around 3 hours for each individual simulation run. Five to six PIC solver simulations were run within 10 ns for each parametric geometry study. First, the simulations were done varying only one geometric parameter at a time, while considering the other parameters constant.

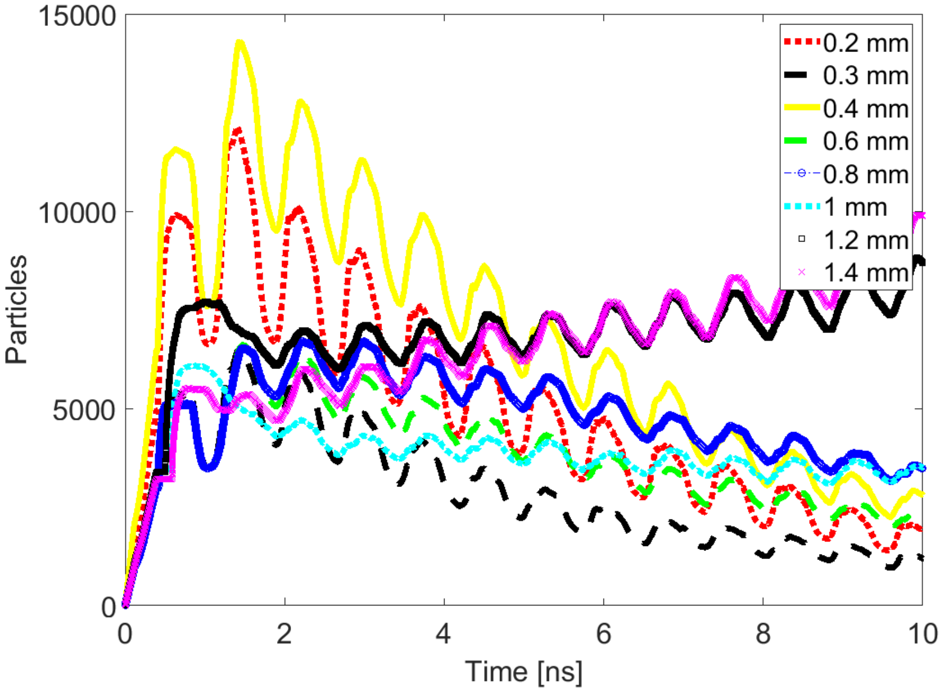

Figure 4.9: Left: Number of particles over time in case of varying the width w of the CSRG surface.

The probability of an electron entering into the grooves and being captured by the CSRG surface depends on the width w. The effect of w was investigated with the values of 0.2 mm, 0.3 mm, 0.4 mm, 0.6 mm, 0.8 mm, 1.0 mm, 1.2 mm and 1.4 mm, while the depth $h = 0.8$ mm and the distance between two neigboring grooves $g = 0.4$ mm were assumed constant. The simulation results reveal that the number of particles were significantly reduced for a width w ranging from 0.2 mm to 1.0 mm as shown in Fig. 4.9. However, if the groove is wider (see the result of 1.2 mm and 1.4 mm), the number of particles starts to increase within 10 ns. This is for two reasons: the electron can easily escape the groove and hit the wall within half-RF period and/or secondary electrons are produced in the groove itself as the electrons impact the side walls of the groove.

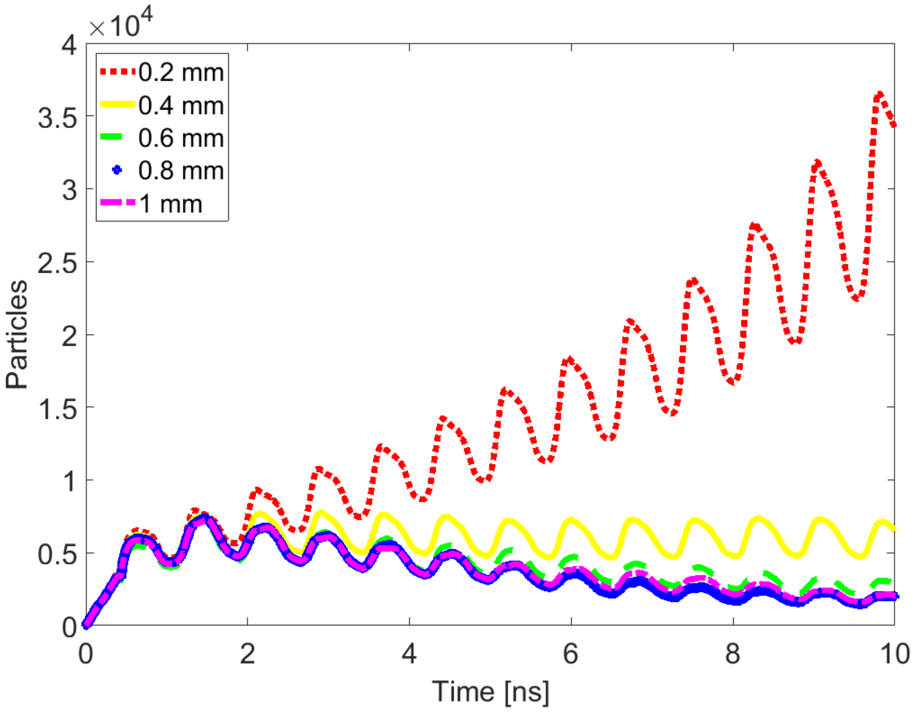

Figure 4.10: Left: Number of particles over time in case of varying the height h of the CSRG surface.

Figure 4.10 shows the number of particles as a function of time within the CSRG model for different values of height h. The influence of h was studied by varying its value from 0.2 mm to 1 mm. The other parameters such as the width $w = 0.4$ mm and the distance between two neighboring grooves $g = 0.4$ mm were kept constant. A deeper height h demonstrates a total suppression of the emission of secondaries. The electrons were trapped in the CSRG surface with the large h, as the surface provided sufficiently attenuated electric field and destroyed the resonant conditions of the trajectories of the particles. If h is too small, for example 0.2 mm, as shown in Fig. 4.10, the electrons can easily escape the groove and produce the secondary electrons by maintaining the resonant conditions. In this case, MP can occur. A similar study was carried on the distance g between two neighboring grooves. The effect of this parameter on δ_a was comparatively small within a wide range. A significant reduction of the number of particles was observed for a distance g between two neighboring grooves between 0.2 mm and 1.8 mm within 10 ns. A very slight increase was detected only for a distance g of 2 mm. Based on these simulation studies, to determine the best optimal model, the parameters w and h, i.e. width and height of the rectangular grooves, were further optimized.

The model was then optimized with respect to δ_a of the Cu and Nb surfaces using the *trust region* algorithm, as already noted. The initial parameters were chosen based on the above manual optimization results, which was already close to optimum. This gave some flexibility to choose a dominant parameter for the optimization of the grooved surface. The optimization goal was to have a δ_a less than unity. Additionally, the impact energy is expected to be lower than the first crossover energy, U_{c1} of the SEY curve of the respective material. Even though a rather powerful computer (Intel(R)CPU E5 with 3.30 GHz and 256 GB) was used for our optimization of such complex surfaces, the computational time still typically takes around three hours for one iteration of the PIC solver with 2.9 millions mesh cells. Using the TRM, the solver was carried out 18 times to obtain the best optimal parameters.

Yet, the best optimal parameters of the CSRG surface are a width of $w = 0.328$ mm, a height of $h = 0.865$ mm and a distance between two neigboring grooves of $g = 0.48$ mm. For these parameters, the δ_a for Cu and Nb surfaces reached 0.93 and 0.63, respectively, at 112.6 kV/m, where the peak generation of secondaries was observed within Model C. The corresponding average impact energies for Cu and Nb were 21.1 eV and 49.1 eV, respectively. These values are lower than the first crossover energies (U_{c1}), i.e., 27.3 eV and 76 eV, for Cu and Nb, respectively. The optimization procedure and some results are presented in Appendix D. Next, the amplitude of the electric field was swept for the wide range of 78.62 to 215.3 kV/m in order to obtain the limits of field levels for MP for the optimal parameters. As illustrated in Figure 4.11, all values of the calculated δ_a for Cu and Nb stay below the threshold, which is unity. Therefore, MP can be avoid at all field levels.

4.3.3 Effect of CSIG and CSSG Surfaces on Multipactor Discharge

Next, the influence of two triangularly grooved surfaces, namely the CSIG and CSSG, to MP were investigated. The CSIG surface (shown in Fig. 4.12) was constructed from two tilted surfaces with the same grazing angle of θ_g. The groove tips were blended as noted before, since practically manufacturing the sharp tips is expensive [152], [102] and must also be avoided per se due to otherwise occurring excessive field enhancement. The blend radius is 0.05 mm. Similar to CSRG, initially three parameters, the width, w, the depth, h, of each groove, and the distance or gap between two neighboring grooves, g were varying in the simulation study.

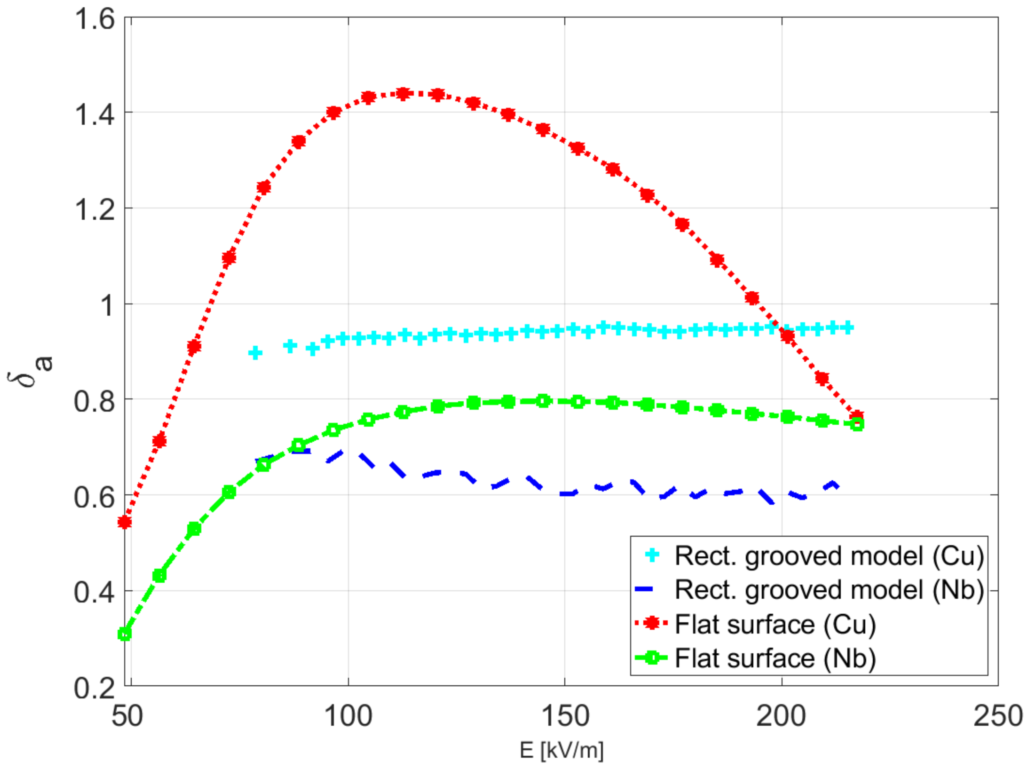

Figure 4.11: Comparison of the δ_a of the CSRG model with that of a flat surface. The CSRG surface reduces the δ_a below unity.

The EM field was computed at 1.3 GHz within the model using the FD solver of CST MWS. Like the above models, the PEC surface and the PMC BC at both ends of the structure were assumed. The two symmetry planes of magnetic walls ($H_t = 0$) were also considered to reduce the size of the computational model. The converged result was obtained for a number of around 750,000 mesh cells (with 65 cells per wave length). The distribution of the electric field in the CSIG surface is illustrated in Figure 4.12. The field intensity is represented with the color distribution. The EM fields were imported into the PIC solver for MP simulation. Again, the fields were scaled in PIC solver based on the actual electric field in the cavity. The PIC simulation was performed for the complete computational model using a total number of around 3 million of HEX mesh cells (with $\mathrm{N}_x = 222$ $\mathrm{N}_y = 117$ $\mathrm{N}_z = 117$).

CSIG and CSSG surfaces with deeper grooves have shown reduced MP in the simulations. The simulations have been performed varying only one geometric parameter at a time while considering other parameters constant. Initially, the MP dependence on the depth h has been studied. In case of the CSIG, the depth h has been varied from 0.2 mm to 0.8 mm while the distance $g = 0.5$ mm and the

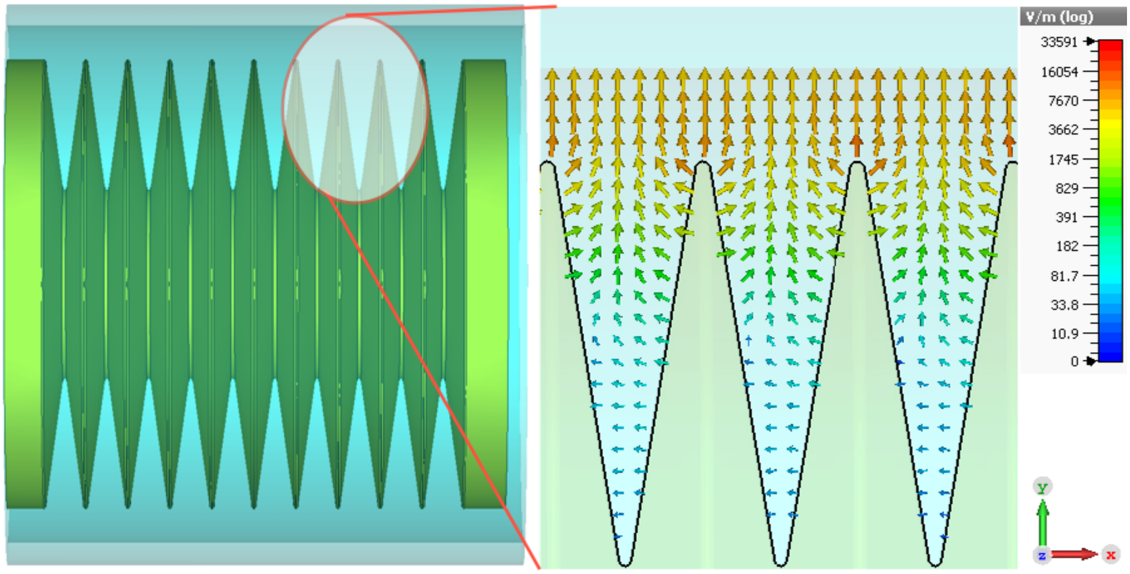

Figure 4.12: Left: The CSIG model with a period of $g + w$, i.e. distance plus width; Right: Electric field distribution inside of a zoom with three CSIG surfaces on the z-cut plane.

width $w = 0.3$ mm were considered constant. The parameters g and w were initially chosen arbitrarily. As shown in Fig.4.13, the grooves with depth $h = 0.4$ mm had a significant impact on MP. Considering the manufacturing costs, the groove with a depth of 0.4 mm is more advantageous compared to the groove with a depth of 0.6 mm as they have approximately similar MP effect. Moreover, it displayed that a groove with smaller h, i.e., 0.2 mm, has a risk of MP occurrence. Except for a depth of $h = 0.2$ mm, similar results were observed in both CSIG and CSSG surfaces as presented in Fig. 4.13. Deep grooves of CSIG and CSSG surfaces disturb the electron trajectories and also attenuate the fields inside the grooves, and therefore, they do not allow the secondary electrons to gain sufficient energy. Thereby the resonant electron production is prevented.

A significant rise in the number of particle with time was observed while varying the width w of the triangular grooves. Now, the depth $h = 0.4$ mm, and the distance $g = 0.2$ mm were kept constant during the simulations. The CSIG surface with wider width does not strongly attenuate the field. It, therefore, allows the secondary electrons to gain sufficient energy, resulting in a raise in particle number over time, as illustrated in Fig. 4.14. Comparatively, grooves with a width w of 0.2 mm have shown less MP in the cathode vicinity. Moreover, wider widths with 0.6 mm and 0.8 mm resulted in a significant rise in particle number over time. This is probably because the electrons could escape easily with sufficient energy from the groove the wider it gets.

Finally, the parameters $h = 0.4$ mm and $w = 0.3$ mm, i.e. the depth and the

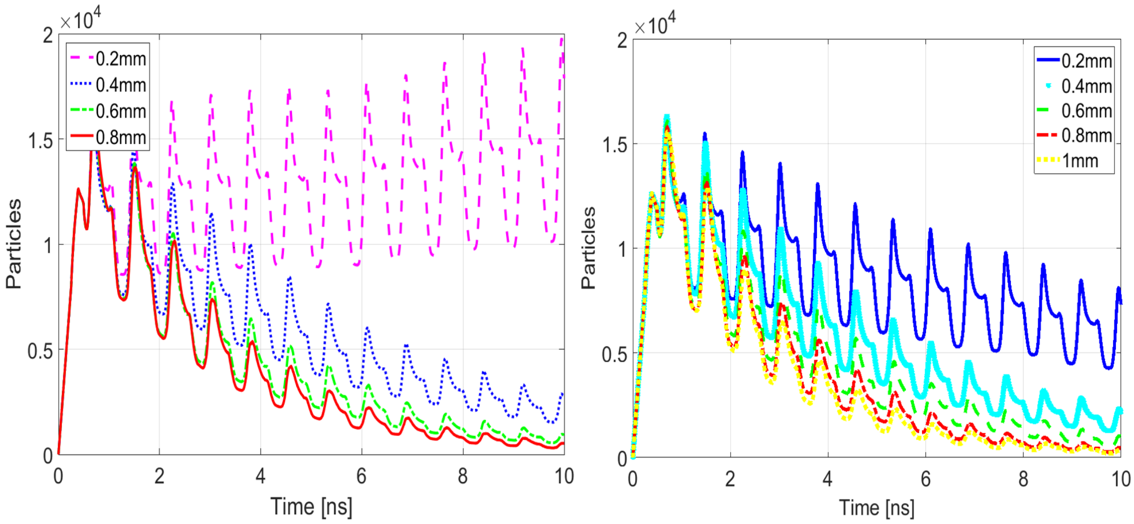

Figure 4.13: Particles vs time graph for varying the depth h of the CSIG (left) and CSSG (right) surfaces.

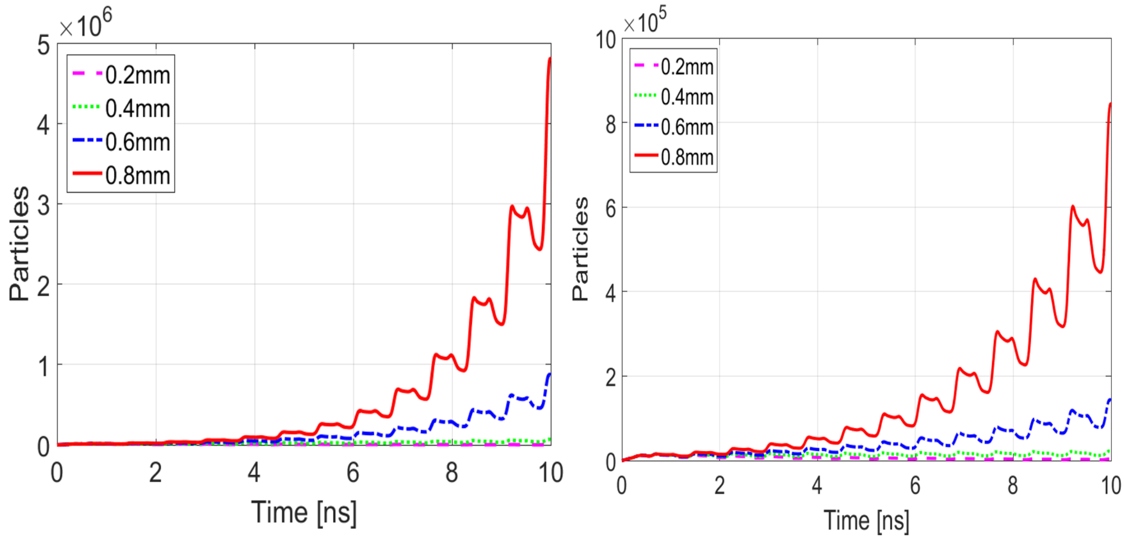

Figure 4.14: Particle vs time graph by varying the parameter w of the CSIG and CSSG surfaces.

width of the triangular grooves, were kept unchanged while varying the distance g for CSIG and CSSG models. In both cases MP could sufficiently be suppressed for all parameter values as illustrated in Fig. 4.15. Therefore, the impact of this parameter was less compared to others as no significant change in the number of particles was observed within the given range.

In conclusion, varying the width w of the CSIG and CSSG surfaces had significant impact on the MP compared to varying the height h and the distance g. As w of the

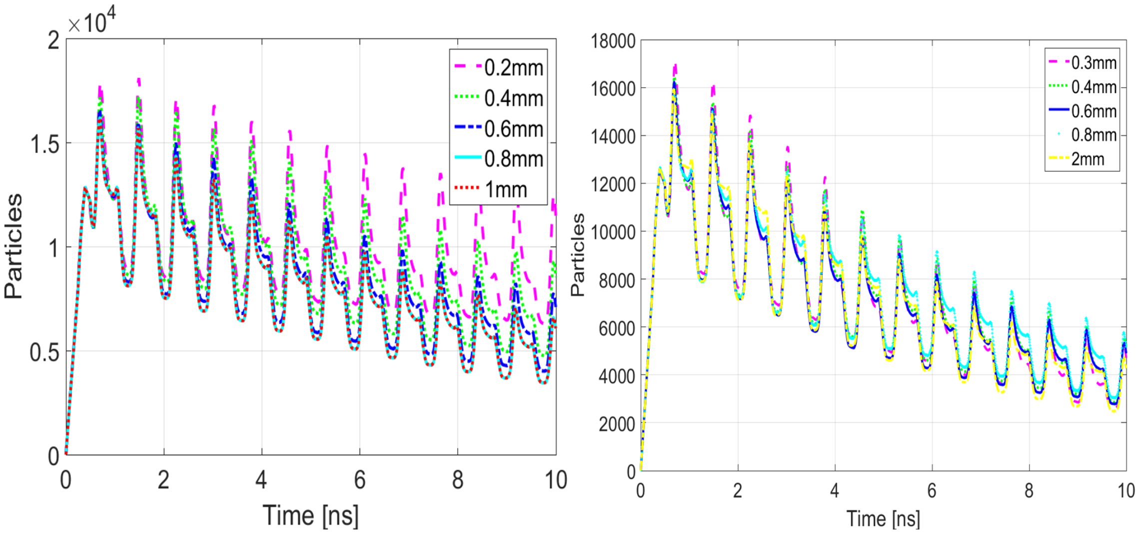

Figure 4.15: Particles vs time graph in case of varying the distance g of the CSIG (left) and CSSG (right) surfaces.

grooves gets wider, the number of secondary particles rises (studied up to 0.8 mm), and MP is observed. Almost similar numerical results were observed for both kind of surfaces in all parametric studies. Therefore, as manufacturing the CSSG surface requires more effort than the CSIG, a further study was carried out concentrating only on the CSIG model.

For the automated optimization, besides the width w, the effect of the angle α or the grazing angle θ_g was studied as well, as previous investigations showed that the δ_a is sensitive to the angle α [70],[102]. Therefore, in the present study, the two main parameters, such as the width w and the angle α were considered. The optimization procedure and some results are presented in Appendix D. The optimum parameters for the CSIG are a grazing of $\theta_g = 88.8°$ or angle $\alpha = 45.6°$ and a width of $w = 0.293$ mm. The model reduces the peak of δ_a for Cu and Nb to 0.897 and 0.301, respectively, at 112.6 kV/m, where the maximum generation of secondaries was observed within the flat gap. The corresponding average impact energies are 15.60 and 28.54 eV for both Cu and Nb, which are lower than the first crossover energies (U_{c1}) of 27.3 eV for Cu and 76 eV for Nb, respectively. Next, to obtain the field level with respect to δ_a for the CSIG surface, a parameter sweep of the electric field amplitude was performed from 78.62 kV/m to 212.27 kV/m. As Fig. 4.16 depicts, all values of the calculated δ_a for Cu and Nb within this amplitude range of the electric field are below the threshold, which is unity. Therefore, MP is totally suppressed in the region. The δ_a curves for a flat surface (Model C) are shown in the same figure as a reference.

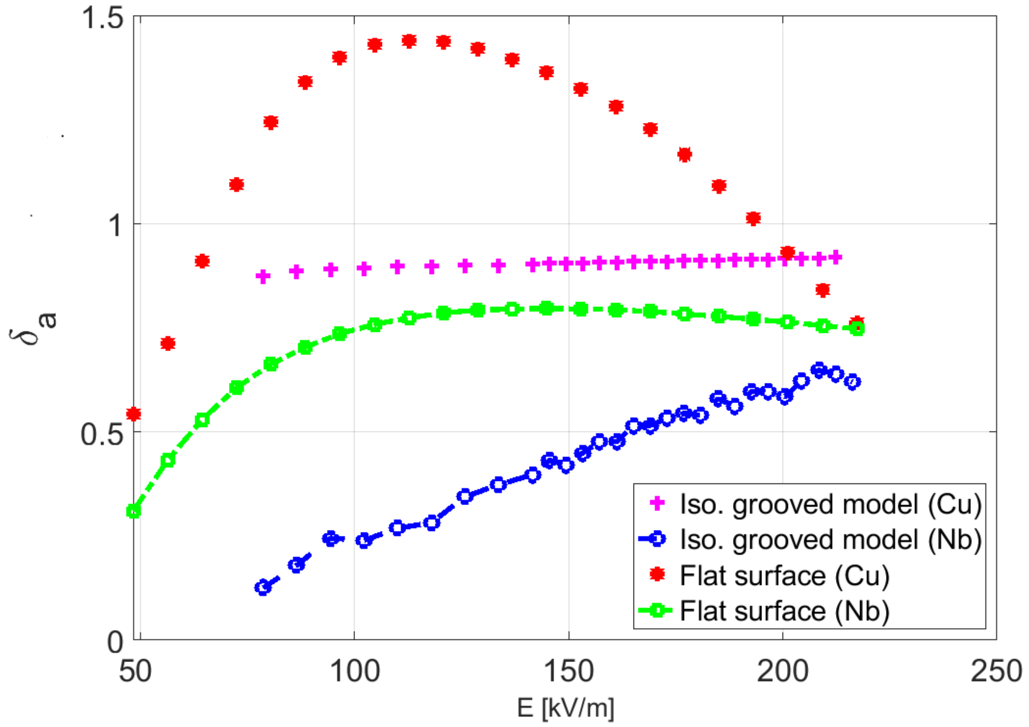

Figure 4.16: Comparison of the CSIG model with a flat surface with respect to MP in terms of δ_a. The isosceles surface reduces the δ_a below the threshold.

4.4 Anti-Multipactor Layer

Anothr candidate for the mitigation of multipactor discharge, namely anti-Multipactor layer or thin-film coating, was also studied. Coating various thin films with a low SEY can reduce the secondary electron emission and MP effects, as the SEY function is mainly considered to be influenced by the uppermost material layer from 3 to 5 nm [101]. The present work was conducted in collaboration with the University of Siegen. The SEY experimental platform was set up at the University of Siegen based on the designs from CERN. The experimental setup and the principle of the measurement on SEY are presented in [113]. The SEY measurements for various materials, such as Titanium Nitride (TiN) and Carbon (C), Molybdenum (Mo), Copper (Cu), and Niobium (Nb) with different samples were carried out by our partner Dr. Christoph Schlemper and Dr.-Ing. Michael Vogel from the Chair of Surface and Materials Technology of Prof. Dr. Xin Jiang, Institute of Materials Engineering at University of Siegen within the framework of the BMBF-funded joint project 05K2013- HOPE: High brilliance photoinduced radio frequency electron sources. Quasi in-situ measurements were utilized to evaluate SEY. DC and RF magnetron sputtering were implemented for the deposition of thin films. The films were deposited on substrates, namely Copper (Cu), Molybdenum (Mo), and Silicon (Si), with a thickness of 400 to 600 nm. The experimental studies on SEY for various substrate materials, such as Cu, Nb, Mo, and the two film materials C and TiN, were discussed in [113],[150]. The effect of the surface conditions, various cleaning processes, and coating methods concerning SEY values were considered in these papers.

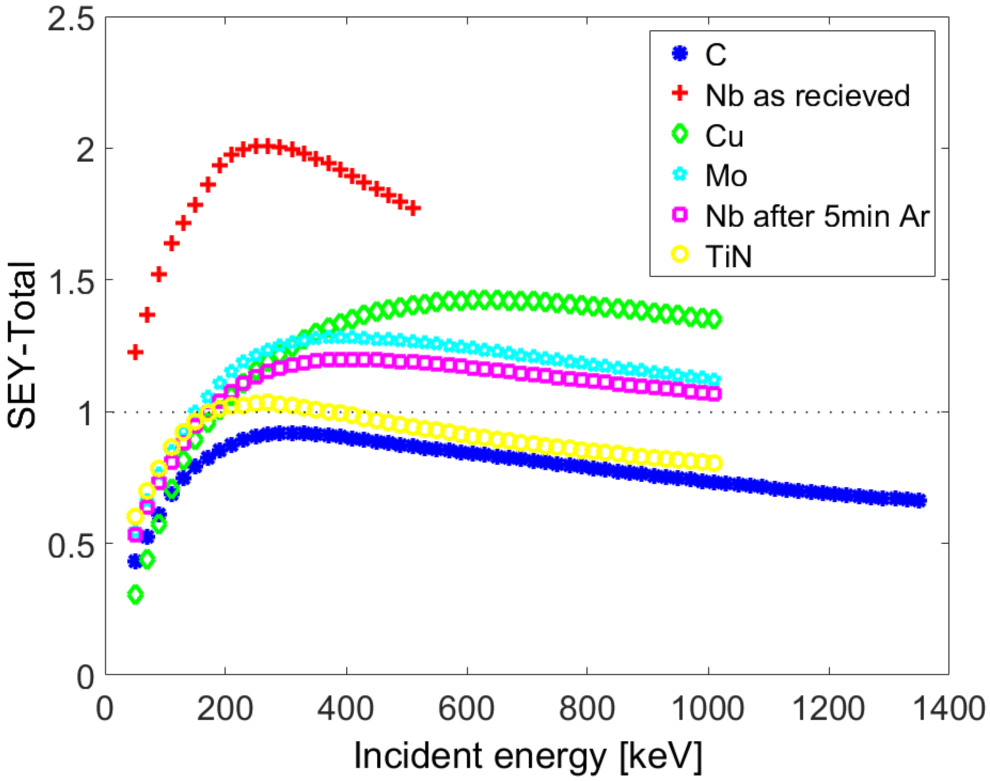

Figure 4.17: The measurement data of SEY for various materials obtained from our partners at the University of Siegen.

The comparison of the SEY-measurements on different materials shown in Fig. 4.17 reveals that coating TiN and C are found to be promising in terms of avoiding MP by lowering the SEY value. The SEY values of other materials used as a substrate are also presented in the same graph. These experimental results demonstrate that the SEY value of ~0.8 and ~1.0 can be achieved by using optimized C and TiN films, respectively.

In this work, based on the measurement data of SEY, the δ_a as a function of field levels were evaluated. The numerical studies were carried out using our computational model (Model C) (see Fig. 3.2). However, the computational model was constructed from a C cathode stem and a Nb pipe, as the C coatings are the best method

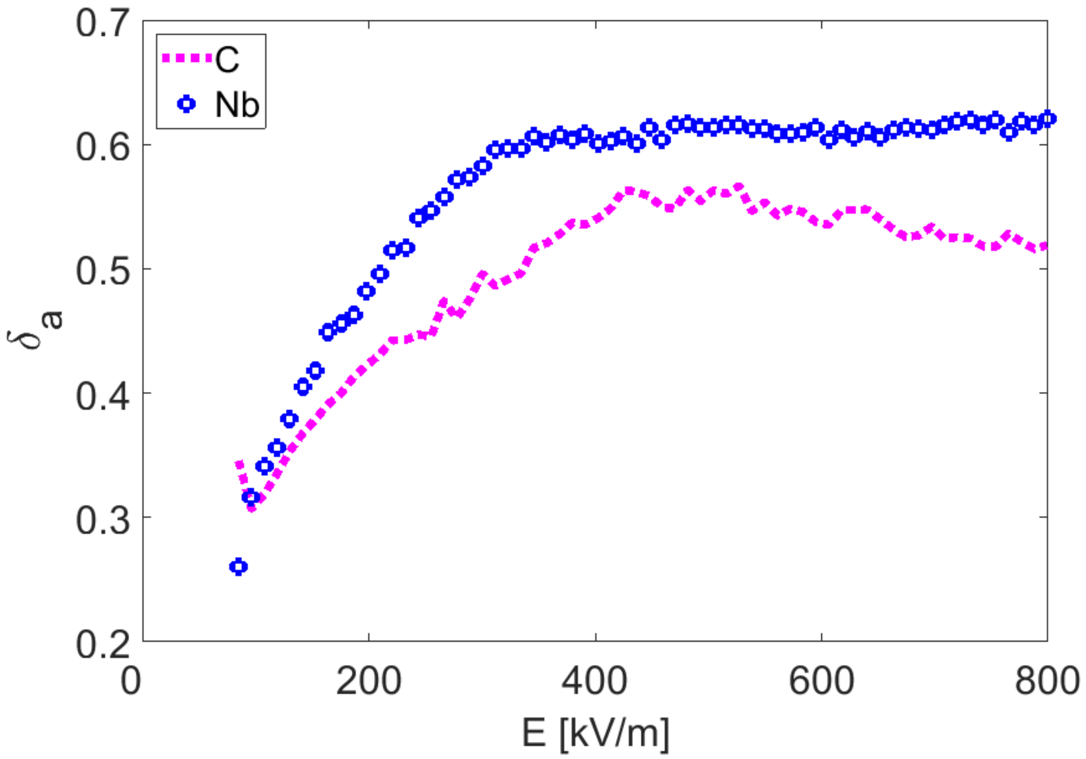

Figure 4.18: The numerical results for the δ_a of C and Nb as a function of electric field.

to achieve low SEY comparing to TiN, as noted above. The EM field was then calculated using the FD solver of CST PS. Similar to the above-simulated model, the port and the BCs were set, as illustrated in Fig. 3.13. The same mesh settings used there (in Section 3.2.1) were also considered for this simulation. The EM field was then imported into the PIC solver as a base of MP simulation.

For the MP calculation, all the initial conditions and set up of the seed electrons were assumed as presented in Table 3.1. The secondary emission was governed by the imported SEY function of C and Nb. The material properties, such as the EM properties and the thermal properties, of C and Nb, were defined according to the data in the CST's material library. Then the δ_a for the inner and outer surfaces were calculated separately. This calculation was done in the range of 85 to 175 kV/m of the gap electric field levels. As evidenced by the illustration in Fig. 4.18, the δ_a values are far below one in the case of all field levels for both surfaces. The peak δ_a values for C and Nb of 0.57 and 0.62 were obtained at 527.0 kV/m and 481.7 kV/m, respectively. These values corresponded to the impact energy of 92.79 eV and 84.42 eV. These numerical studies confirm that the C coatings method is a good candidate, as proposed in [113],[150], to avoid MP as the SEY values are below one in all field levels.

5 Uncertainty Quantification and Sensitivity Analysis in Multipactor Threshold

One of the main parameters for MP calculation is the SEY function, as discussed in previous chapters. In practice, any contamination and air exposure can cause an increase of the SEY values of the materials used in particle accelerators, for example, adsorption of oxygen on the Cu surface [146],[101]. The MP threshold is highly determined by the presence of uncertainty in the SEY. Thus the study on the impact of the variation of the SEY function in terms of the MP threshold is crucial. Therefore, based on the result from the suppression of multipactor methods discussed in Chapter 4, the robustness of the proposed models, namely CSRG and CSIG, was examined through uncertainty quantification (UQ) and global sensitivity analysis (GSA). The UQ [132] was carried out to appraise and quantify the impact of the SEY uncertainty for newly designed and optimized models of the cathode vicinity. For this purpose, we applied the advanced tools, i.e. the generalized polynomial chaos expansion (gPCE), to quantify the effect of uncertainty and to assess to which extent the achieved results of the models can be affected by changing the values of the SEY. Moreover, the systematic investigation of the SA [110] was performed to identify the key parameters of SEY curves that influence the uncertainty of the model output (δ_a) the most. Among various SA approaches, the Sobol sensitivity indices (SSI) [124],[125], which are considered as the most accurate sensitivity measure, based on generalized polynomial chaos (gPC) were applied.

5.1 Sobol' Decomposition

Assuming a computational model $\mathcal{F}$ represents the behavior of the considered physical system and the N probabilistic model parameters X_N, the computational model can then be written as $Y = \mathcal{F}(X_1, X_2, ..X_N)$. The main approach of Sobol to define the SSIs is the decomposition of the mathematical model $Y = \mathcal{F}(X)$ into summands of different dimensions. Assuming ξ_i is the independent random input variable, the Sobol or ANOVA (ANalysis Of VAriance) decomposition of the stochastic output $Y = \mathcal{F}(\xi_1 ... \xi_N)$ is [124], [125]

$$\mathcal{F}(\xi) = f_0(\xi) + \sum_{1 \le i \le N} f_i(\xi_i) + \sum_{1 \le i < j \le N} f_{ij}((\xi_i), (\xi_j)) + ... + f_{1...N}(\xi_1, ..., \xi_N), \quad (5.1)$$

where the first term of the decomposition is a constant representing the mean value of the function

$$f_0(\xi) = \mathbb{E}\big[f(\xi)\big] \tag{5.2}$$

and the Sobol' decomposition of $\mathcal{F}(\xi)$ is unique if the other terms are orthogonal to each other

$$\int_{\Omega^N} f_{i_1,\ldots i_s}(\xi_{i_1}\ldots,\xi_{i_s}) f_{j_1,\ldots j_s}(\xi_{j_1}\ldots,\xi_{j_s}) d\xi_1,\ldots d\xi_N = 0, \qquad \text{if } \big\{i_1,\ldots,i_s\big\} \neq \big\{j_1,\ldots,j_s\big\}, \tag{5.3}$$

due to the orthogonality properties, by using Eq. 5.1 and Eq. 5.3, the total variance V of Y can be decomposed as follows

$$V = \int_{\Omega^N} f^2(\xi)d\xi - f_0^2(\xi) \ = \sum_{1\leq i\leq N} V_i + \sum_{1\leq i<j\leq N} V_{ij} + \ldots + V_{1,\ldots,N}, \tag{5.4}$$

where the partial or conditional variances $V_{i,\ldots,j}$ can be defined as

$$V_{i,\ldots,j} = \int \ldots \int f^2_{i,\ldots,j}(\xi_i,\ldots,\xi_j)d\xi_i,\ldots\xi_j, \qquad 1 \leq i \text{ and } j \leq N \tag{5.5}$$

The Sobol' sensitivity indices can be defined as the ratio of the partial variances to the total variance [125]

$$S_{i_1,\ldots,i_s} = \frac{V_{i_1,\ldots,i_s}}{V}, \qquad \{i_1,\ldots,i_s\} \subset \{1,\ldots,N\}, \tag{5.6}$$

that measures the amount of the total variance caused by the interaction between the uncertain input variables. The influence of the individual random input variables can be obtained by computing the first order indices S_i, whereas the higher order indices explain the effect of their interaction to the model output and their sum can be written as [130]

$$\sum_{i=1}^{N} S_i + \sum_{1\leq i<j\leq N} S_{ij} + \ldots + S_{1,\ldots,N} = 1. \tag{5.7}$$

One example of the statistical approaches to evaluate the SSI is the Monte-Carlo method. The method requires $O(n^2)$ evaluations for n sample sets of input variables for sufficient accuracy, which typically necessitates thousands of model evaluations [164]. Additionally, a simplified Monte-Carlo sampling method requires $O(n2^N)$ evaluations of all indices in Eq. 5.7. This indicates that the cost grows exponentially with the number of input variables, N. Hence, this makes the method computationally very demanding.

The other technique is the polynomial chaos (PC) method for UQ as well as SA. The idea was originally introduced by Wiener [158], where the mathematical model is represented by stochastic PDE and the solution can be found using deterministic sampling methods. The classical approach of this method, which was first described by Ghanem and Spanos [47], is extended to the so-called generalized polynomial chaos (gPC) method [164]. The gPC uses the special class of orthogonal polynomial basis functions called polynomial chaos expansion (PCE) for the model solution to construct the surrogate model. The first step to determine the PCE is computing the coefficients, which will be explained in the following sections. The main advantage of using this method in GSA is once the coefficients are obtained in the intermediate computation, the solution for first and higher-order indices follows by simple analytical formulae [130]. The computational cost is reduced significantly compared to Monte-Carlo methods. In the present work, due to its computational efficiency, a gPC approach was applied to investigate the propagation of uncertainty in the SEY on the model output and to compute all the Sobol' indices (stated in Eq. 5.7).

5.2 Polynomial Chaos Expansion

A uniform distribution for input parameters is considered in $\sim U(a, b)$. The model output of the stochastic process Y can also be represented by a series of multivariate orthogonal basis functions Ψ_i based on gPC expansion [164],[47] as

$$Y = \sum_{i \in \mathbb{N}^N} c_i \Psi_i(\xi). \tag{5.8}$$

c_i are the PC coefficients of the expansion of the random variable Y and ξ are independent and uniformly distributed random variables in $U[a, b]$. For practical application, the infinite basis function in Eq. 5.8 can be truncated to a limited number of basis polynomials M. The optimal choice for uniformly distributed model parameters is the orthogonal multi-variate Legendre polynomial, which is one of the

Distribution	Polynomials	PDF	Weight Function	Support Range
Gaussian	Hermite	$\frac{1}{\sqrt{2\pi}}e^{\frac{-x^2}{2}}$	$e^{\frac{-x^2}{2}}$	$[-\infty, \infty]$
Uniform	Legendre	$\frac{1}{2}$	1	$[-1, 1]$
Beta	Jacobi	$\frac{(1-x)^a(1+x)^b}{2^{a+b+1}\beta(a+1,b+1)}$	$(1-x)^a(1+x)^b$	$[-1, 1]$
Exponential	Laguerre	e^{-x}	e^{-x}	$[0, -\infty]$
Gamma	Generalized Laguerre	$\frac{x^a e^{-x}}{\Gamma(a+1)}$	$x^a e^{-x}$	$[0, -\infty]$

Table 5.1: Famillies of orthogonal polynomials with various standard continuous PDFs and the corresponding weighting functions with their support range. Table taken from [36].

common orthogonal polynomials families shown in Table 5.1. Then the quantity of interest Y can be approximated using a series expansion of $M-1$ with N independent uniformly distributed random variables:

$$Y \approx \hat{Y} = \sum_{i=0}^{M-1} c_i \Psi_i(\xi), \qquad \xi \sim U[-1,1]^N. \tag{5.9}$$

The multi-variate Legendre polynomials $\Psi_i(\xi)$ can be determined by the product of uni-variate polynomials $L_{\alpha i}(\xi_i)$, where each multi-variate basis Legendre polynomial represented by a multi-index $\alpha = (\alpha_1, ..., \alpha_N)$, [164]:

$$\Psi_\alpha(\xi) = \prod_{i=1}^{N} L_{\alpha_i}(\xi_i), \qquad \alpha \in \mathcal{I}_{N,p}, \;\; \mathcal{I}_{N,p} = \{\alpha = (\alpha_1, ..., \alpha_N) \in \mathbb{N}_0^N : \|\alpha\|_1 \leq p\}, \tag{5.10}$$

where $\|\alpha\|_1$ is the 1-norm of the multi-index α, i.e., $\|.\|_1 = \alpha_1 + ... + \alpha_N$, p is the order of expansion and ξ_i are mutually independent N-dimensional random variables. In such a case, the total number of basis polynomials M can be determined by the order of the gPCE p for N uncertain input variables [164]:

$$M = \sum_{i=0}^{p} \binom{N+i-1}{i} = \frac{(p+N)!}{p!N!}. \tag{5.11}$$

Usually, the higher the order of PC basis functions, the more accurate representation can be found. However, the higher number of unknown coefficients with a larger number of stochastic dimensions need to be solved. A detailed mathematical description of the gPC approach can be found in [164].

The determination of c_α in the expansion of $\hat{Y}$ enables us to characterize the uncertainty and to evaluate the SSI directly. Among others, the projection approach of a non-intrusive PCE method allows determining the c_α by projecting the expansion of $\hat{Y}$ on each basis polynomial [131], [36]. This approach then uses the following relations from the orthogonality of the PC basis to estimate the coefficients c_α

$$c_\alpha = \frac{1}{\langle \Psi_\alpha(\xi), \Psi_\alpha(\xi) \rangle} \langle \hat{Y}(\xi), \Psi_\alpha(\xi) \rangle, \tag{5.12}$$

where $\langle ., . \rangle$ denotes the inner product. The evaluation of $\langle \psi_\alpha(\xi), \Psi_\alpha(\xi) \rangle$ is known exactly based on the orthogonal relation of the Legendre polynomial. By using the definition of the inner product, the nominator in Eq. 5.12 reads

$$\langle \hat{Y}(\xi), \Psi_\alpha(\xi) \rangle = \int_I \hat{Y}(\xi) \Psi_\alpha(\xi) w(\xi) d\xi, \tag{5.13}$$

then Eq. 5.12 can be rewritten as

$$c_\alpha = \frac{1}{\langle \Psi_\alpha(\xi), \Psi_\alpha(\xi) \rangle} \int_I \hat{Y}(\xi) \Psi_\alpha(\xi) w(\xi) d\xi, \tag{5.14}$$

where I is the domain $([a, b]^N)$ of ξ with the probability measure of the associated weighting function $w(\xi)$, which is one in case of Legendre polynomial as noted in Table 5.1. The integrals in Eq. 5.14 can not be integrated analytically. Thus the numerical integration should be applied, which requires the evaluation of the deterministic model at each quadrature node. One approach to compute the integrals numerically is a multi-dimensional cubature based on tensor and sparse grids using Smolyak algorithm [115],[114]. The latter grids were used for our numerical calculation as it is computationally efficient. The method is described in detail in [114] as it was successfully implemented in our working group using the MATLAB® library called QUNIPALM[1]. This code was initially used for bio-electrical engineering problems in our research group for the investigation of human brain models [114]. Then it has been employed for the applications of accelerator physics, some works can be found in [57], [116] [58]. This technique was also adapted and implemented in the present work.

Similar to Eq. 5.1, the decomposition of the PCE of $\hat{Y}$ for the term $M-1$ can be rewritten as [130],[85]

$$\begin{aligned} \hat{Y} = c_0 + \sum_{i=1}^{N} \sum_{\alpha \in \mathcal{I}_{1,p}} c_\alpha \Psi_\alpha(\xi_i) + \sum_{1 \le i < j \le N} \sum_{\alpha \in \mathcal{I}_{2,p}} c_\alpha \Psi_\alpha(\xi_{\alpha_i}, \xi_{\alpha_j}) \\ +, ..., + \sum_{\alpha \in \mathcal{I}_{1,2,...,N,p}} c_\alpha \Psi_\alpha(\xi_1, ..., \xi_N). \end{aligned} \tag{5.15}$$

Once the PCE coefficients are computed, the probability density function (PDF) as well as the stochastic moments of the figures of merit, such as the mean μ and the standard deviation σ, of $\hat{Y}$ can be determined. The first coefficient of the gPCE in Eq. 5.15 is equal to the mean value μ of the Quantities of Interest. The μ and σ of $\hat{Y}$ then reads [130]:

$$\mu = \mathbb{E}\big[\hat{Y}\big] = c_0, \tag{5.16}$$

and

$$\sigma^2[\hat{Y}] = V\big[\hat{Y}\big] = \sum_{\alpha \in \mathcal{I}_{N,p}} c_\alpha^2, \tag{5.17}$$

respectively.

5.2.1 Generalized Polynomial Chaos based Sobol' indices

The gPC based calculation of SSI was initially described by Sudret [131],[130]. The mathematical expression of the gPC based SSI can directly be driven from the gPC expansions in Eq. 5.15. Due to the orthoganality of the bases functions, the first

---

[1] QUNIPALM stands for Quantifying Uncertainties using a Non-Intrusive Projection Approach Library for Matlab.

and the higher order of the gPC-based SSI can be evaluated from the cofficients as follows [51]:

$$S_i = \frac{\sum_{\alpha \in \mathcal{A}_i} c_\alpha^2}{\sum_{\alpha \in \mathcal{A}} c_\alpha^2}, \qquad \mathcal{A}_i = \alpha \in \mathcal{A} : \alpha_i > 0, \alpha_{i \neq j} = 0 \tag{5.18}$$

and in a similar manner the total SSI can be estimated by

$$S_i^T = \frac{\sum_{\alpha \in \mathcal{A}_i^T} c_\alpha^2}{\sum_{\alpha \in \mathcal{A}_i^T} c_\alpha^2}, \quad \mathcal{A}^T = \alpha \in \mathbb{N}^N : \alpha_i > 0. \tag{5.19}$$

5.3 Uncertainty Quantification and Sensitivity Analysis for the Grooved Models

The aim of this investigation is to apply the gPC-based method for UQ and SA for the optimized grooved models. Figure 5.1 depicts the grooved geometries, namely the CSRG and CSIG, considered for the computations. The models are discussed in detail in Chapter 4. The inner and outer surfaces are made of the Cu and Nb materials, respectively. In this work, in order to calculate the MP threshold, the SEY curves modeled by Furman and Pivi for Cu and Nb materials were considered. The SEY is a function of the impact energy (U_i) of the incident electron and its incident angle (θ_0). As illustrated in Fig. 3.5, the peak SEY, $\hat{\delta}$, of Cu is 2.1 at 250 eV of corresponding impact energy, $\hat{U}$. Similarly, the $\hat{\delta}$ of Nb is 1.49 at 300 eV of $\hat{U}$, for perpendicular incidence. In the present study, our focus is on the SEY of the Cu surface (depicted in Fig. 5.2). This curve exhibits the key parameters, i.e., a peak SEY ($\hat{\delta}$) with energy at peak yield ($\hat{U}$), where the highest generation of secondary electrons is expected as discussed in detail in Chapter 2. The parameters $\hat{\delta}$ and $\hat{U}$ were therefore chosen to be uncertain to investigate the effect of the uncertainty in the SEY on the multipactor threshold in case of CSRG and CSIG surfaces. These uncertain parameters were assumed to be uniformly distributed random variables with mean values μ of 2.1 and 250, respectively. The impact of the individual and the collective contribution of each parameter was studied by evaluating the SSI.

In this work, the multipactor threshold characterized by the average SEY denoted as δ_a of the model' output is of interest. To quantify the uncertainty for the δ_a with respect to the uncertain SEY model, a uni-variate and a multi-variate gPCE based on the deviation of $\hat{\delta}$ and $\hat{U}$, were carried out. For this purpose, the repeated computation of the PIC solver in combination with the gPC technique was conducted using the PIC solver of CST PS as well as QUNIPALM. Additionally, in order to integrate the QUNIPALM into our computational models, the VBA[2] script, which is an extension for the source code of CST PS, was required. Along with the VBA script, the MATLAB function was used to call the CST PS macro and to control

---

[2] VBA stands for Visual Basic for Applications

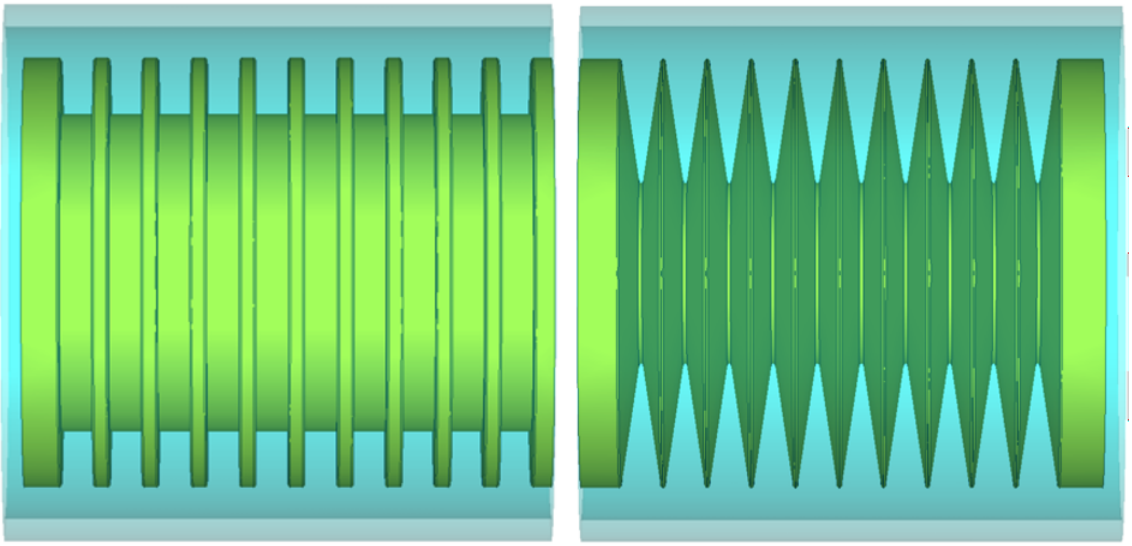

Figure 5.1: The optimized geometries of CSRG (left) and CSIG (right) modeled by CST MWS.

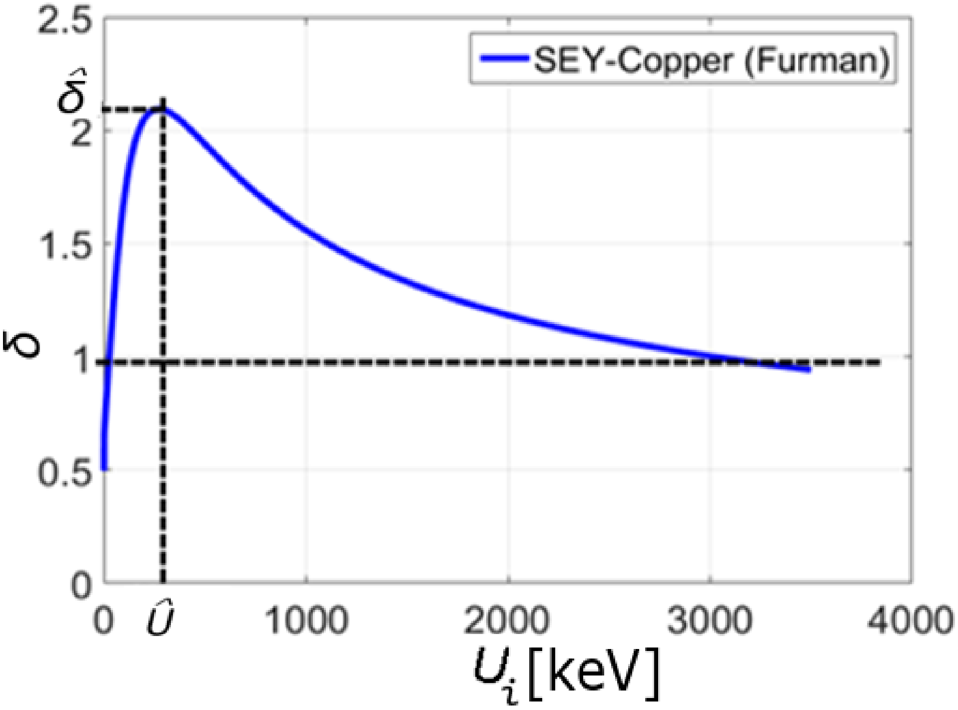

Figure 5.2: The total SEY as a function of incident energy U_i at zero incident angle for Cu. The peak SEY, $\hat{\delta}$, of Cu is 2.1 at the energy $\hat{U}$ of 250 eV.

the input/output parameters of the simulation model for the repeated computation of the PIC solver of CST PS.

5.3.1 Uncertainty Quantification for CSRG Model

As a result of the UQ in case of CSRG, the uncertainty for δ_a with respect to the parameters of the SEY model was investigated considering the variation of the following three cases: 1) $\hat{\delta}$; 2) $\hat{U}$; 3) $\hat{\delta}$ and $\hat{U}$. In the first case of a univariate study, 10^6 uniformly distributed random variable samples of $\hat{\delta}$ were modeled considering a mean value μ of 2.1 with relative standard deviations σ_r up to 35 %. The summary of the probabilistic model parameters of $\hat{\delta}$ in $U[a, b]$ is given in Table 5.2.

σ_r [%]	lower boundary (a)	upper boundary (b)	mean (μ)
5	1.995	2.197	2.1
10	1.890	2.294	2.1
15	1.785	2.391	2.1
20	1.680	2.488	2.1
25	1.575	2.585	2.1
30	1.470	2.682	2.1
35	1.365	2.779	2.1

Table 5.2: Probabilistic model parameters of $\hat{\delta}$ in $U[a, b]$.

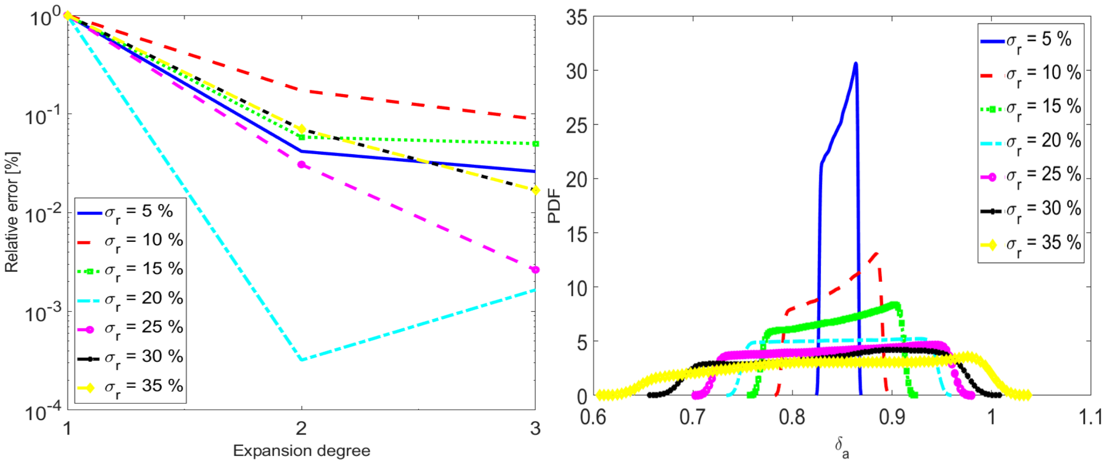

Figure 5.3: Left: Relative error of the variance of the RMS value for the gPCE degree p of upto 3 in case of a relative standard deviation of σ_r of 5 %, 10 %, 15 %, 20 %, 25 %, 30 % and 35 % in the peak yield $\hat{\delta}$; right: PDFs of δ_a obtained via third-order uni-variate gPCE.

For each deviation of the probabilistic model $\hat{\hat{\delta}}$, the CST PIC simulations were carried out. All the parameter setups were similar to the numerical simulations of MP described in Section 4.3.2 and Section 4.3.3. The resulting δ_a was approximated by a truncated series of random polynomials. The accuracy of this approximation was controlled by computing the relative error of the variance of the root mean square (RMS) value of δ_a for a uni-variate gPCE degree p of up to 3. The number of polynomials can be determined according to Eq. 5.11 in each case of polynomial degree for the random variable of $\hat{\hat{\delta}}$. Fig. 5.3 (left) shows the convergence of the variance of the RMS value of the coefficients in case of σ_r of 5 %, 10 %, 15 %, 20 %, 25 %, 30 % and 35 % for the CSRG model. A well-decreased convergence rate was observed in all cases as the values of the relative errors were below 0.1 %. For these deviations on $\hat{\hat{\delta}}$, the probabilistic density functions of δ_a were computed. The non-intrusive projection approach for a degree p of 3 of the uni-variate polynomial basis was employed based on 10^6 uniformly distributed random variable samples of $\hat{\hat{\delta}}$. The latter choice was fixed throughout the present studies. Figure 5.3 (right) illustrates that the asymmetric behavior of the *unimodal* PDF of δ_a in the case of 5 %, 10 % and 15 % of σ_r in $\hat{\hat{\delta}}$ and rather symmetric for the remaining values of σ_r up to 35 %. The larger δ_a is more probable than the smaller one compared to the mean. The deviations σ_r in $\hat{\hat{\delta}}$ up to 25 % ensure that all the values of δ_a were below unity. The value of δ_a slowly start to exceed unity as from 30 % of σ_r. The CPU time required for each PIC simulation of MP (within 10 ns) and the gPC recomputation of the CSRG model solution for each sample case is approximately 90 minutes. For example, the total time required for the UQ results achieved only in case of $\sigma_r =$ 5 % at the polynomial degree of $p = 3$ is approximately 13.5 hours using a powerful computer (Intel(R)CPU E5 with 3.30 GHz and 256 GB).

For the second case of a univariate study, the propagation of the uncertain parameter energy $\hat{U}$ in the multipactor threshold for the CSRG model was investigated. Uniformly distributed random variable samples of $\hat{U}$ were modeled considering a mean value of μ of 250 for σ_r up to 45 %. In Table 5.3 the probabilistic model parameters of $\hat{U}$ in $U[a, b]$ are shown. The quantitative representation of the gPCE

σ_r [%]	lower boundary (a)	upper boundary (b)	mean (μ)
5	237.50	261.55	250
10	225.00	273.10	250
15	212.50	284.65	250
20	200.00	296.19	250
25	187.50	307.74	250
30	175.00	319.29	250
35	162.50	330.84	250

Table 5.3: Probabilistic model parameters of $\hat{U}$ in $U[a, b]$.

accuracy for the approximation of δ_a was computed using the relative error of the variance of the RMS value of δ_a. The results were approximated with orders of the gPCE p up to 3. Fig. 5.4 (left) shows the convergence of the variance of the RMS value of the coefficients in case of σ_r of 5 %, 10 %, 15 %, 20 %, 25 %, 30 %, 35 % and 40 % for the CSRG model. In all cases, the values of the relative errors are below 0.1 %. Similar to the previous case, the PDFs of the model output δ_a were evaluated by gPCE for a degree p up to 3 based on random variable samples of $\hat{U}$. Figure 5.4 (right) shows the predicted PDFs of third-order gPCE up to 45 % of σ_r of $\hat{U}$. The probabilistic distribution for all cases of deviations of the input parameter indicated only a very slight asymmetric behavior except for 20 % of σ_r. However, in the latter case the relative error has been reduced for p = 3 with respect to p = 2. More importantly, the larger δ_a is more probable than the smaller one compared to the mean. The deviations σ_r in $\hat{U}$ up to 40 % ensure that all the values of δ_a are below unity. The δ_a slowly start to exceed unity for 45 % of σ_r.

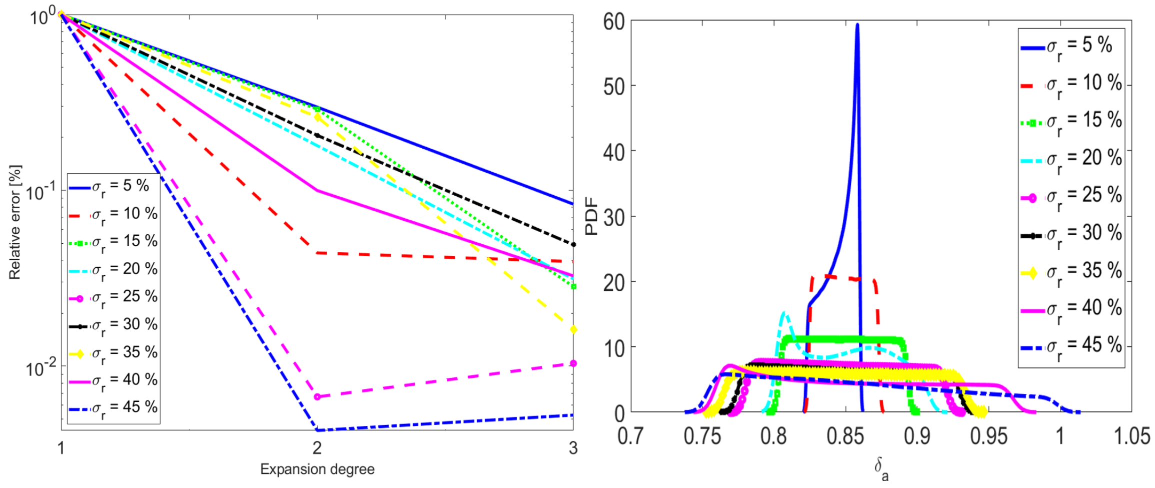

Figure 5.4: Left: Relative error of the variance of the RMS value for the gPCE degree p of upto 3 in case of a relative standard deviation of σ_r of 5 %, 10 %, 15 %, 20 %, 25 %, 30 % and 35 % in energy at peak yield $\hat{U}$; right: PDFs of δ_a evaluated via third-order uni-variate gPCE for the variability of $\hat{U}$.

Lastly, the two-variate studies for the CSRG model were performed using gPC with a polynomial order of $p = 4$. The model was computed for both uncertain input parameters $\hat{\delta}$ and $\hat{U}$ with different relative standard deviations up to 25 % for the mean values 2.1 and 250, respectively. These two uncertain parameters led to two stochastic dimensions with the total number of basis polynomials of $M = 65$ for the order of $p = 4$. The relative errors of the variance of the RMS value of δ_a were computed in case of σ_r of 5 %, 10 %, 15 %, 20 %, 25 % as illustrated in Fig. 5.5 (left). The results were approximated for orders of gPCE p up to 3. For each study case, a good convergence of the variance was obtained with the relative error below

0.1 %. The PDFs of δ_a shown in Fig. 5.5 (right) were obtained for the parameters

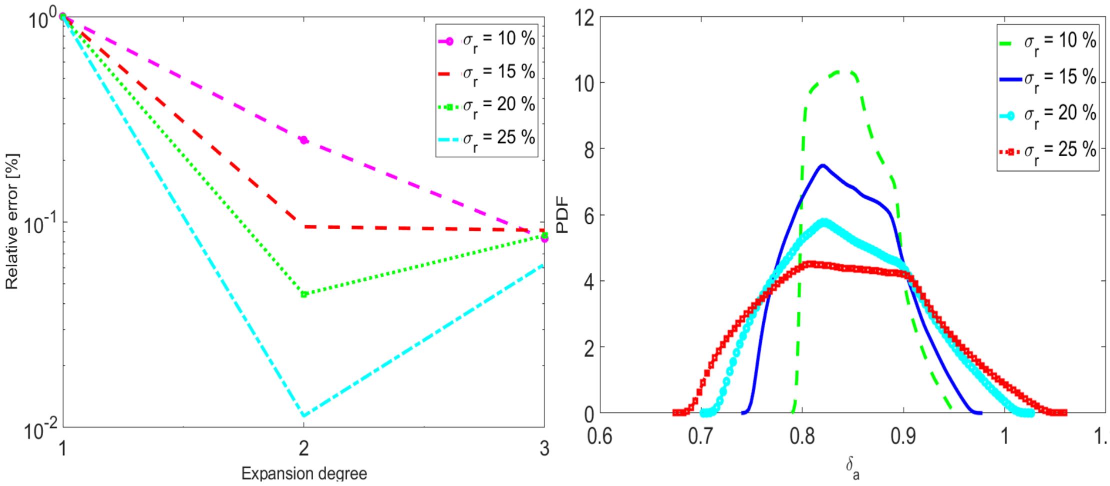

Figure 5.5: Left: Relative error of the variance of the RMS value for the multi-variate gPCE degree p of up to 4 in case of a relative standard deviation of σ_r of 5 %, 10 %, 15 %, 20 %, 25 % in $\hat{\delta}$ and $\hat{U}$; right: PDFs of δ_a evaluated via third-order uni-variate gPCE for the variability of uncertain parameters $\hat{\delta}$ and $\hat{U}$.

$\hat{\delta}$ and $\hat{U}$ with uncertainties of 5 %, 10 %, 15 %, 20 %, 25 %. The results were computed for the 3^{rd} order gPCE. From the figures, a slightly asymmetric behavior of the PDF of δ_a is observable for the first three cases of deviations of the variables, whereas a rather symmetric density results for the relative standard deviation σ_r of 25 %. The results show that up to the relative standard deviations of σ_r 15 % in both uncertain variables $\hat{\delta}$ and $\hat{U}$, the δ_a is less than unity. The results achieved from the uni-variate and multi-variate computations lead to the conclusion that smaller deviations in the uncertain parameters, i.e., 20 %, were required to cross the multipactor threshold in the multi-variate case compared to that of the uni-variate cases. Regarding the uni-variate cases, the magnitudes of 30 % and 45 % of the uncertainties of the parameters in $\hat{\delta}$ and $\hat{U}$, respectively, depicted (see in Fig. 5.4 and in Fig. 5.3) almost similar results in terms of multipactor threshold compared to the results evaluated from the parameter uncertainty of 20 % for the multi-variate case.

5.3.2 Computation of gPCE-based Sobol Indices for CSRG

As noted before, the SSI based on gPCE was computed to assess which input variables have the highest influence on the quantity of interest based on the deviations in the uncertain input parameters. One of the benefits of using the gPCE method for SA, besides the PDF and the stochastic moments of the solution, is that SSI can be directly calculated analytically from the coefficients of the polynomial. Therefore, computing the SSI is straightforward with almost no additional computational cost as soon as the gPCE of $\hat{Y}$ is available. According to Eq. 5.18, the gPCE-based SSI

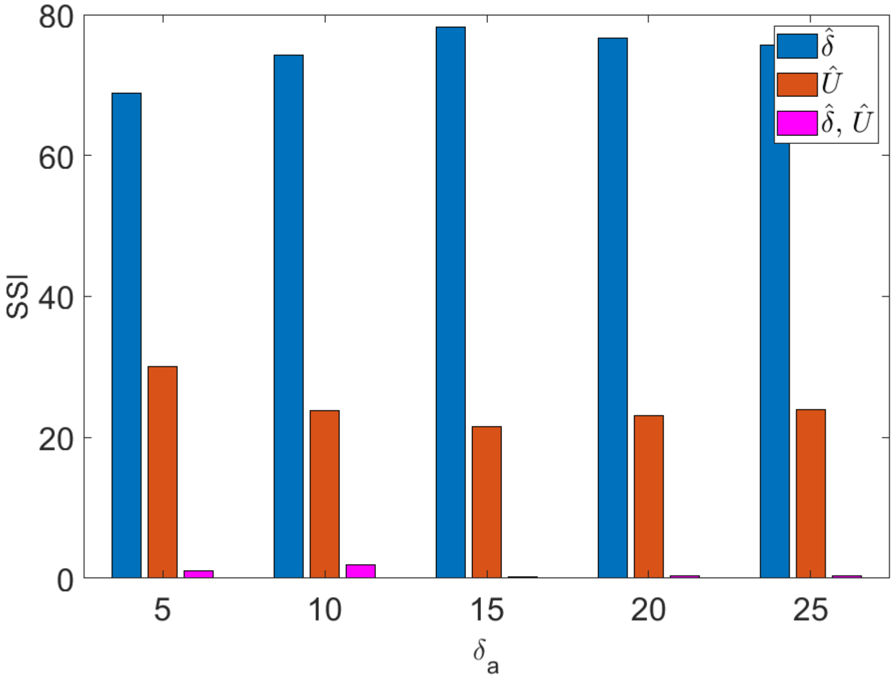

Figure 5.6: The estimation of SSI as a function of the model output δ_a using gPC. The first order of the indices S_1 is related to the SSI of peak SEY $SSI_{\hat{\delta}}$, the second order S_2 related to the SSI of the energy at the peak $SSI_{\hat{U}}$ and S_{12} is related to their combination $SSI_{\hat{\delta},\hat{U}}$.

of uncertain parameters was computed for the order of expansions $p = 3$ in the case of the CSRG model. The SSI for the individual input variables, i.e., $\hat{\delta}$ and $\hat{U}$, and for their interaction to the model output were estimated. S_1 is related to the SSI of peak SEY $SSI_{\hat{\delta}}$, S_2 related to the SSI of the energy at the peak $SSI_{\hat{U}}$ and S_{12} is related to their combination $SSI_{\hat{\delta},\hat{U}}$. The results achieved for four different relative standard deviations σ_r are shown in the bar plot of Fig 5.6. The values are also listed in Table. 5.4. The results demonstrate that the first- and the second-order indices have a significant influence on the probabilistic δ_a. The values $SSI_{\hat{\delta}}$ for different σ_r are indicative of the major effects arising from the changes of the parameter $\hat{\delta}$. Contributions of the indices $SSI_{\hat{\delta},\hat{U}}$ obtained for the interaction between the two variables are not significant.

σ_r %]	$\mathrm{SSI}_{\hat{\delta}}$ [%]	$\mathrm{SSI}_{\hat{U}}$ [%]	$\mathrm{SSI}_{\hat{\delta},\hat{U}}$ [%]
5	68.89	30.06	1.05
10	74.23	23.82	1.96
15	78.26	21.53	0.22
20	76.64	23.06	0.30
25	75.72	23.93	0.36

Table 5.4: The Sobol sensitivity indices of the individual input variables $\mathrm{SSI}_{\hat{\delta}}$, $\mathrm{SSI}_{\hat{U}}$ and their interaction $\mathrm{SSI}_{\hat{\delta},\hat{U}}$ for the relative standard deviations σ_r of 5 %, 10 %, 15 %, 20 % and 25 %.

5.3.3 Uncertainty Quantification for CSIG Model

Similar to the above investigations on the probabilistic CSRG model output δ_a, the UQ for the CSIG model output δ_a with respect to the uncertainties in the parameters of the SEY model was investigated. Therefore, the variations of the following three study cases were considered: 1) $\hat{\delta}$; 2) $\hat{U}$; 3) $\hat{\delta}$ and $\hat{U}$. For the first case of the computation of the variability of $\hat{\delta}$, uniformly distributed random variable samples of $\hat{\delta}$ were modeled with the mean value μ of 2.1 with a relative standard deviation σ_r up to 90 %. The probabilistic model parameters of $\hat{\delta}$ with the lower and upper boundaries $U[a, b]$ are given in Table 5.5. The convergence of the truncated polynomial expansion of δ_a was determined by computing the relative error of its variance. The relative error of the gPCE approximation of δ_a for degree $p = 2$ was calculated for each relative standard deviation 10 %, 15 %, 20 %, 25 %, 30 %, 35 %, 60 % and 90 %. The results of the relative error of the variance of the δ_a exhibited a good convergence at $p = 2$. The error shown in Fig. 5.7 (left) is below 1 % for each study case. The probabilistic density functions of δ_a were computed for the different relative standard deviations up to a maximum of 90 %. Figure 5.7 (right)

σ_r [%]	lower boundary (a)	upper boundary (b)	mean (μ)
10	1.890	2.310	2.1
15	1.785	2.415	2.1
20	1.680	2.520	2.1
25	1.575	2.625	2.1
30	1.470	2.730	2.1
35	1.365	2.835	2.1
60	0.840	3.360	2.1
90	0.210	3.990	2.1

Table 5.5: Probabilistic model parameters of $\hat{\delta}$ in $U[a, b]$ in case of CSIG model.

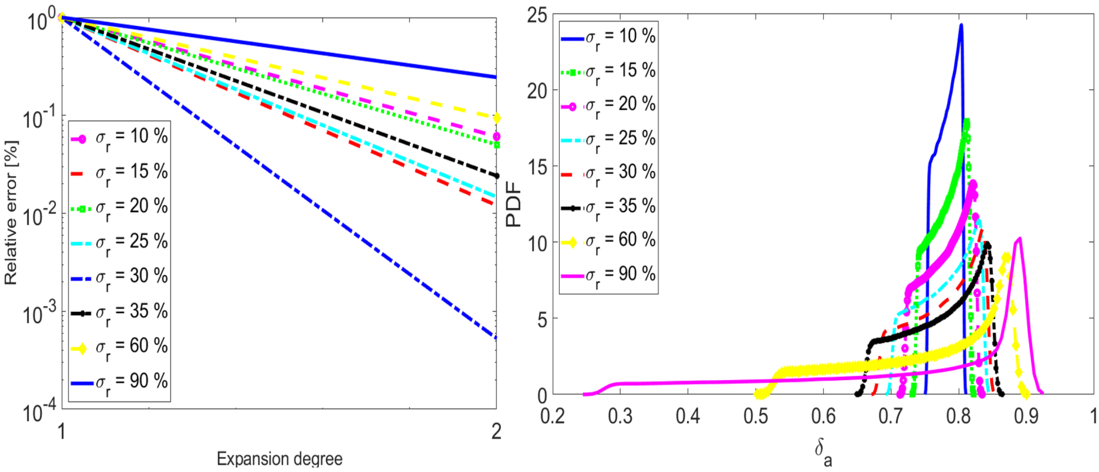

Figure 5.7: Left: Convergence of the variance of the probabilistic δ_a computed via the uni-variate gPCE at degree $p = 2$ for different relative standard deviation of 10 %, 15 %, 20 %, 25 %, 30 %, 35 %, 60 % and 90 %, in $\hat{\delta}$ in case of the CSIG model; right: the corresponding PDFs of δ_a determined via second-order uni-variate gPCE for the variability of $\hat{\delta}$.

depicts the PDF of δ_a for arbitrarily chosen eight σ_r. The results of these study cases showed that all δ_a values are below unity even after the 90 % variations of the uncertain parameter $\hat{\delta}$. However, unlike the investigation on the CSRG model, for the simulation model CSIG, the estimated probabilistic densities of the δ_a for uncertain $\hat{\delta}$ for all study cases show a strong asymmetry (see Fig. 5.7 (right)).

For the second case of a univariate study, the influence of the uncertain parameter energy at peak SEY $\hat{U}$ in the multipactor threshold for the CSIG model was investigated. Uniformly distributed random variable samples of $\hat{U}$ were modeled considering a mean value of μ of 250 for different σ_r up to 90 %. In Table 5.6, the probabilistic model parameters of $\hat{U}$ in $U[a, b]$, where the lower and the upper boundary were set to 10 % and 90 %, respectively, are shown. The quantitative

σ_r [%]	lower boundary (a)	upper boundary (b)	mean (μ)
10	225.00	287.50	250
15	212.50	284.65	250
20	200.00	300.00	250
25	187.50	312.50	250
35	162.50	337.50	250
60	100.50	400.00	250
90	25.00	475.00	250

Table 5.6: Probabilistic model parameters of $\hat{U}$ in $U[a, b]$ in case of CSIG model.

representation of the gPCE accuracy for the approximation of δ_a was computed using the relative error of the variance of the RMS value of δ_a. The results were approximated with orders of gPCE p up to 3 for the σ_r of 10 %, 25 %, 35 %, whereas gPCE $p = 2$ applied for the σ_r of 15 %, 20 %, 25 %, 60 % and 90 %. As shown in Fig. 5.8 (left) a good convergence of the variance of the RMS value of the coefficients for each σ_r is obtained. In all cases, the values of the relative errors are below 0.1 %.

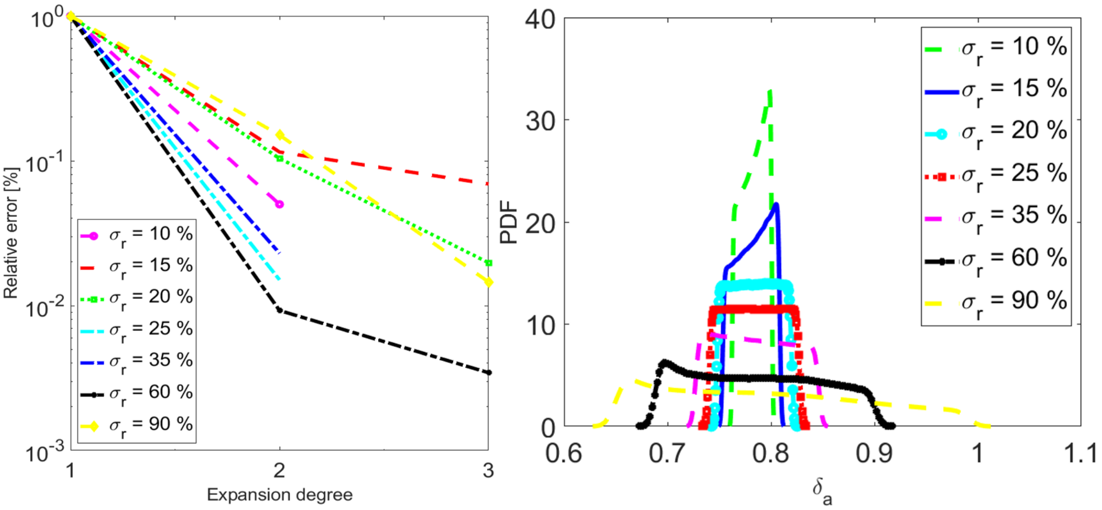

Figure 5.8: Left: Relative error of the variance of the RMS value for the gPCE degree p of up to 3 in case of a relative standard deviation of σ_r of 5 %, 10 %, 15 %, 20 %, 25 %, 30 % and 35 % in energy at peak yield $\hat{U}$; right: PDFs of δ_a evaluated via third-order uni-variate gPCE for the variability of $\hat{U}$.

To compute the PDF of the probabilistic δ_a, the uni-variate expansion with the polynomial degree up to 3 was employed based on random variable samples of $\hat{U}$. Polynomial degree of 2 was sufficient to achieve an accurate representation of the PDF of the probabilistic δ_a for the σ_r of 15 %, 20 %, 25 %, 60 % and 90 %, while an increase of polynomial degree 3 was required for the σ_r of 10 %, 25 %, 35 %. Figure 5.8 (right) shows the predicted PDFs of the second and third-order gPCE up to 90% of σ_r of $\hat{U}$. These results revealed asymmetric probabilistic densities of δ_a for the deviations 10 % and 15 % in $\hat{U}$ and a slight asymmetry for σ_r of 35 %, 60 % and 90 % while symmetric probability densities result in case of 20 % and 25 % of σ_r. Moreover, the larger δ_a is more probable than a smaller one compared to the mean. Almost up to 90 % of deviations σ_r in $\hat{U}$ ensure that the values of δ_a stay near unity.

Finally, uncertainties in both parameters, $\hat{\delta}$ and $\hat{U}$, were considered to investigate their influence on the CSIG model solution δ_a. The multi-variate expansion of the probabilistic δ_a with the polynomial degree p of 2 was employed for the calculation of its PDF. The probabilistic model parameters of $\hat{\delta}$ and $\hat{U}$ were applied with different relative standard deviations up to a maximum of 60 % for the mean values 2.1 and

250, respectively. To monitor the convergence of the stochastic solution, the relative error of the variance of the probabilistic δ_a was computed with the second-order of gPCE. Figure 5.9 (left) shows the results for the different σ_r of 10 %, 15 %, 20 %, 25 %, 35 % and 60 %. The convergence of the variance is visible as the relative error is below 0.1 % for each study case. The PDFs of δ_a shown in Fig. 5.9 (right) were obtained for the parameters $\hat{\delta}$ and $\hat{U}$ with uncertainties up to the maximum deviations of 70 % from their mean values. The results were computed for the 3^{rd} order gPCE. The PDF of δ_a is rather symmetric for the uncertainties of 10 %, 15 %, 20 % and 25 % in $\hat{\delta}$ and $\hat{U}$, whereas it is a slightly asymmetric for the deviations of 30 %, 35 %, 40 %, 50 %, 60 % and 70 %. The results also show that up to the uncertainties of 60 % in both variables $\hat{\delta}$ and $\hat{U}$, the δ_a remains less than unity.

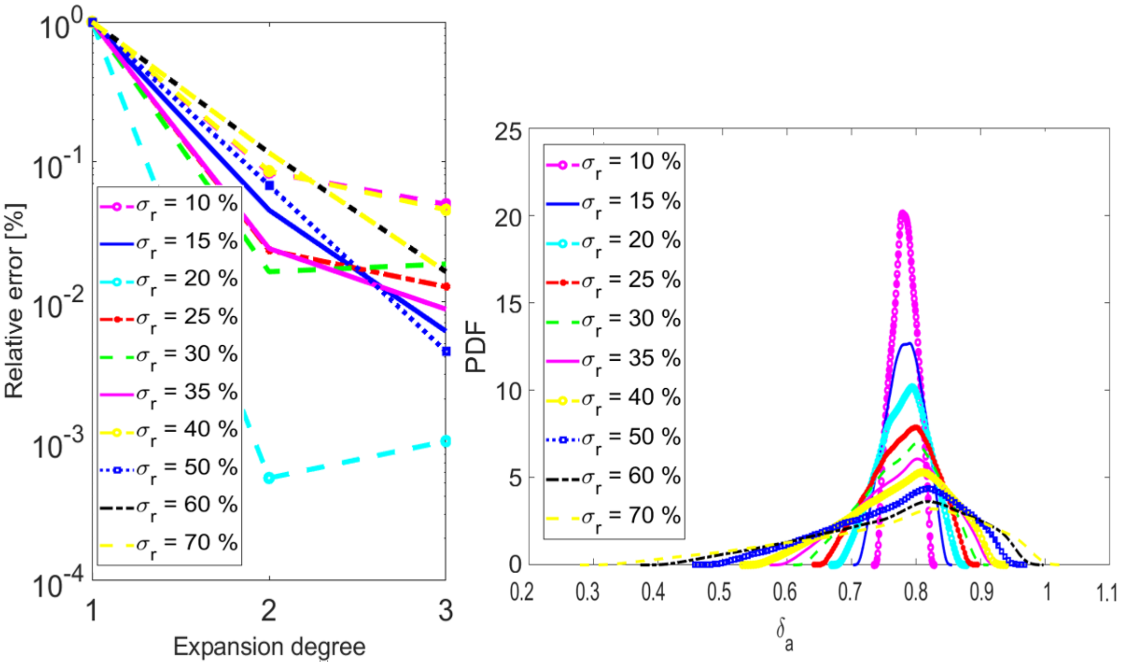

Figure 5.9: Left: A relative error of the variance of the RMS value for the gPCE degree p of up to 3 in case of a relative standard deviation of σ_r of 5 %, 10 %, 15 %, 20 %, 25 %, 30 %, 35 %, 40 %, 50%, 60 % and 70 % in energy at peak yield $\hat{U}$; right: PDFs of δ_a evaluated via third-order uni-variate gPCE for the variability of $\hat{U}$.

In conclusion, for the two-dimensional case, the CSIG model can avoid MP up to 60 % of uncertainties in the two parameters while the CSRG works only within 15 % of variations of uncertain parameters. Therefore, the CSIG model might be more advantageous in case of higher uncertainties in the SEY.

5.3.4 Computation of gPCE-based Sobol Indices for CSIG

Similar to the SA in the case of the CSRG model, we computed the SSI based on gPCE to assess which input variable has the most influence on the model output δ_a in terms of MP threshold. In the computation, different deviations of the uncertain input parameters were taken into account. The gPCE-based SSI of uncertain parameters was computed for the order of expansions $p = 3$ in case of the CSIG model. The SSI for the individual input variables, i.e. $\hat{\delta}$ and $\hat{U}$, and for their interaction to the model output were estimated. As mentioned before, the first and the second order indices represent the SSI of peak SEY $\mathrm{SSI}_{\hat{\delta}}$ and the SSI of the energy at the peak $\mathrm{SSI}_{\hat{U}}$, respectively, and their combination $\mathrm{SSI}_{\hat{\delta},\hat{U}}$. For the computation, different relative standard deviations σ_r up to 70 % were considered. The results are shown in the bar plot of Fig. 5.10. The values are also listed in Table. 5.7. Similar to previous case study, the first- and the second-order indices have a significant influence on the probabilistic δ_a. The values $\mathrm{SSI}_{\hat{\delta}}$ for different σ_r are indicative of the major effects arising from the changes of the parameter $\hat{\delta}$. Contributions of the indices $\mathrm{SSI}_{\hat{\delta},\hat{U}}$ obtained for the interaction between the two variables are insignificant.

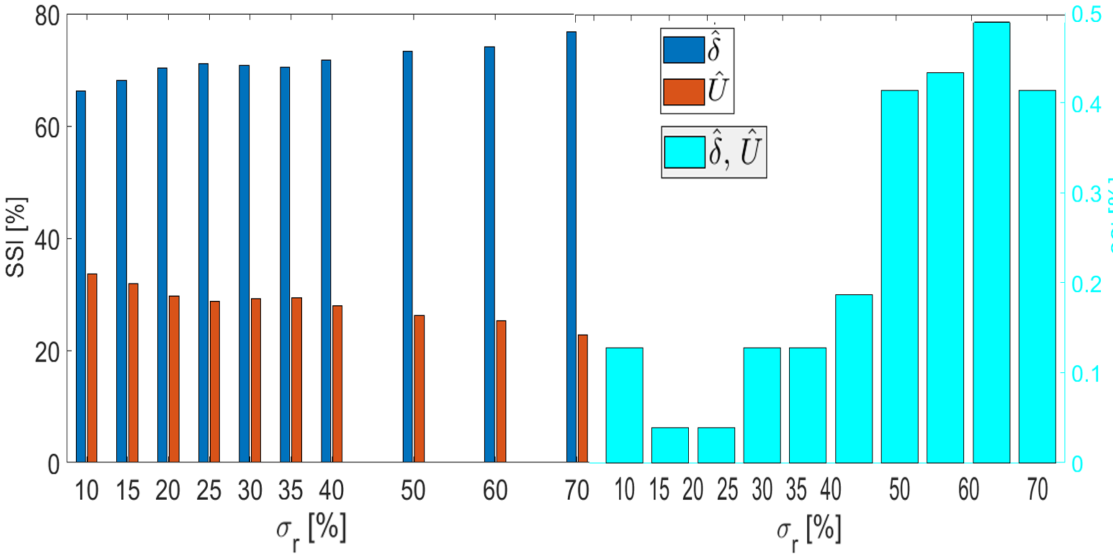

Figure 5.10: The SSI as a function of the model output δ_a using gPC. The first order of the indices S_1 is related to the SSI of peak SEY $\mathrm{SSI}_{\hat{\delta}}$, the second order S_2 related to the SSI of the energy at the peak $\mathrm{SSI}_{\hat{U}}$ and S_{12} is related to their combination $\mathrm{SSI}_{\hat{\delta},\hat{U}}$.

σ_r %]	$\mathrm{SSI}_{\hat{\delta}}$ [%]	$\mathrm{SSI}_{\hat{U}}$ [%]	$\mathrm{SSI}_{\hat{\delta},\hat{U}}$ [%]
10	66.28	33.59	0.13
15	68.05	31.91	0.04
20	70.24	29.72	0.04
25	71.11	28.76	0.13
30	70.71	29.15	0.13
35	70.45	29.36	0.19
40	71.66	27.91	0.42
50	73.38	26.18	0.44
60	74.17	25.33	0.50
70	76.76	22.82	0.42

Table 5.7: The SSI of the individual input variables $\mathrm{SSI}_{\hat{\delta}}$, $\mathrm{SSI}_{\hat{U}}$ and their interaction $\mathrm{SSI}_{\hat{\delta},\hat{U}}$ for the relative standard deviations σ_r of 10 %, 15 %, 20 %, 25 %, 30 %, 35 %, 40 %, 50 %, 60 % and 70 %.

6 Summary and Outlook

The development of the superconducting radio frequency photoinjector (SRF gun) represents the most promising technology for many applications. However, there are various challenges during the operation. Electron multipacting is one of the recently observed difficulties for the SRF gun. Multipactor discharge limits the accelerating gradient E_{acc} in the cavity, moreover, it might cause impairment of the RF components and distortion of the RF signal.

The aim of this thesis was to design an multipactor-reduced photocathode channel which could potentially improve the gun performance. For this reason, first, a detailed analysis of multipacting in the critical area of the ELBE's SRF gun was carried out, and various suppression techniques of multipactor discharge were investigated. Then the parameters of the specific surface structures, which proved to be effective methods to mitigate the multipacting phenomenon from the photocathode unit, were optimized with respect to the number of particles as well as the average secondary emission yield (δ_a). Finally, the uncertainty quantification and global sensitivity analysis on the variability of the secondary electron emission coefficients of a newly designed cathode tip were carried out.

Quantitative and qualitative systematic numerical studies, as well as simple analytical analyses, were conducted. Simulations of the SRF gun were carried out for a Copper photocathode and a niobium cavity combined with the advanced probabilistic model for the secondary emission process developed by Furman and Pivi. The electromagnetic field and the electron multipactor discharge simulations were performed using the 2D code MultiPac 2.1 as well as the 3D software CST STUDIO SUITE®, namely CST MICROWAVE STUDIO® and CST PARTICLE STUDIO®. A comparison of analytical multipactor predictions for a simplified plane-parallel model with our numerical simulations provided reasonable results. The results obtained by the numerical and analytical studies indicated that *two sided* 1^{st} order multipacting exists in the cathode unit where the inner and the outer parts are separated by 0.75 mm gap width. The numerical study [cf. Fig.3.8] revealed that this type of multipacting occurs at low electric field amplitudes typically between $\sim$ 70 kV/m and $\sim$ 194 kV/m. Moreover, the δ_a was larger than one for the average impact energy (U_a) values between 35 and 50.8 eV. The highest generation of secondary electrons, or the peak δ_a of 1.44, was produced at the gap field of 112.6 kV/m, while the corresponding accelerating field in the cavity is about 1.55 MV/m. In particular, the latter confirmed that the simulation results are in a good agreement with the experimental data at ELBE. Similarly, the δ_a for the niobium surface was calculated.

The result is displayed in Fig.3.8. The δ_a of niobium was below one in the whole range of field levels. Thus, the contribution of the niobium surface to multipacting is negligible.

Various possible remedies, such as geometric modifications, static electric field perturbation, anti-multipactor coatings, and anti-multipactor grooves of the cathode's surface, to suppress electron multipactor discharge and to improve the breakdown threshold in the critical area of the SRF gun were investigated. Introducing anti-multipactor grooves, namely cylindrically symmetric rectangularly grooved and cylindrically symmetric triangularly grooved, on the cathode surface proved to be an efficient way to suppress vacuum electron multipacting. The parameters for grooved surfaces were optimized with respect to the number of particles as well as δ_a. Initially, the geometric parameters of the grooved surfaces with respect to the number of particles over time were optimized manually. This gives certain flexibility to choose dominant parameters for further optimization studies. Then optimizing the geometric parameters of the models was done using the so-called trust-region algorithm. The initial parameters were chosen based on the manual optimization results, which were already close to optimum. The automated optimization of the grooved surfaces is based on the optimization goal that the δ_a is lower than the threshold, i.e., less than unity, for each possible combination of parameter values.

With the best optimal parameters, i.e. the width $w = 0.328$ mm, the height $h = 0.865$ mm, and the distance between two neighboring grooves $g = 0.48$ mm of the cylindrically symmetric rectangularly grooved surface, the peak δ_a for copper and niobium surfaces reached only 0.93 and 0.63, respectively, at 112.6 kV/m, where the peak generation of secondaries was observed within the flat gap. The corresponding average impact energies for copper and niobium were 21.1 eV and 49.1 eV, respectively. These values are lower than the first crossover energies (U_{c1}), i.e., 27.3 eV and 76 eV, for copper and niobium, respectively. Next, the amplitude of the electric field was swept for the wide range of 78.62 to 215.3 kV/m in order to obtain the limits of field levels for multipacting for the optimal parameters. As depicted in Figure 4.11, all values of the calculated δ_a for copper and niobium stay below the threshold, which is unity. Similarly, the optimum parameters for the cylindrically symmetric isosceles grooved are a grazing of $\theta_g = 88.8°$ or angle $\alpha = 45.6°$ and a width of $w = 0.293$ mm. The model reduces the peak of δ_a for copper and niobium to 0.897 and 0.301, respectively, at 112.6 kV/m, where the maximum generation of secondaries was observed within the flat surface of coaxial structure (Model C). The corresponding average impact energies are 15.60 and 28.54 eV for both copper and niobium, which are lower than the first crossover energies (U_{c1}) of 27.3 eV for copper and 76 eV for niobium, respectively. Next, to obtain the field level with respect to δ_a for the cylindrically symmetric isosceles grooved surface, a parameter sweep of the electric field amplitude was performed from 78.62 kV/m to 212.27 kV/m. As Fig. 4.16 depicts, all values of the calculated δ_a for copper and niobium, within this amplitude range of the electric field, are below the threshold, which is unity.

Therefore, multipacting is totally suppressed in the region. Accordingly, both types of grooved surfaces are effective in reducing the SEY below the multipacting threshold and to totally suppress multipacting in the cathode region.

Finally, the robustness of the proposed models, namely cylindrically symmetric rectangularly grooved and cylindrically symmetric isosceles grooved, was examined through uncertainty quantification and global sensitivity analysis. The uncertainty quantification was carried out to appraise and quantify the impact of the SEY uncertainty on the newly designed and optimized models of the cathode vicinity. For this purpose, we applied advanced tools, i.e. the generalized polynomial chaos expansion, to quantify the effect of uncertainty and to assess to which extent the achieved results of the models can be affected by changing the values of the SEY. As the numerical simulation results indicated, both cylindrically symmetric rectangularly grooved and cylindrically symmetric isosceles grooved models could work with high uncertainties in the SEY, e.g. for the two-dimensional case, the cylindrically symmetric isosceles grooved model can avoid multipactor discharge up to 60% of uncertainties in the parameters. Moreover, the systematic investigation of the global sensitivity analysis was performed to identify the critical parameters of SEY curves that influence the uncertainty of the model output (δ_a) the most. Among various global sensitivity analysis approaches, the Sobol sensitivity indices, which are considered as the most accurate sensitivity measure, based on the generalized polynomial chaos were applied. The Sobol sensitivity indices for the individual input variables, i.e. $\hat{\delta}$ and $\hat{U}$, of SEY coefficients and for their interaction to the model output were estimated. The first- and the second-order indices have a significant influence on the probabilistic δ_a. The values $\mathrm{SSI}_{\hat{\delta}}$ for different σ_r are indicative of the major effects arising from the changes of the parameter $\hat{\delta}$. Contributions of the indices $\mathrm{SSI}_{\hat{\delta},\hat{U}}$ obtained for the interaction between the two variables are insignificant.

In conclusion, the development of this multipacting-free cathode unit particularly serves the further development at ELBE and thus the increase of the performance of existing and future compact accelerators. Nonetheless, the concrete and methodological results obtained here are of high value for similar projects. Moreover, multipacting is still one of the challenges in many other RF components, the knowledge gained is also applicable to similar projects.

A *Two Sided* Multipacting

A simple analytical model for *two sided* multipactor was set up for the coaxial part of the structure, where MP is critical as denoted in chapter two and chapter three. For local inspection of a small volume, two parallel plates can approximate the coaxial line structure to predict the order of MP and the range of the electric field in which MP may occur. As shown in Fig. A.1, the two electrodes were separated by a gap of width d. Both the magnetic field and the space charge effects, can be ignored since their effects are negligible here [138], [96].

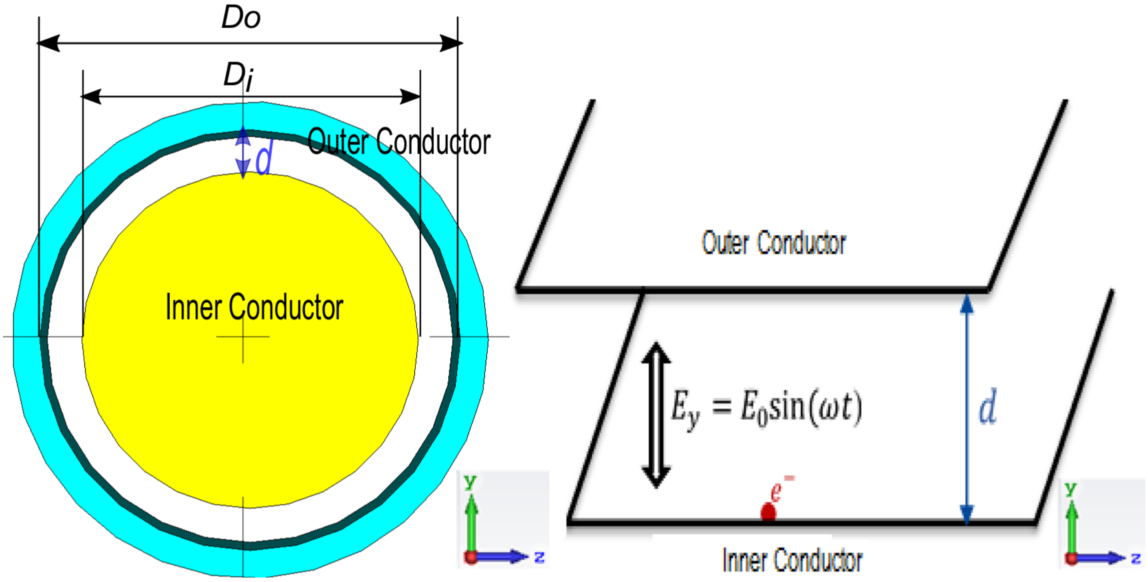

Figure A.1: Left: the coaxial line structure (Model C); right: a two parallel plates model for analytical treatment of *two sided* MP in a coaxial line structure.

The homogeneous perpendicular electric field distribution across the gap was assumed to be $E = E_0 \sin(\omega_g t)\hat{y}$, where ω_g is the angular frequency, t is the time and

$$E_0 = V_g/d. \tag{A.1}$$

V_g is the RF voltage across the gap, and the gap width d is given by $d = D_o - D_i$, where D_o is the outer conductor diameter and D_i is the inner conductor diameter. Let us assume that an electron e^- starts from the inner conductor with initial phase φ_0 and moves toward the outer conductor (in y direction) via the RF field. Thus, the equation of motion for the electron in the two parallel plates can be written as

$$\ddot{y} = \frac{eE_0}{m_e}\sin(\omega_g t + \varphi_0)\hat{y}, \tag{A.2}$$

where e is the electric charge and m_e is the electron mass at rest. There are two approaches in the literature to analyze the motion of the electron along the RF field and to predict the *two sided* MP occurrence. In the first case (see e.g. [96]), we assumed for the initial condition (at y_0) that the electron is emitted with zero energy U (eV) when the RF field is zero so that the initial phase is zero. Then, integrating the equation of motion as a function of time gives the velocity

	Numerical Solution			Analytical Solution	
	E [kV/m] (at $\hat{\delta}_a$)	U [eV] (at $\hat{\delta}_a$)	$\hat{\delta}_a$	E [kV/m]	U [eV]
Model C					
$d = 0.75$ mm	112.7	45.6	1.440	90.3	43.1
$d = 1.5$ mm	153.7	387.3	2.100	180.5	172.4
$d = 3$ mm	353.8	387.3	2.100	361.0	689.5
CSRG surface					
$d = 0.75$ mm	112.9	22.6	0.956	...	...
CSIG surface					
$d = 0.75$ mm	113.0	15.6	0.910	...	...

Table A.1: Analytical and numerical solutions of the first order *two sided* MP.

$$\dot{y} = \frac{eE_0}{m_e\omega_g}(\cos\omega_g t - 1), \tag{A.3}$$

and the position

$$y = \frac{eE_0}{\omega_g^2 m_e}\sin\omega_g t - \frac{eE_0}{\omega_g m_e}t. \tag{A.4}$$

Then, as discussed in chapter two, the resonant condition for the *two sided* MP requires that the transit time of the electron to the outer conductor (at position y = d) is an odd integer number of the half an RF period [96]

$$t = \frac{(2n-1)\pi}{\omega_g} = \frac{T}{2}(2n-1), \qquad n = 1, 2, 3, ... \tag{A.5}$$

where T is the RF period and n is the order of MP. By putting equation (A.5) into equation (A.4), the voltage in the gap of the two parallel plates (V_g) in case of *two sided* MP becomes

$$V_g = E_0 d = \frac{4\pi m_e c^2 d^2}{(2n-1)e\lambda^2}, \tag{A.6}$$

and the corresponding impact energy (U) is given by

$$U = \frac{8m_e c^2 d^2}{(2n-1)^2 \lambda^2}, \tag{A.7}$$

where c is the speed of light and λ is the RF wave length. By using the last two equations, the prediction of a possible *two sided* MP of n^{th} order is therefore possible in the vicinity of the cathode.

The analytical solution of the above equations and the numerical simulation results for Model C, the CSRG and the CSIG surfaces are summarized in Table A. The simulation results are recorded for the gap width d of 0.75 mm, 1.5 mm and 3 mm in case of Model C, and for the gap width d of 0.75 mm in case of CSRG and CSIG at the operating frequency of 1.3 GHz. A larger gap improves the threshold voltage and the electric field.

A second approach leads to the stability condition for the two parallel plates. This can be achieved by assuming that the electron e^- starts from the inner conductor with a non-zero velocity at the initial phase φ_0. The gap field and the gap voltage can be obtained from the derivative of Eq. (A.2) with respect to the phase. A detailed derivation and explanation can be found in [143, 120]. This approach is highly relevant in a low pressure gas. However, for the vacuum multipactor in the parallel plates where the RF field is homogenous, the first approach is more reasonable [143]. Hence, we assume that the secondary emission yield depends only on the impact energy since the impact of the electrons is perpendicular in a homogeneous field.

B Model of Secondary Emission Yield

The results discussed in chapter three and chapter four were obtained using Furman's model of SEY except the results achieved for the Anti-multipactor layer (discussed in Section 4.4). The *Imported emission model* was employed for the Anti-multipactor layer study. The key formulations with respect to the SEY models, as implemented in the CST PS, are noted below.

Furman Model of Secondary Emission Yield

As mentioned in chapter two, the model distinguishes three different ways of generating secondary electrons [42]: true secondary electrons, elastic reflection (*backscattered* electrons), and inelastic reflection (*rediffused* electrons).

Furman's Model for True Secondary Electrons

The true secondary emission coefficient can be described as:

$$\delta_{ts}(E_0, \theta_0) = \hat{\delta}(\theta_0) D(E_0/\hat{E}(\theta_0)), \tag{B.1}$$

where $\hat{\delta}$ is a peak value of SEY and the corresponding energy $\hat{E}$. The universal scaling function $D(x)$ can be defined as

$$D(x) = \frac{sx}{s - 1 + x^s}, \tag{B.2}$$

where s is an adjustable parameter that must be greater than one. The *incident angle* dependence of the $\hat{\delta}$ and $\hat{E}$ are assumed as

$$\hat{\delta}(\theta_0) = \hat{\delta}_{ts}[1 + t_1(1 - \cos^{t_2} \theta_0)], \tag{B.3}$$

$$\hat{E}(\theta_0) = \hat{E}_{ts}[1 + t_3(1 - \cos^{t_4} \theta_0)], \tag{B.4}$$

The energy spectrum function:

$$f_{n,ts} = \theta(E) F_n E^{p_n - 1} \exp^{-E/\epsilon_n}, \tag{B.5}$$

where p_n and ϵ_n are phenomenological parameters which are the finiteness of $\delta(E_0, \theta_0)$

$$F_n^n = \frac{P_{n,ts}(E_0)}{(\epsilon_n^{p_n} \Gamma(p_n))^n P(np_n, E_0/\epsilon_n)}, \tag{B.6}$$

The probability $P_{n,ts}$ for emitting n true secondary electrons for the binomial distribution can be written as

$$\acute{\delta}_{ts} = \frac{\delta_{ts}}{1 - \delta_{bs} - \delta_{rd}}, \tag{B.7}$$

$$\acute{P}_{n,ts} = \binom{M}{n} p^n (1-p)^{M-n}, p = \frac{\acute{\delta}_{ts}}{M}. \tag{B.8}$$

Furman Model for *Backscattered* Electrons

The secondary emission coefficient for the *backscattered* electrons can be described as:

$$\delta_{bs}(E_0, \theta_0) = \delta_{bs}(E_0, 0)[1 + e_1(1 - \cos^{e_2}\theta_0)], \tag{B.9}$$

and the SEY for the *backscattered* electrons at normal incidence:

$$\delta_{bs}(E_0, 0) = P_{1,bs}(\infty) + [\hat{P}_{1,bs}]\exp(-\frac{|E_0 - \hat{E}_{bs}|^p}{p^{Wp}}). \tag{B.10}$$

The probability distribution function for the *backscattered* reads as

$$f_{1,bs} = \theta(E)\theta(E_0 - E)\delta_{bs}(E_0, \theta_0)\frac{2\exp(-(E - E_0)^2/2\sigma_{bs}^2)}{\sqrt{2\pi}\sigma_{bs}\mathrm{erf}(E_0/\sqrt{2}\sigma_{bs})}. \tag{B.11}$$

Furman Model for *Rediffused* Electrons

The secondary emission coefficient for the *rediffused* electrons can be described as:

$$\delta_{rd}(E_0, \theta_0) = \delta_{rd}(E_0, 0)[1 + r_1(1 - \cos^{r_2}\theta_0)], \tag{B.12}$$

and the SEY for the *rediffused* electrons at normal incidence:

$$\delta_{rd}(E_0, 0) = P_{1,rd}(\infty)[1 - \exp(-(E_0/E_{rd})^r)]. \tag{B.13}$$

The probability distribution function for the *rediffused* is given by

$$f_{1,\mathrm{rd}} = \theta(E)\theta(E_0 - E)\delta_{\mathrm{rd}}(E_0, \theta_0)\frac{(q+1)E^q}{E_0^{q+1}}. \tag{B.14}$$

The main parameters of the SEY of the Cu model are illustrated in Table B.

Emitted angular spectrum	
α	1
Backscattered electrons	
$P_{1,e}(\infty)$	0.02
$\hat{P}_{1,e}$	0.496
$\hat{E}_e$ [eV]	0
W [eV]	60.86
p	1
σ_{bs} [eV]	2
e_1	0.26
e_2	2
Rediffused electrons	
$P_{1,r}(\infty)$	0.2
E_r [eV]	0.041
r	0.104
q	0.5
r_1	0.26
r_2	2
True secondary electrons	
$\hat{\delta}_{ts}$	1.8848
E_{ts} [eV]	276.8
s	1.54
t_1	0.66
t_2	0.8
t_3	0.7
t_4	1
E_t [eV]	271
δ_t	2.1

Table B.1: The main parameters of the SEY of the Cu model taken from [42]

Secondary Electron Emission for Different Materials

In CST PS, the *Imported emission model* allows to import the data of the SEY for normal incidence angle θ_0. In our simulation we used this model in order to include the measurement data of SEY discussed in Section 4.4. Unlike the Furman's model, this model considers only the true secondaries.

The probability density function of the energy distribution as implemented in CST PS is given by

$$f(U) = (U_0 - U_{\text{threshold}})\frac{2\pi}{2\pi + \theta^2} + U_{\text{threshold}}, \tag{B.15}$$

and the dependency of the energy distribution and the yield on the angle is stated as following

$$U(\theta) = (U_0 - U_{threshold})\frac{2\pi}{2\pi + \theta^2} + U_{threshold}, \tag{B.16}$$

$$\delta(\theta) = \delta(0)(1 + \frac{\theta^2}{2\pi}), \tag{B.17}$$

respectively.

C Mesh Refinement Studies

The *mesh refinement* study is a basic step in numerical simulation. The convergence study was executed to identify an appropriate mesh size for the numerical calculations that ensures the accuracy of the simulation results. This section presents *mesh refinement* studies on Model B, Model C, CSRG and CSIG models. In the case of Model B, the dependence of the resonant frequency f_n on the total number of nodes N_p was investigated. In that case, the following relative accuracy criterion was assumed to obtain an optimum mesh size:

$$\epsilon_f = \max_n \left| \frac{f_{\mathrm{ref},n} - f_n(N_p)}{f_{\mathrm{ref},n}} \right| . \tag{C.1}$$

The operating frequency of the computational model, i.e. 1.3 GHz, is assumed as the reference resonant frequency $f_{ref,n}$. $f_n(N_p)$ is the computed resonant frequencies for the given number N_p of mesh-cells. The convergence plot in Fig. C.1 is achieved by refining the mesh. The eigenmode computation was started with an initial mesh consisting of 233,415 hexahedra. The number of nodes was increased until the result is converged, i.e. the relative error ϵ_f (Eq. C.1) in the computation is acceptably small.

Next, the effect of mesh size on the averaged value $\overline{\mathbf{E}}$ of electric field over the remaining models, namely Model C, CSRG and CSIG surfaces, was studied. $\overline{\mathbf{E}}$ was obtained by evaluating the field integral over these computational domains. The EM field was computed at 1.3 GHz using the frequency domain solver of CST MWS. The field simulation was performed for different *mesh refinement* levels. The relative error was computed by

$$\epsilon_{\overline{\mathbf{E}}} = \max_n \left| \frac{\overline{\mathbf{E}}_{\mathrm{ref},n} - \overline{\mathbf{E}}_n(N_p)}{\overline{\mathbf{E}}_{\mathrm{ref},n}} \right| . \tag{C.2}$$

The averaged value $\overline{\mathbf{E}}$ of the electric field obtained using the largest nodes at the final run is employed as a reference electric field $\overline{\mathbf{E}}_{ref,n}$ and $\overline{\mathbf{E}}_n(N_p)$ is the computed averaged value of the electric field for the given number N_p of meshes. The result was considered to converge as the changes in the field between the last two successive numbers of mesh become small enough. The meshes cells employed for field computation within the three computational domains are depicted in Fig. C.4, Fig. C.6 and Fig. C.8, respectively.

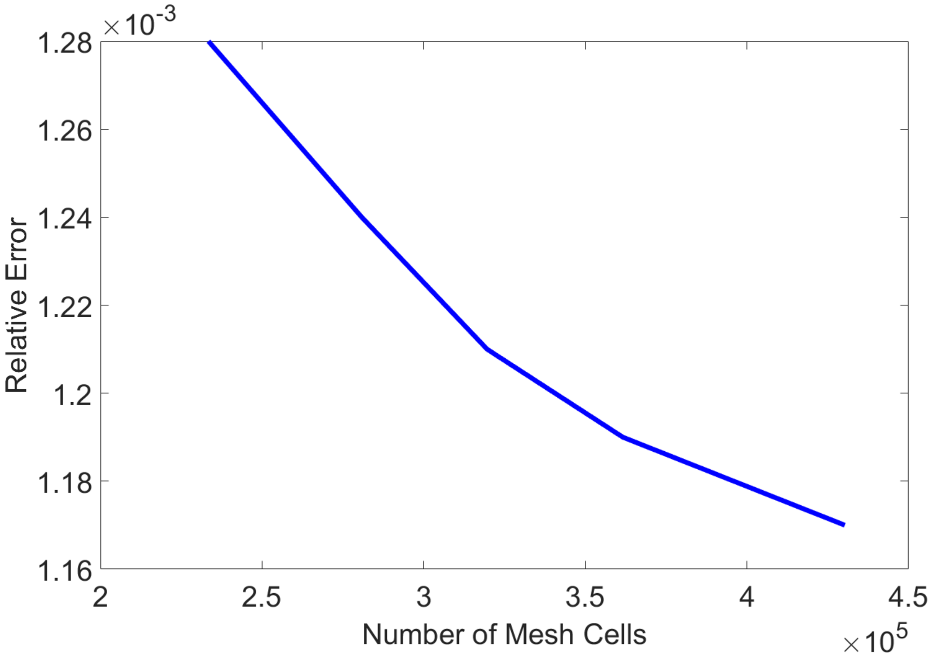

Figure C.1: Numerical convergence of resonant frequency using Eq. C.1 for Model B. The computed resonant frequency for 430,272 mesh cells is 1.298 GHz.

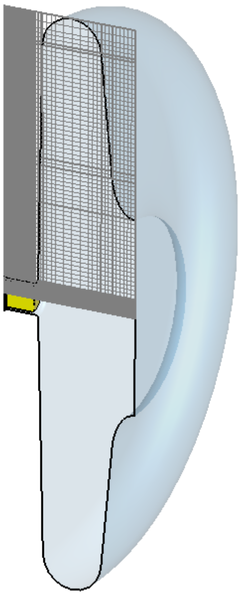

Figure C.2: Mesh used for calculation of resonant frequency and EM field within Model B. Locally refined mesh is used in the cathode region as it is the most critical part. The distribution of electric and magnetic fields of the TM_{010} mode within Model B had values defined for $N_x = 65$, $N_y = 84$, $N_z = 82$ nodes. The corresponding total number of mesh cells is 430,272.

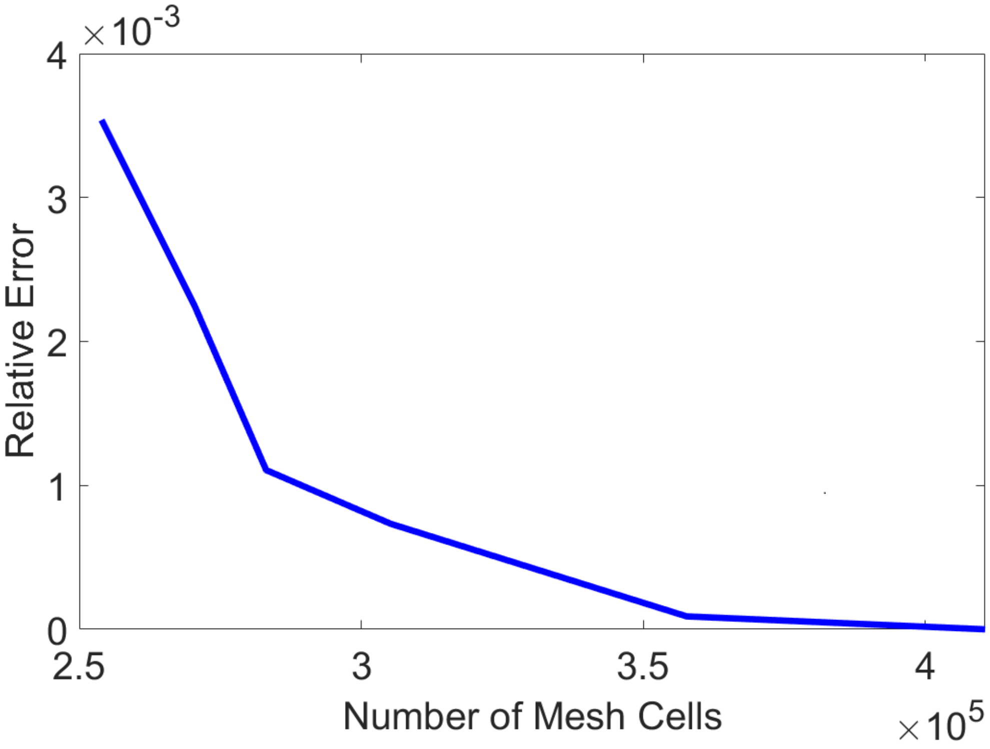

Figure C.3: *Mesh refinement* study of Model C under the convergence criterion stated in Eq. C.2.

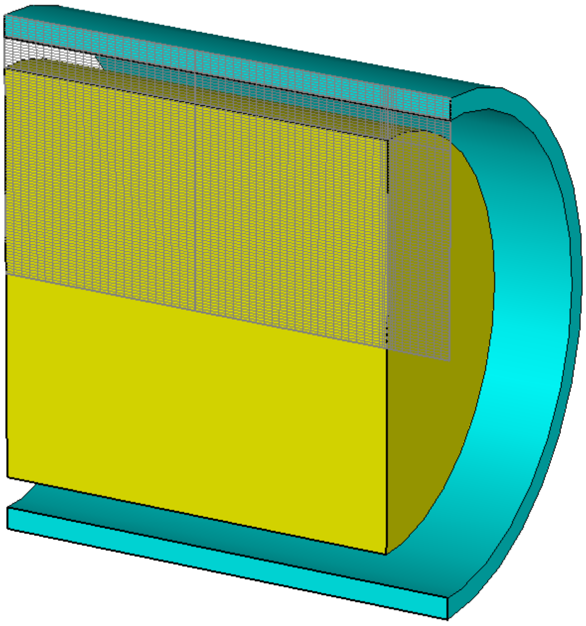

Figure C.4: Discretization of Model C for the calculation of EM field.

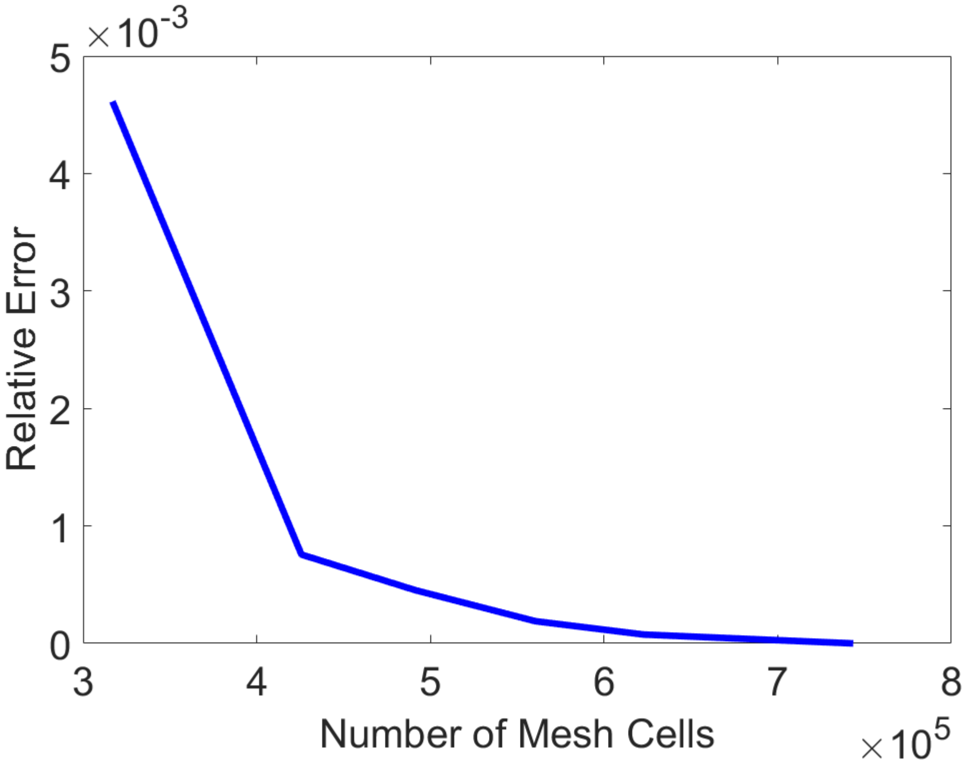

Figure C.5: *Mesh refinement* study for CSRG surface under the convergence criterion stated in Eq. C.2.

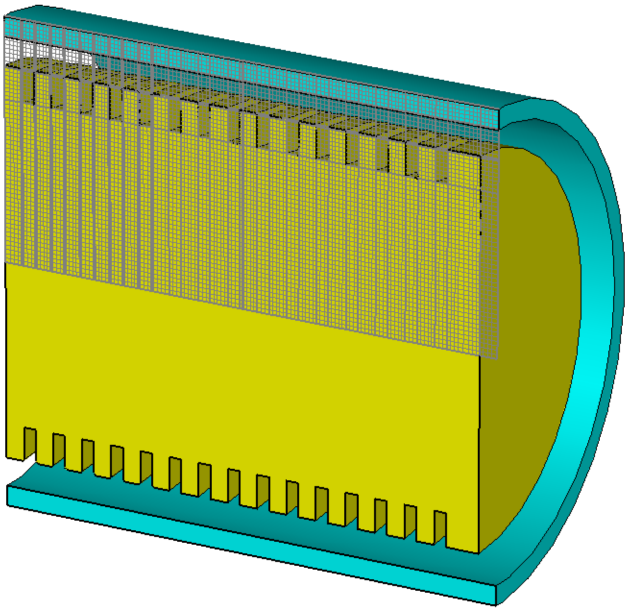

Figure C.6: Mesh employed in CSRG surface for the calculation of EM field.

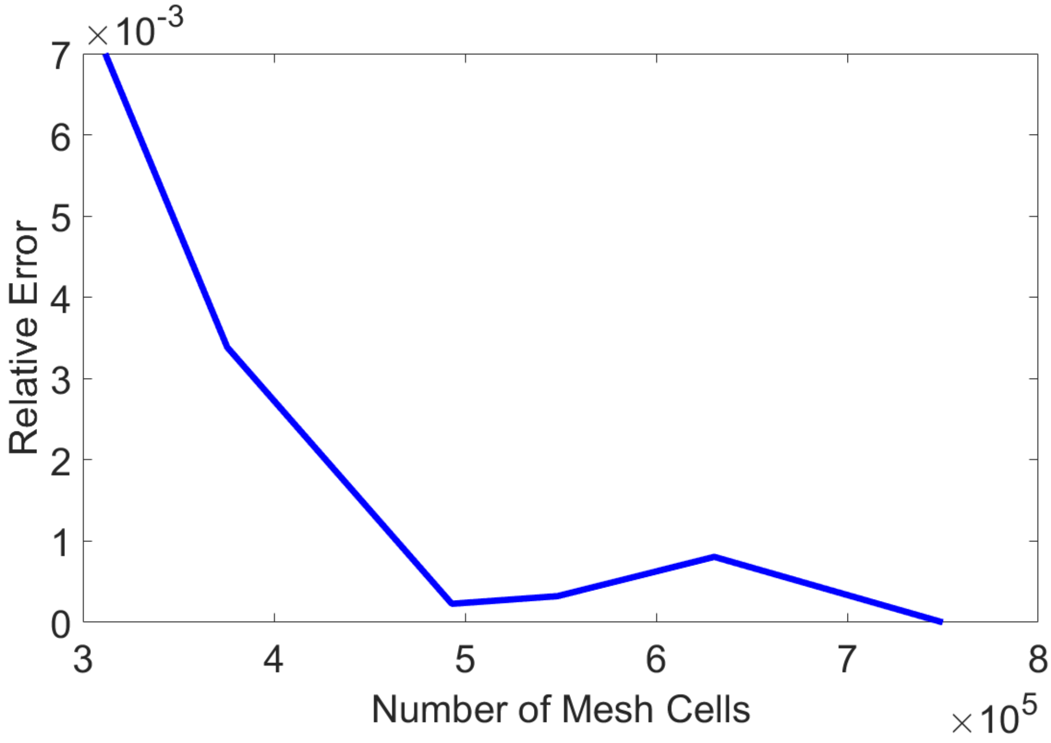

Figure C.7: *Mesh refinement* study for CSIG surface under the convergence criterion stated in Eq. C.2.

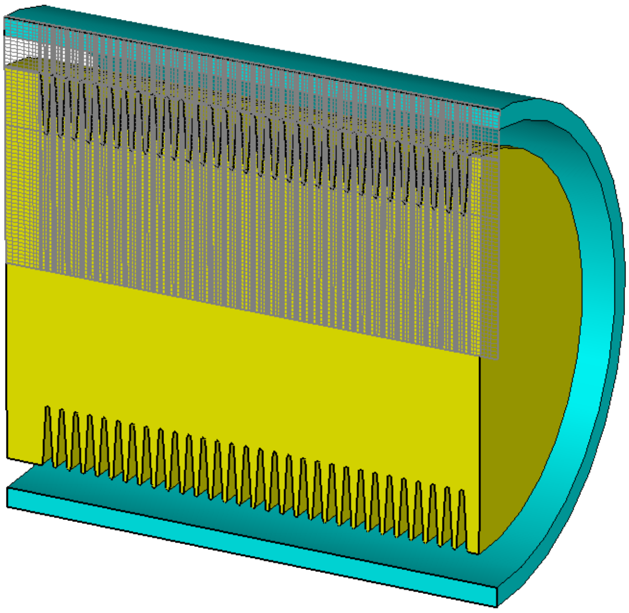

Figure C.8: Mesh used in CSIG surface for the calculation of EM field.

D Trust-region Method

As the CSRG and CSIG models demonstrated promising results in the early stage of this study (see [140], [141]), further investigations including a multi-objective optimization were carried out. Simulations were done using CST Design Studio® (CST DS) by coupling the FD solver of CST MWS and the PIC solver CST PS. Two sub-simulation projects were created and linked to the master file in which the EM field was calculated using the FD solver of CST MWS, and the MP simulations were carried out using the PIC solver of CST PS. The general work flow for multi-dimensional optimization is shown in Fig. D.1.

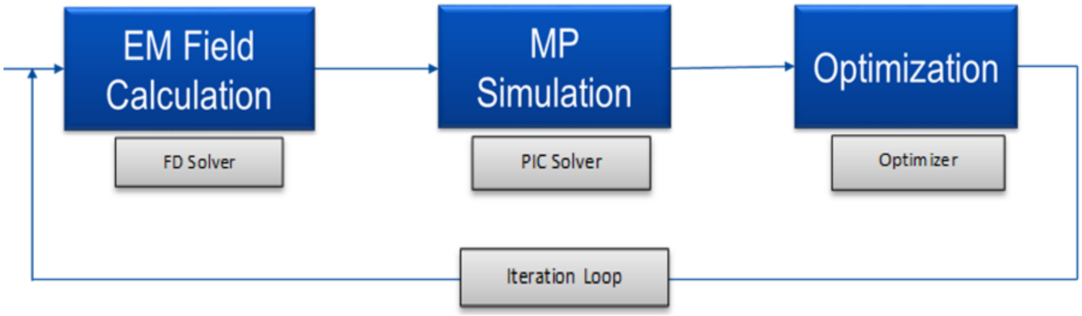

Figure D.1: The general work flow for multi-dimensional optimization.

In the optimizer task, the geometric parameters of the CSRG, such as the width w, the depth of each groove h, as well as the geometric parameters of the CSIG, namely the width of each groove w and the angle α [cf. 4.7], were taken into account. A constrained multi-objective optimization was employed to find the optimal geometric parameters based on the given objective and constraints. One of the main constraints is to have a δ_a less than unity that satisfies one of the conditions in order to avoid MP as noted in Chapter 2. The *trust-region* algorithm is an effective algorithm used to obtain the optimal solution with a few function evaluations. The algorithm was therefore used to minimize the objective function $g(p)$ and obtain the best geometric parameter values of p for the CSRG and the CSIG surfaces, i.e. $p = x_1, x_2, ... = w$, h, and α.

The algorithm works as follows:

- Step 0. The first step of the algorithm is to choose the initial point (x_0) in the space of real numbers and to set an initial trust-region radius Δ_k for the k^{th} iteration (initially $k = 1$).

In the present study, initial parameters were chosen based on our previous manual optimization, which was close to the optimum solution. The initial points $(w_1,\, h_1) = (0.33,\, 0.8)$ for CSRG and $(w_1,\, \alpha_1) = (0.3,\, 80.5°)$ for CSIG were chosen. The initial trust-region radii (Δ_1) in both cases were set to be 10% of the starting points.

- Step 1. Calculate the trial step (s_k) by solving the *trust-region* subproblem

$$\min_{s\in\Re^n} m_k(s) \quad \text{subject to } \|s\| \leq \Delta_k \text{ to reduce } f(x_k + s), \tag{D.1}$$

  where $\|s\|$ is the trust-region constraint, and $\|.\|$ is the standard Euclidean norm.

- Step 2. Decide whether to set $x_{k+1} = x_k + s_k$ or $x_{k+1} = x_k$ based on the reduction of the goal function $g(p)$.

- Step 3. Construct a new model $m_{k+1}(s)$ for the next iteration, choose Δ_{k+1} and set k to $k+1$ and go to step 1.

For the CSRG surface, the geometric parameters with respect to δ_a were optimized using the *trust-region* algorithm so that the optimal geometry was found as noted before. Initially, the value of δ_a was set to less than unity ($\delta_a < 1$), which is a condition for *two sided* MP as discussed in Chapter 2. With this condition, the optimizer was started to run with the given initial points and initial trust-region radii. After 20 iterations, it stopped as the objective function value $g(p)$ reached to 0 at the geometric parameter values of $w = 0.23$ mm and $h = 0.8$ mm for the CSRG surface. In that case, δ_a of the CSRG surface was decreased from 1.440 to 0.956 at 112.7 kV/m, where the maximum generation of secondaries was observed in the Model C. The results were discussed in [142]. Next, even though satisfactory reduction of δ_a of the Cu surface was achieved for the constraint given above ($\delta_a < 1$), we continued to run the optimizer by setting other constraints, i.e. $\delta_a < 0.9$, 0.85, and 0.8, consecutively, to obtain the best possible reduction of δ_a for the grooved surfaces. For $\delta_a < 0.85$, 18 iterations were required to minimize the objective function value to 0.08, and the result converged as shown in Fig. D.2. As a result, the optimal parameters of the CSRG surface, such as $w = 0.328$ mm and $h = 0.865$ mm, were obtained in case of the constraint $\delta_a < 0.85$. For these parameters, the value of δ_a for the Cu surface was reduced to 0.93 at 112.6 kV/m. Finally, in the case of δ_a less than 0.8, the value of the goal function and of the δ_a for the CSRG surface stayed almost the same.

Similar procedures and settings were considered for the geometric optimization of CSIG surface with respect to δ_a. Like CSRG, the optimizer was run for $\delta_a < 1$, 0.9, 0.85, and 0.8, consecutively. In the case of $\delta_a < 0.85$, the objective function value was minimized to ~0.04, and the result converged as shown in Fig. D.3. Correspondingly, the optimum parameters for the CSIG are a grazing of $\theta_g = 88.8°$ or angle $\alpha = 45.6°$ and a width of $w = 0.293$ mm. The model reduces the peak of δ_a for Cu to 0.897 at 112.6 kV/m. Similar to the CSRG case, for δ_a less than 0.8, the value of the goal function and δ_a for the Cu surface of CSIG stayed almost the same.

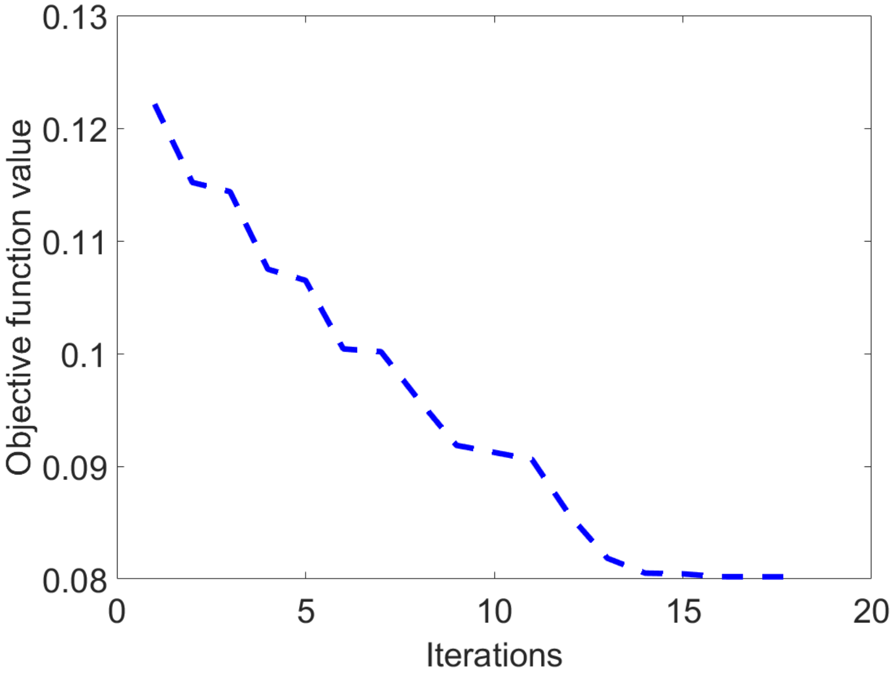

Figure D.2: The *trust-region* algorithm performance to minimize the objective function at the starting point of the parameters $(w_1, h_1) = (0.33, 0.8)$ in case of CSRG surface.

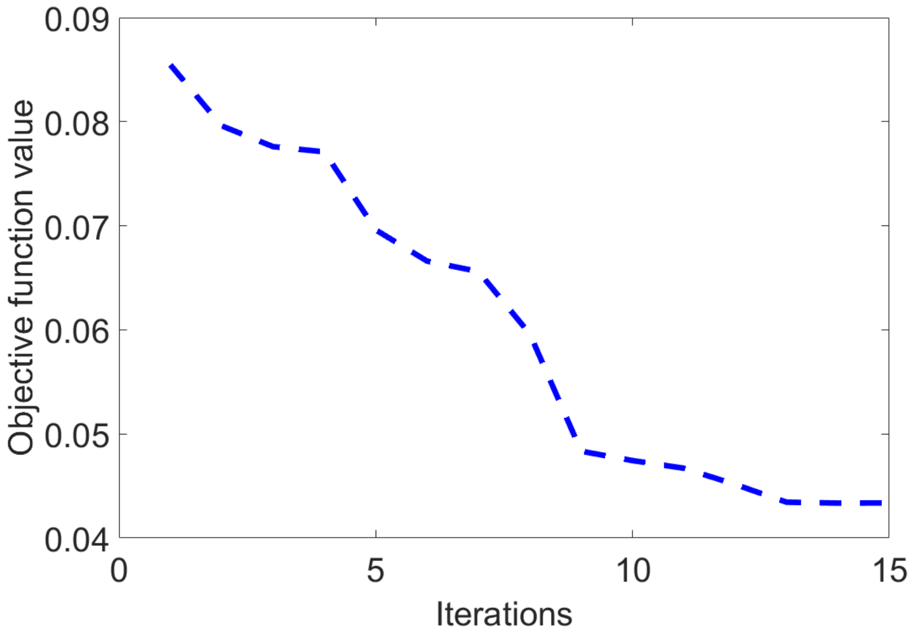

Figure D.3: The *trust-region* algorithm performance to minimize the objective function at the starting point of the parameters $(w_1,\, \alpha_1) = (0.3,\, 80.5°)$ for CSIG surface.

Bibliography

[1] G. Aad and et al. Observation of a New Particle in the Search for the Standard Model Higgs boson with the ATLAS Detector at the LHC. *Physics Letters B*, 716(1):1–29, 2012.

[2] T. Abe and et al. Multipactoring Suppression by Fine Grooving of Conductor Curfaces of Coaxial-Line Input Couplers for High Beam Current Storage Rings. *Phys. Rev. ST Accel. Beams*, 13:102001, Oct 2010. doi: 10.1103/PhysRevSTAB.13.102001.

[3] CST AG. *CST Studio Suite®*. Now part of the SIMULIA brand of Dassault Systèmes, Darmstadt, Germany, 2017. URL `https://www.3ds.com`.

[4] A. Arnold. *Simulation und Messung der Hochfrequenzeigenschaften einer Supraleitenden Photo-Elektronenquelle*. PhD thesis, Universität Rostock, 2012.

[5] A. Arnold and et al. Development of a Superconducting Radio Frequency Photoelectron Injector. *Nuclear Instruments and Methods in Physics Research*, 577:440 – 454, 2007. doi: 10.1016/j.nima.2007.04.171.

[6] A. Arnold and J. Teichert. Overview on Superconducting Photoinjectors. *Phys. Rev. ST Accel. Beams*, 14:024801, Feb 2011. doi: 10.1103/PhysRevSTAB.14.024801.

[7] K. P. Artyomov and et al. PIC Code KARAT Simulation of Different Types of Polarization Radiation Generated by Relativistic Electron Beam. In *In Journal of Physics: Conference Series*, volume 357, page 012022. IOP Publishing, 2012.

[8] V. Baglin and et al. The Secondary Electron Yield of Technical Materials and its Variation with Surface Treatments. Technical report, LHC-Project-Report-433, 2000.

[9] K. Balewski and et al. PETRA III: A Low Emittance Synchrotron Radiation Source. Technical report, DESY, Hamburg, Germany, 2004.

[10] D. P. Barber and et al. Discovery of Three-Jet Events and a Test of Quantum Chromodynamics at PETRA. *Physical Review Letters*, 43(12):830, 1979.

[11] E. M. Baroody. A Theory of Secondary Electron Emission from Metals. *Physical Review*, 78(6):780, 1950.

[12] R. Becker and W. B. Herrmannsfeldt. The Design of Electron and Ion Guns, Beams, and Collectors. *Jornal of Physics: Conference Series.*, 2(1):152, 2004.

[13] P. Berutti, T. Khabiboulline, and G. Romanov. Multipactor Discharge in the PIP-II Superconducting Spoke Resonators. *Fermilab, Technical division, Technical note TD-16-005*, 2016.

[14] G. Bienvenu, P. Fernandes, and R. Parodi. An Investigation on the Field Emitted Electrons in Travelling Wave Accelerating Structures. *Nuclear Instruments and Methods in Physics Research Section A: Accelerators, Spectrometers, Detectors and Associated Equipment*, 320(1-2):1–8, 1992.

[15] D. H. Bilderback, P. Elleaume, and E. Weckert. Review of Third and Next Generation Synchrotron Light Sources. *Journal of Physics B: Atomic, molecular and optical physics*, 38(9):S773, 2005.

[16] C. K. Birdsall. Particle-in-Cell Charged-Particle Simulations, Plus Monte Carlo Collisions with Neutral Atoms, PIC-MCC. *IEEE Transactions on Plasma Science*, 19(2):65–85, 1991.

[17] C. K. Birdsall and A. B. Langdon. *Plasma Physics via Computer Simulation.* Institute of Physics Publ., 1995. ISBN 0-7503-0117-1.

[18] M. Bousonville and S. Choroba. Multipacting in an RF Window: Simulations and Measurements. In *Journal of Physics: Conference Series*, volume 1067, page 082001. IOP Publishing, 2018.

[19] H. Bruining. *Physics and Applications of Secondary Electron Emission.* Pergamon Science Series: Electronics and Waves—a Series of Monographs. McGraw-Hill Book Co., New York, 1954.

[20] A. Burrill and et al. Multipacting Analysis of a Quarter Wave Choke Joint Used for Insertion of a Demountable Cathode into a SRF Photoinjector. In *Particle Accelerator Conference, 2007. PAC. IEEE*, pages 2544–2546. IEEE, 2007.

[21] A. Burrill and et al. First Horizontal Test Results of the HZB SRF Photoinjector for bERLinPro. In *6th International Particle Accelerator Conference*, IPAC2015, Richmond, VA, USA, 2015. JACoW Publishing. ISBN 978-3-95450-168-7. doi: 10.18429/JACoW-IPAC2015-WEPMA011.

[22] G. Burt and A. C. Dexter. Prediction of Multipactor in the Iris Region of RF Deflecting Mode Cavities. *Physical Review Special Topics-Accelerators and Beams*, 14(12):122002, 2011.

[23] G. Burt and et al. Benchmarking Simulations of Multipactor in Rectangular Waveguides using CST-Particle Studio. In *SRF 2009*, volume 9, page 321, 2009.

[24] H. Chaloupka and et al. A Proposed Superconducting Photoemission Source of High Brightness. *Nuclear Instruments and Methods in Physics Research Section A: Accelerators, Spectrometers, Detectors and Associated Equipment*, 285(1-2):327–332, 1989.

[25] C. Chang and et. al. The Effect of Grooved Surface on Dielectric Multipactor. *Journal of Applied Physics*, 105(12):123305, 2009.

[26] C. Chang and et al. Review of Recent Theories and Experiments for Improving High-power Microwave Window Breakdown Thresholds. *Physics of Plasmas*, 18:5, 2011. URL `https://doi.org/10.1063/1.3560599`.

[27] S. Chatrchyan and et al. Observation of a New boson at a Mass of 125 GeV with the CMS Experiment at the LHC. *Physics Letters B*, 716(1):30–61, 2012.

[28] P. G. Ciarlet. *The Finite Element Method for Elliptic Problems*, volume 40. SIAM, 2002.

[29] M. Clemens and T. Weiland. Discrete Electromagnetism with the Finite Integration Technique. *Progress In Electromagnetics Research*, 32:65–87, 2001.

[30] F. T. Cole. Design Report Tevatron 1 Project. Technical Report FERMILAB-DESIGN-1984-01, FERMILAB, 1984. URL `#https://cds.cern.ch/record/1478620#`.

[31] R. E. Collin. *Foundations for Microwave Engineering*. John Wiley & Sons, 2007.

[32] R. Courant. Variational Methods for the Solution of Problems of Equilibrium and Vibrations. *Bulletin of the American Mathematical Society*, 49(1):1–23, 1943.

[33] M. Curtin and et al. First Demonstration of a Free-Electron Laser Driven by Electrons from a Laser-Irradiated Photocathode. *Nuclear Instruments and Methods in Physics Research Section A: Accelerators, Spectrometers, Detectors and Associated Equipment*, 296(1):127 – 133, 1990. ISSN 0168-9002. URL `http://www.sciencedirect.com/science/article/pii/016890029091199L`.

[34] A. di Bona and et al. Auger and X-ray Photoemission Spectroscopy Study on Cs2Te Photocathodes. *Journal of Applied Physics*, 80(5):3024–3030, 1996. doi: 10.1063/1.363161. URL `https://doi.org/10.1063/1.363161`.

[35] D. H. Dowell and et al. First Operation of a Photocathode Radio Frequency Gun Injector at High Duty Factor. *Applied physics letters*, 63(15):2035–2037, 1993.

[36] M. Eldred, C. Webster, and P. Constantine. Evaluation of Non-intrusive Approaches for Wiener-Askey Generalized Polynomial Chaos. In *10th AIAA Non-Deterministic Approaches Conference*, number AIAA-2008-1892, page 1892, 2008.

[37] P. Emma and et al. First Lasing and Operation of an Angstrom-Wavelength Free-Electron Laser. *nature photonics*, 4(9):641, 2010.

[38] P. Farnsworth. Television by Electron Image Scanning. *Journal of the Franklin Institute*, 218(4):411–444, 1934. doi: 10.1016/S0016-0032(34)90415-4.

[39] H. Fehske, R. Schneider, and A. Weiße. *Computational Many-Particle Physics*, volume 739. Springer, 2007.

[40] J. L. A. Fernandez and et al. A Large Hadron Electron Collider at CERN Report on the Physics and Design Concepts for Machine and Detector. *Journal of Physics G: Nuclear and Particle Physics*, 39(7):075001, 2012.

[41] T. Flisgen. *Compact State-Space Models for Complex Superconducting Radio-Frequency Structures based on Model Order Reduction and Concatenation Methods.* PhD thesis, University of Rostock, 2015. URL `http://purl.uni-rostock.de/rosdok/id00001811`.

[42] M. A. Furman and M. T. F. Pivi. Probabilistic Model for the Simulation of Secondary Electron Emission. *Accelerators and Beams*, 5:124404, 2002.

[43] F. Gabriel and et al. The Rossendorf Radiation Source ELBE and its FEL Projects. *Nuclear Instruments and Methods in Physics Research Section B: Beam Interactions with Materials and Atoms*, 161:1143–1147, 2000.

[44] R. L. Geng. Multipacting Simulations for Superconducting Cavities and RF Coupler Waveguides. In *Proceedings of the 2003 Particle Accelerator Conference*, volume 1, pages 264–268. IEEE, 2003.

[45] R. L. Geng and et al. Suppression of Multipacting in Rectangular Coupler Waveguides. *Nuclear Instruments and Methods in Physics Research Section A: Accelerators, Spectrometers, Detectors and Associated Equipment*, 508(3):227–238, 2003.

[46] R. L. Geng and et al. Fabrication and Performance of Superconducting RF Cavities for the Cornell ERL Injector. pages 2340 – 2342, 07 2007. doi: 10.1109/PAC.2007.4441243.

[47] R. Ghanem and P. D. Spanos. *Stochastic Finite Elements: A Spectral Approach*. Courier Corporation, 2003.

[48] E. W. B. Gill and A. von Engel. Starting Potentials of High-frequency Gas Discharges at Low Pressure. In *Proceedings of the Royal Society of London. Series A. Mathematical and Physical Sciences*, volume 192 of *446-463*, 1948. doi: 10.1098/rspa.1948.0018.

[49] D. Gonzalez-Iglesias and et al. Multipactor in a Coaxial Line under the Presence of an Axial DC Magnetic Field. *IEEE Electron Device Letters*, 33 (5):727–729, 2012.

[50] D. Gonzalez-Iglesias and et al. Multipactor Mitigation in Coaxial Lines by means of Permanent Magnets. *IEEE Transactions on Electron Devices*, 61 (12):4224–4231, 2014.

[51] L. Le Gratiet, S. Marelli, and B. Sudret. *Metamodel-Based Sensitivity Analysis: Polynomial Chaos Expansions and Gaussian Processes*, pages 1289–1325. 06 2017. doi: 10.1007/978-3-319-12385-1_38.

[52] S. M. Gruner and et al. Energy Recovery Linacs as Synchrotron Radiation Sources. *Review of Scientific Instruments*, 73(3):1402–1406, 2002.

[53] F. Hamme, U. Becker, and P. Hammes. Simulation of Secondary Electron Emission with CST PARTICLE STUDIO. In *Proc. ICAP*, pages 160–163, 2006.

[54] J. Han and et al. Single-Side Electron Multipacting at the Photocathode in RF Guns. *Physical Review Special Topics-Accelerators and Beams*, 11(1): 013501, 2008.

[55] A. J. Hatch and H. B. Williams. The Secondary Electron Resonance Mechanism of Low-Pressure High-Frequency Gas Breakdown. *Journal of Applied Physics*, 25:417–423, 1954. doi: 10.1063/1.1721656. URL `https://doi.org/10.1063/1.1721656`.

[56] A. J. Hatch and H. B. Williams. Multipacting Modes of High-Frequency Gaseous Breakdown. *Physical Review*, 112:681–685, Nov 1958. doi: 10.1103/PhysRev.112.681. URL `https://link.aps.org/doi/10.1103/PhysRev.112.681`.

[57] J. Heller, C. Schmidt, U. van Rienen, and T. Flisgen. Quantification of Geometric Uncertainties in Single Cell Cavities for BESSY VSR using Polynomial Chaos. In *5th International Particle Accelerator Conference (IPAC2014)*, Dresden, Germany, 2014.

[58] J. Heller, U. Van Rienen, T. Flisgen, and C. Schmidt. Uncertainty Quantification for Complex RF-structures Using the State-space Concatenation Approach. In *PIERS Proceedings*, Prague, Czech Republic, 2015.

[59] W. B. Herrmannsfeldt. EGUN: An Electron Optics and gun Design Program. Technical report, Stanford Linear Accelerator Center, 1988.

[60] E. Hoyt and et al. Processing of OFE Copper Beam Chambers for PEP-II High Energy Ring. In *Proceedings Particle Accelerator Conference*, volume 3, pages 2054–2056. IEEE, 1995.

[61] D. Janssen and et al. First Operation of a Superconducting RF-Gun. *NIM*, (A507(2003)314):314–317, 2003.

[62] R. Kishek and et al. Interaction of Multipactor Discharge and RF Circuit. In *Proc. SPIE 2843, Intense Microwave Pulses IV*, volume 2843, 1996. doi: 10.1117/12.255408. URL `https://doi.org/10.1117/12.255408`.

[63] R. A. Kishek and et al. Multipactor Discharge on Metals and Dielectrics: Historical Review and Recent Theories. *Physics of Plasmas*, 5(5):2120–2126, 1998. doi: 10.1063/1.872883. URL `https://doi.org/10.1063/1.872883`.

[64] R. A. Kishek and Y. Y. Lau. Multipactor Discharge on a Dielectric. *Physical review letters*, 80(1):193, 1998.

[65] U. Klein and D. Proch. Multipactoring in Superconducting RF Structures. *proceedings of the Conference on Future Possibilities for Electron Accelerators, Charlottesville*, volume N1–17, 1979.

[66] P. Kneisel, R. Vincon, and J. Halbritter. First Results on Elliptically Shaped Cavities. *Nuclear Instruments and Methods in Physics Research*, 188(3):669–670, 1981.

[67] J. Knobloch, W. Hartung, and H. Padamsee. Multipacting in 1.5-GHz Superconducting Niobium Cavities of the CEBAF Shape. In *Proceedings of the 8th Workshop on RF Superconductivity, Padua, Italy*, 1997. URL `http://www.lns.cornell.edu/public/SRF/1998/SRF981012-09`.

[68] K. Ko and et al. Advances in Parallel Electromagnetic Codes for Accelerator Science and Development. Technical report, SLAC National Accelerator Lab., Menlo Park, CA (United States), 2011.

[69] D. Kostin and et al. Multipacting in HOM Couplers at the 1.3 GHz 9-Cell TESLA Type SRF Cavity. In *inProceedings of SRF2011*, 2011.

[70] A. A. Krasnov. Molecular Pumping Properties of the LHC Arc Beam Pipe and Effective Secondary Electron Emission from Cu Surface with Artificial Roughness. *Vacuum*, 73(2):195 – 199, 2004. ISSN 0042-207X. doi: https://doi.org/10.1016/j.vacuum.2003.12.051. URL `http://www.sciencedirect.com/science/article/pii/S0042207X03002380`.

[71] B. Krietenstein, R. Schuhmann, P. Thoma, and T. Weiland. The Perfect Boundary Approximation Technique Facing the Big Challenge of High Precision Field Computation. In *Proceedings of the XIX International Linear Accelerator Conference (LINAC 98), Chicago, USA*, pages 860–862, 1998.

[72] J. Leach. *AutoCAD 2016 Instructor*. Sdc Publications, 2015.

[73] P. Lenard. *Quantitatives über Kathodenstrahlen aller Geschwindigkeiten*, volume 5. C. Winter's Universitatsbuchhandlung, Heidelberg, 1918.

[74] K. Levenberg. A Method for the Solution of Certain Non-Linear Problems in Least Squares. *Quarterly of applied mathematics*, 2(2):164–168, 1944.

[75] Z. K. Liu and et al. Multipacting in a Coaxial Coupler with Bias Voltage for SRF Operation with a Large Beam Current. *Journal of Instrumentation*, 11 (09):P09015–P09015, sep 2016. doi: 10.1088/1748-0221/11/09/p09015. URL `https://doi.org/10.1088%2F1748-0221%2F11%2F09%2Fp09015`.

[76] L. Lorenz. Ueber die Identität der Schwingungen des Lichts mit den Elektrischen Strömen. *Annalen der Physik*, 207(6):243–263, 1867.

[77] L. D. Ludeking, A. J. Woods, and P. Stoltz. Well Matched Electromagnetic Boundary in FDTD-PIC for Charged Particle Penetration. *Open Plasma Physics Journal*, 3:53–59, 2010.

[78] A. Markovik. *Simulation of the Interaction of Positively Charged Beams and Electron Clouds*. PhD thesis, Universität Rostock, Fakultät für Informatik und Elektrotechnik,, 2013. URL `http://rosdok.uni-rostock.de/resolve?urn=urn:nbn:de:gbv:28-diss2014-0031-8&pdf`.

[79] A. Markovik, G. Pöplau, U. van Rienen, and R. Wanzenberg. Tracking Code with 3D Space Charge Calculations Taking into Account the Elliptical Shape of the Beam Pipe. In *Proceedings of ICAP 2006 (Proceedings of the 7th International Computational Accelerator Physics Conference), Chamonix Mont-Blanc, France*, pages 218–221, 2006.

[80] J. C. Maxwell. II. A Dynamical Theory of the Electromagnetic Field. *Proceedings of the Royal Society of London*, (13):531–536, 1864.

[81] K. T. McDonald. Analysis of TEM Waves in a Coaxial Cable via the Scalar Potential. 2017.

[82] B. W. J. McNeil and N. R. Thompson. X-ray Free-Electron Lasers. *Nature photonics*, 4(12):814, 2010.

[83] P. Michel. The Radiation Source ELBE at the Forschungszentrum Dresden-Rossendorf. In *2008 IEEE Nuclear Science Symposium Conference Record*, pages 3078–3080. IEEE, 2008.

[84] P. Michelato. Photocathodes for RF Photoinjectors. *Nuclear Instruments and Methods in Physics Research Section A: Accelerators, Spectrometers, Detectors and Associated Equipment"*, 393(1):455 – 459, 1997. ISSN 0168-9002. doi: https://doi.org/10.1016/S0168-9002(97)00545-7. URL `http://www.sciencedirect.com/science/article/pii/S0168900297005457`.

[85] O. Moreau and et al. Stochastic Nondestructive Testing Simulation: Sensitivity Analysis Applied to Material Properties in Clogging of Nuclear Powerplant Steam Generators. *IEEE Transactions on Magnetics*, 49(5):1873–1876, 2013.

[86] Y. Morozumi. RF Structure Design and Analysis XXXIII. 2007.

[87] I. Munteanu and F. Hirtenfelder. Convergence of the Finite Integration Technique on Various Mesh Types. volume 5, page 4, 2005.

[88] S. Myers and E. Picasso. The Design, Construction and Commissioning of the CERN Large Electron-Positron Collider. *Contemporary Physics*, 31(6): 387–403, 1990.

[89] J. Nédélec. Mixed Finite Elements in $\mathbb{R}^3$. *Numer. Math.*, 35(1):315–341, 1980.

[90] J. Nédélec. A New Family of Mixed Finite Elements in $\mathbb{R}^3$. *Numerische Mathematik*, 50(1):57–81, 1986.

[91] A. Neumann and et al. The bERLinPro SRF Photoinjector System from First RF Commissioning to First Beam. In *9th Int. Particle Accelerator Conf.(IPAC'18), Vancouver, BC, Canada, April 29-May 4, 2018*, pages 1660–1663. JACOW Publishing, Geneva, Switzerland, 2018.

[92] C. K. Ng and et al. Multipacting Simulation of Accelerator Cavities using ACE3P. In *Proceedings of the 25th Particle Accelerator Conference, PAC-2013, Pasadena, CA*, page 216, 2013.

[93] H. K. A. Nguyen and et al. Calculations of Multipactor Growth in Rectangular Waveguides. *IEEE Transactions on Plasma Science*, 47(2):1364–1371, 2019.

[94] A. R. Nyaiesh and et al. *Properties of thin antimultipactor coatings for klystron windows.* PhD thesis, AVS, 1986.

[95] H. Padamsee. Design Topics for Superconducting RF Cavities and Ancillaries. *arXiv preprint arXiv:1501.07129*, 2015.

[96] H. Padamsee, J. Knobloch, and T. Hays. *RF Superconductivity for Accelerators.* John Wiley and Sons, second edition, 2011.

[97] E. Panofski. *Beam Dynamics and Limits for High Brightness, High Average Current Superconducting Radiofrequency (SRF) Photoinjectors.* PhD thesis, 2019.

[98] I. Petrushina and et al. Mitigation of Multipacting in 113 MHz Superconducting RF Photoinjector. *Physical Review Accelerators and Beams*, 21(8):082001, 2018.

[99] T. S. Pettersson and P. Lefevre. The Large Hadron Collider: Conceptual Design. Technical report, CERN-AC-95-05 LHC, CERN, Geneva, October 1995.

[100] J. Pierron and et al. Effect of Rectangular Grooves and Checkerboard Patterns on the Electron Emission Yield. *Journal of Applied Physics*, 124(9):095101, 2018.

[101] P. C. Pinto and et al. Carbon Coatings with Low Secondary Electron Yield. *Vacuum*, 98:29–36, 2013.

[102] M. Pivi and et al. Sharp Reduction of the Secondary Electron Emission Yield from Grooved Surfaces. *Journal of Applied Physics*, 104(10):104904, 2008. doi: 10.1063/1.3021149. URL `https://doi.org/10.1063/1.3021149`.

[103] H. Qian, M. Krasilnikov, and F. Stephan. A Cryocooled Normal-Conducting and Superconducting Hybrid CW Photoinjector. In *38th International Free Electron Laser Conference*, Santa Fe, NM, USA, 2018. JACoW Publishing. doi: 10.18429/JACoW-FEL2017-WEP009.

[104] R. R. Xiang and et al. Cs2Te Normal Conducting Photocathodes in the Superconducting RF Gun. *Physical Review Special Topics-Accelerators and Beams*, 13(4):043501, 2010.

[105] T. Rao and D. H. Dowell. *An Engineering Guide to Photoinjectors.* 2014.

[106] S. A. Rice and J. P. Verboncoeur. A Comparison of Multipactor Predictions using two Popular Secondary Electron Models. *IEEE Transactions on Plasma Science*, 42(6):1484–1487, 2014.

[107] G. Romanov. Update on Miltipactor in Coaxial Waveguides Using CST Particle Studio. *PAC2011, New York, NY, USA, TUP008*, 2011.

[108] G. Romanov. Simulation of Multipacting with Space Charge Effect. *American Journal of Physics and Applications*, 5(FERMILAB-PUB-17-399-TD), 2017.

[109] G. Romanov, P. Berrutti, and T. N. Khabiboulline. Simulation of Multipacting in SC Low Beta Cavities at FNAL. *Proc. IPAC2015 (Richmond, VA, USA,)*, 2015.

[110] A. Saltelli and et. al. *Global Sensitivity Analysis. The Primer.* John Wiley & Sons, 2008.

[111] S. V. Samsonov and et al. Generation and Compression of Frequency Modulated Pulses from a Relativistic BWO. In *2004 International Conference on High-Power Particle Beams (BEAMS 2004)*, pages 430–433. IEEE, 2004.

[112] J. M. Sattler and et. al. Modeling Micro-porous Surfaces for Secondary Electron Emission Control to Suppress Multipactor. *Journal of Applied Physics*, 122(5), 2017.

[113] C. Schlemper, X. Jiang, and M. Vogel. Next Generation of SRF-guns: Low Secondary Electron Yield Based on a Thin Film Approach. In *Proceedings of SRF*, number TUPB047, Whistler, BC, Canada, 2015.

[114] C. Schmidt. *Uncertainty Quantification in a Computationally Optimised Volume Conductor Model for Deep Brain Stimulation.* PhD thesis, 2013.

[115] C. Schmidt, P. Grant, M. Lowery, and U. van Rienen. Influence of Uncertainties in the Material Properties of Brain Tissue on the Probabilistic Volume of Tissue Activated. *IEEE Transactions on Biomedical Engineering*, 60(5):1378–1387, 2012.

[116] C. Schmidt, T. Flisgen, J. Heller, and U. van Rienen. Comparison of Techniques for Uncertainty Quantification of Superconducting Radio Frequency Cavities. In *2014 International Conference on Electromagnetics in Advanced Applications (ICEAA)*, pages 117–120. IEEE, 2014.

[117] P. Schmüser and et al. *Free-Electron Lasers in the Ultraviolet and X-ray Regime*, volume 258. Springer, 2014.

[118] V. E. Semenov and et al. Multipactor in Rectangular Waveguides. *Physics of Plasmas*, 14(3):033501, 2007.

[119] V. E. Semenov and et al. Simulations of Multipactor in Circular Waveguides. *Physics of Plasmas*, 17(12):123503, 2010.

[120] V. Shemelin. Generalized Phase Stability in Multipacting. *Physical Review Special Topics-Accelerators and Beams*, 14(9):092002, 2011.

[121] V. Shemelin. Multipactor in Crossed RF Fields on the Cavity Equator. *Phys. Rev. ST Accel. Beams*, 16:012002, Jan 2013. doi: 10.1103/PhysRevSTAB.16.012002. URL `https://link.aps.org/doi/10.1103/PhysRevSTAB.16.012002`.

[122] V. Shemelin, H. Padamsee, and R. L. Geng. Optimal Cells for TESLA Accelerating Structure. *Nuclear Instruments and Methods in Physics Research Section A: Accelerators, Spectrometers, Detectors and Associated Equipment*, 496(1):1–7, 2003.

[123] V. D. Shemelin. Existence Zones for Multipactor Discharges. *Sov. Phys. Tech. Phy*, 31(5), 1986.

[124] I. M. Sobol. Sensitivity Estimates for Nonlinear Mathematical Models. *Mathematical modelling and computational experiments*, 1(4):407–414, 1993.

[125] I. M. Sobol. Global Sensitivity Indices for Nonlinear Mathematical Models and their Monte Carlo Estimates. *Mathematics and computers in simulation*, 55(1-3):271–280, 2001.

[126] E. Somersalo and et al. Computational Methods for Analyzing Electron Multipacting in RF Structures. *Particle Accelerators*, 59:107 – 141, 1998.

[127] E. Somersalo, P. Ylä-Oijala, and D. Proch. Analysis of Multipacting in Coaxial Lines. In *Proceedings Particle Accelerator Conference*, volume 3, pages 1500–1502. IEEE, 1995.

[128] H. Spachmann and U. Becker. Electron Gun Simulation with CST PARTICLE STUDIO. *Nuclear Instruments and Methods in Physics Research Section A: Accelerators, Spectrometers, Detectors and Associated Equipment*, 558(1):50–53, 2006.

[129] G. Stupakov and M. Pivi. Supperssion of the Effective Secondary Emission Yield for a Grooved Metal Surface. In *CERN Reports No.LCC-0145, No. SLAC-TN-04-045*, Stanford Linear Accelerator Center Stanford University 2575 Sand Hill Road Menlo Park, CA, 2004. LCC-0145 SLAC-TN-04-045.

[130] B. Sudret. Global Sensitivity Analysis using Polynomial Chaos Expansions. *Reliability Engineering & System Safety*, 93(7):964–979, 2008.

[131] B. Sudret, M. Berveiller, and M. Lemaire. A Stochastic Finite Element Procedure for Moment and Reliability Analysis. *European Journal of Computational Mechanics/Revue Européenne de Mécanique Numérique*, 15(7-8):825–866, 2006.

[132] T. J. Sullivan. *Introduction to Uncertainty Quantification*, volume 63. Springer, 2015.

[133] J. Teichert and et al. A Superconducting Photo-Injector with 3+ 1/2-Cell Cavity for the ELBE Linac. In *Proceedings of EPAC 2004*, number No. CARE-Conf-04-031-PHIN, Lucerne, Switzerland, 2004. Proceedings of EPAC 2004.

[134] J. Teichert and et al. Operation of the Superconducting RF Photo Gun at ELBE. *Journal of Physics: Conference Series*, 298:012008, 2011.

[135] J. Teichert and et al. Free-Electron Laser Operation with a Superconducting Radio-Frequency Photoinjector at ELBE. *Nuclear Instruments and Methods in Physics Research Section A: Accelerators, Spectrometers, Detectors and Associated Equipment*, 743:114–120, 2014.

[136] J. Teichert and et al. First Beam Characterization of SRF Gun II with a Copper Photocathode. In *Proceedings of ERL2015, Stony Brook, NY, USA*, 2015.

[137] M. Tigner. A Possible Apparatus for Electron Clashing Beam Experiments. *Il Nuovo Cimento (1955-1965)*, 37(3):1228–1231, 1965.

[138] G. Torregrosa and et al. Time Evolution of an Electron Discharge in a Parallel-Plate Dielectric-Loaded Waveguide. *IEEE Electron Device Letters*, 27, 2006. doi: 10.1109/LED.2006.877284.

[139] E. T. Tulu, A. Arnold, and U. van Rienen. 3D Multipacting Study for the Rossendorf SRF Gun. In *proceedings of SRF2013*, number THP040, Paris, France, 2013.

[140] E. T. Tulu, A. Arnold, and U. van Rienen. Different Countermeasures of Electron Amplification in the Photocathode Unit. In *Proceedings, 5th International Particle Accelerator Conference (IPAC 2014)*, number MOPRI028, Dresden, Germany, 2014. URL `http://jacow.org/IPAC2014/papers/mopri028.pdf`.

[141] E. T. Tulu, A. Arnold, and U. van Rienen. Numerical Studies on a Modified Cathode Tip for the ELBE Superconducting RF Gun. In *Proc. of International Particle Accelerator Conference (IPAC2017), Copenhagen, Denmark, 19 May, 2017*, number 8, pages 515–517, Copenhagen, Denmark, May 2017. JACoW. ISBN 978-3-95450-182-3. doi: https://doi.org/10.18429/JACoW-IPAC2017-MOPIK008. URL `http://jacow.org/ipac2017/papers/mopik008.pdf`.

[142] E. T. Tulu, U. van Rienen, and A. Arnold. Systematic Study of Multipactor Suppression Techniques for a Superconducting RF Gun. *Physical Review*

Accelerators and Beams, 21, 11 2018. doi: 10.1103/PhysRevAccelBeams.21.113402.

[143] R. Udiljak and et al. Improved Model for Multipactor in Low Pressure Gas. *Physics of Plasmas*, 11(11):5022–5031, 2004. doi: 10.1063/1.1797691. URL `https://doi.org/10.1063/1.1797691`.

[144] R. Udiljak and et al. Multipactor in a Coaxial Transmission Line. I. Analytical Study. *Physics of plasmas*, 14(3):033508, 2007.

[145] R. Valizadeh and et al. Low Secondary Electron Yield Engineered Surface for Electron Cloud Mitigation. *Applied Physics Letters*, 105(23):231605, 2014.

[146] C. Yin Vallgren. *Low Secondary Electron Yield Carbon Coatings for Electron Cloud Mitigation in Modern Particle Accelerators.* Number CERN-THESIS-2011-063. CERN, 2011.

[147] U. van Rienen. *Numerical Methods in Computational Electrodynamics: Linear Systems in Practical Applications*, volume 12. Springer Science & Business Media, 2012.

[148] J. R. M. Vaughan. Multipactor. *IEEE Transactions on Electron Devices*, 35 (7):1172, 1988.

[149] R. Vaughan. Secondary Emission Formulas. *IEEE Transactions on Electron Devices*, 40(4):830, 1993.

[150] M. Vogel, X. Jiang, and C. Schlemper. Carbon-based Coatings for Electron Cloud Mitigation in SRF Photocathodes. In *18th International Conference on RF Superconductivity (SRF2017)*, Lanzhou, China, 2018. doi: 10.18429/JACoW-SRF2017-THPB076.

[151] D. Wang and et al. Secondary Electron Emission Characteristics of Nanostructured Silver Surfaces. *Journal of Applied Physics*, 122(15):153302, 2017.

[152] L. Wang, T. O. Raubenheimer, and G. Stupakov. Suppression of Secondary Emission in a Magnetic Field using Triangular and Rectangular Surfaces.

[153] S. Wang. *Secondary Electron Yield Measurements of Anti-multipacting Surfaces for Accelerators.* PhD thesis, Loughborough University, 2016.

[154] T. P. Wangler. *RF Linear Accelerators.* John Wiley & Sons, 2008.

[155] T. Weiland. A Discretization Method for the Solution of Maxwell's Equations for Six-Component Fields. *Electronics and Communication,(AEÜ),*, 1977.

[156] T. Weiland. On the Unique Numerical Solution of Maxwellian Eigenvalue Problems in Three Dimensions. *Part. Accel.*, 17(DESY-84-111):227–242, 1984.

[157] G. A. Westenskow and J. M. J. Madey. Microwave Electron Gun. *Laser and Particle Beams*, 2(2):223–225, 1984.

[158] N. Wiener. The Homogeneous Chaos. *American Journal of Mathematics*, 60 (4):897–936, 1938.

[159] K. Wille. The Physics of Particle Accelerators: an Introduction. 2000.

[160] H. Winick. Fourth Generation Light Sources. In *Proceedings of the 1997 Particle Accelerator Conference (Cat. No. 97CH36167)*, volume 1, pages 37–41. IEEE, 1997.

[161] A. J. Woods and L. D.Ludeking. MAGIC Electromagnetic FDTD-PIC Code Dense Plasma Model Comparison with LSP. *Open Plasma Physics Journal*, 3:73–77, 2010.

[162] R. Xiang and et al. A Step Closer to the CW High Brilliant Beam with the ELBE SRF-Gun-II. In *6th International Particle Accelerator Conferenc, IPAC2015*, Richmond, VA, USA, 2015. 6th International Particle Accelerator Conferenc, IPAC2015. ISBN 978-3-95450-168-7.

[163] R. Xiang and et al. Running Status of SRF GUN-II at ELBE Center. In *29th Linear Accelerator Conf.*, LINAC2018, Beijing, China, 2018. JACoW Publishing. doi: 10.18429/JACoW-LINAC2018-THPO125.

[164] D. Xiu. *Numerical Methods for Stochastic Computations: a Spectral Method Approach.* Princeton university press, 2010.

[165] W. Xu and et al. Design, Simulations, and Conditioning of 500 kw Fundamental Power Couplers for a Superconducting RF Gun. *Physical Review Special Topics-Accelerators and Beams*, 15(7):072001, 2012.

[166] W. Xu and et al. BNL SRF Gun Commissioning. pages 155–158, 2013.

[167] W. Xu and et al. First Beam Commissioning at BNL ERL SRF Gun. In *Proceedings of SRF2015,*, Whistler, BC, Canada, 2015. Proceedings of SRF2015,.

[168] W. Xu and et al. Multipacting-free Quarter-wavelength Choke Joint Design for BNL SRF. In *Proceedings, 6th International Particle Accelerator Conference (IPAC 2015): Richmond, Virginia, USA, May 3-8, 2015*, page TUPMA047, 2015. URL `http://accelconf.web.cern.ch/AccelConf/IPAC2015/papers/tupma047.pdf`.

[169] M. Ye, D. Wang, and Y. He. Mechanism of Total Electron Emission Yield Reduction using a Micro-porous Surface. *Journal of Applied Physics*, 121(12): 124901, 2017.

[170] K. Yee. Numerical Solution of Initial Boundary Value Problems Involving Maxwell's Equations in Isotropic Media. *IEEE Transactions on antennas and propagation*, 14(3):302–307, 1966.

[171] P. Ylä-Oijala. Suppressing Electron Multipacting in Coaxial Lines by DC Voltage. Technical report, SCAN-9802124, 1997.

[172] P. Ylä-Oijala and S. Ärvenpää. Finite Element Method for the Electromagnetic Field Computation in Cylindrically Symmetric RF Structures. *Electromagnetics*, 22(3):261–273, 2002. doi: 10.1080/02726340252886492. URL `https://doi.org/10.1080/02726340252886492`.

[173] P. Ylä-Oijala and et al. Multipacting Analysis and Electromagnetic Field Computation by the Boundary Integral Equation Method in RF Cavities and Waveguides. 1999.

[174] P. Ylä-Oijala and et al. MultiPac 2.1—Multipacting Simulation Toolbox with 2D FEM Field Solver and MATLAB Graphical User Interface. *User's manual (Rolf Nevanlinna Institute, Helsinki, 2001)*, 2001.

[175] P. Ylä-Oijala and D. Proch. MultiPac–Multipacting Simulation Package with 2D FEM Field Solver. In *Proc. of the 10th Workshop on RF Superconductivity, Tsukuba, Japan*, 2001.

[176] P. Ylä-Oijala and M. Ukkola. Suppressing Electron Multipacting in Ceramic Windows by DC Bias. *Nuclear Instruments and Methods in Physics Research Section A: Accelerators, Spectrometers, Detectors and Associated Equipment*, 474(3):197 – 208, 2001. ISSN 0168-9002. doi: https://doi.org/10.1016/S0168-9002(01)00882-8. URL `http://www.sciencedirect.com/science/article/pii/S0168900201008828`.

[177] Y. Yuan. A Review of Trust Region Algorithms for Optimization. 99(1): 271–282, 2000.

[178] Y. Yuan. Recent Advances in Trust Region Algorithms. *Mathematical Programming*, 151(1):249–281, 2015.